THE UNIVERSITY OF CHICAGO

NEXT-GENERATION IMAGES OF GALAXY CLUSTERS AT MILLIMETER WAVELENGTHS

A DISSERTATION SUBMITTED TO
THE FACULTY OF THE DIVISION OF THE PHYSICAL SCIENCES
IN CANDIDACY FOR THE DEGREE OF
DOCTOR OF PHILOSOPHY

DEPARTMENT OF PHYSICS

BY
JOSEPH ERNEST GOLEC

CHICAGO, ILLINOIS
AUGUST 2024

For my grandfathers, Joe Golec and Ernest Wisbiski.

The man who does not understand the nature of the universe cannot know his place in it.

- Marcus Aurelius

TABLE OF CONTENTS

LIST OF FIGURES

LIST OF TABLES

ACKNOWLEDGMENTS

What a long strange trip these last seven years have been and I have many people to thank for guidance, mentorship, friendship, and general support.

First I'd like to thank my advisor, Jeff, for honing me into the physicist and researcher I am today. I met Jeff over 10 years ago. It was my freshman year at Michigan and I wasn't really sure what direction I wanted to take my physics studies. All I knew is that I needed to get involved in research, I was broadly interested in cosmology, and Jeff was hiring undergrads. He rattled off several project ideas to myself and three other undergrads that he had a group interview with (if there's one thing I've learned about Jeff, it's he's efficient with his time when he needs to be) and I was hooked to the enthusiastic hands-on "design-it, build-it, test-it" attitude that he had (and still has). At the end of the interview he smiled and said to the four of us something along the lines of "it would be a pleasure to work with one or any of you, I'm excited." Ten years later, all I can say is the pleasure has been all mine.

Jeff has given me projects that have opened up countless opportunities for me and has given me so much advice for how to be a physicist and a researcher that I'm still trying to absorb to this day. His energetic enthusiasm for science has served me as an incredible motivator and has magnetically attracted me to continue working with him for as long as I have. When I told him I was considering staying at Michigan for graduate school so I could continue working with him he said, and I remember clearly, "I'm salivating at that idea." Such is the vocal support that has always made me feel appreciated and I cannot express my gratitude enough that he has allowed me to be apart of the amazing things he continues to build. Thanks Jeff!

I owe many thanks to my fellow colleagues in the McMahon lab. To the graduate students that were there to aid me in my fledgling years, Charles, Kevin, and Rahul, I owe my basic lab skills. They taught me the quintessential arts of soldering, fastener choice, and which

whiskey belongs in the lab liquor cabinet and which type stays at home. Those skills have only become more valuable since I've been in grad school.

To the post docs who I've had the please working with, Sara and Katie, I thank for the mentorship they provided when Jeff wasn't available. Sara in particular included me on a feedhorn conference proceedings that became the first publication I contributed to and was a co-author on, and for that I am grateful.

My contemporary grad students in the lab, Maya, Shreya, Tommy, Claire, and Carlos have been incredible to work with. I'm continually in awe of the projects everyone is working on and being surrounded by such amazing scientists has only made me work harder. I've always appreciated the conversations with you all and am thankful you have put up with me over the years.

One of those co-workers in particular has become the best friend I could've ever asked for. Carlos has been there for me through it all, thick and thin, and that has made all the difference. The stars aligned when I got to start grad school and work in a lab with someone else who loves beer, baseball, and music as much as myself. We've been co-workers, housemates, drinking buddies, music festival goers, and jazz-fiends to name a few. Carlos has served me as therapist, travel guru, and music-recommender, but I think the most important title I could give him is friend. Thanks for always being there Carlos!

There are so many more players in the show that I need to thank. My housemates from the Miller Street house in Ann Arbor, Rahim, Ryan, and Michael have been apart of so many memories, too many to recount, but I would be remiss if I didn't mention the trivia nights at Bløm. I never really realized how much I missed mead and trivia until I moved to Chicago. I'm grateful for those times we shared and for the credibility you all gave me with the applied physics department.

The physics and astronomy community at UChicago was extremely welcoming after I moved here and I am thankful for that. There are so many people doing such great research

here that it has been inspiring and refreshing to work in an environment where everyone is interested and invested in everyone else's work. I'll call out Emily who has been a great friend and football watching companion, even if she is a Bears fan.

In a more social than academic sense, those communities have also been important for me during grad school. I'd like to call out the undisputed 2023 PSD Beer League Softball Champions, Little Bingo, for providing me with an outlet for my extremely limited athletic ability. Lauren, Kevin, Duncan, Arjun, Rhys, Alex, Cesar, Desi, Sergi, Shu, Sarah M., Sarah C., Lisa, and the geezers Ned, Moses, Rich, and Ed, it has been a privilege playing with you. Alec and Julian haven't just been good teammates, they've been good officemates, and along with Sravan, have allowed me to distract them in the name procrastination countless times. I'm glad to have been able to contribute to countless debates of "how salty is salt?" and "is Julian a Marvel superfan?" (The answers are "pretty salty but there are saltier things" and "yes" respectively).

I'm sure I'm missing individuals who deserve to be mentioned by name here, but I'm extremely forgetful. Please accept my apology and know that I really am appreciative of everyone I've had the pleasure of interacting with throughout grad school.

Penultimately, I'd like to thank my family. My parents have been my biggest supporters all through my life and have encouraged me to be the best I can be. Mom never let me off the hook if she could tell I was slacking. Dad always gave me advice to "learn as much as you can while you can because some day you won't be able to learn anymore," so I took that to heart and spent 25 years in school. I am who I am because of how I was raised by them and I can't thanks them enough. My brother Jason has always been there for me. Roommate, confidante, bookie, and friend I couldn't ask for a better sibling. I bear a constant reminder of my Grandfathers, Joe Golec and Ernest Wisbiski, in my name and can only hope that I live up the tradition of hard working, yet humorous, person of Polish descent that they past down to my parents and unto me.

Finally, I'd like to thank my cat, Chucky. He's only been in my life for a little more than a year now but he's made quite an impact. Chucky greeting me at the door when I get home, even if that's because he knows that means he's getting fed, has never failed to make me feel appreciated. His affection keeps me going and I'm happy he's with me. Although, any typos in this manuscript are entire due to him walking across my keyboard while I've been eating at my computer.

ABSTRACT

Galaxy clusters are the largest and most massive objects in the universe. Observing and studying them unlocks answers to broad cosmological questions, such as the matter content and its distribution in the universe, as well as more specific astrophysical topics regarding the nature of physics within the intracluster medium (ICM). One method to probe clusters is by observing them at millimeter wavelengths via the Sunyaev-Zeldovich (SZ) effect, which results from the interaction of hot electrons in the ICM with Cosmic Microwave Background (CMB) photons. To address expansive questions ranging from cosmological to astrophysical, clusters must be observed at angular scales from arcminutes down to arcseconds. This necessitates multiple instruments: a sensitive arcminute-resolution wide-field survey to discover clusters and provide high fidelity on arcminute scales; and an arcsecond-resolution instrument for efficient high-resolution follow-up. This combination can build statistics and extract as much information as possible from each cluster.

To that end, I present two complementary instruments, the Simons Observatory (SO) Large Aperture Telescope (LAT) and the TolTEC camera on the Large Millimeter Telescope (LMT). Together, these instruments will probe clusters from arcminute to arcsecond scales, unlocking cosmological information about dark matter and dark energy, as well as illuminating astrophysical processes within clusters such as shocks from mergers and feedback mechanisms in the ICM. I present an overview of these instruments and then focus on my contributions. These include metamaterial anti-reflection (AR) coatings fabricated for the refracting optics of the SO LAT and TolTEC, maximum likelihood mapmaking techniques that have been implemented in the TolTEC data reduction pipeline, early images from the TolTEC camera's 2022 commissioning observations, and conclude with forecasts for upcoming cluster observations with the SO LAT and the TolTEC camera.

CHAPTER 1

INTRODUCTION

The largest virialized, or gravitationally bound, objects in the universe are galaxy clusters. These objects consist of many individual galaxies, typically between 50 and 1000, whose dark matter halos have merged and pushed the gravitational potential energy of those halos to be roughly equal to the kinetic energy of the galaxies inside those halos. This creates a massive system that continues to grow over time through the accretion of matter from its surroundings.

Clusters exist in a unique space in the study of cosmological structure formation. They result from linear growth, but gravitational collapse causes them to become extremely non-linear. The conditions that allow for that gravitational collapse are sensitive to the total matter density in the universe and the distribution of that matter. Clusters are relatively young in the cosmological sense and began forming as the universe was becoming dark energy dominated. This makes clusters sensitive to both the matter distribution and the acceleration of the universe, making them rich laboratories for studying cosmological physics encompassing dark matter, dark energy, and even traditional particle physics topics such as constraining the sum of the neutrino masses.

Clusters are also interesting astrophysical objects in their own right. They host some of the most massive galaxies in the universe, and those active galactic nuclei (AGN) inject energy into the intracluster medium (ICM) through powerful jets fueled by the accretion onto the galaxies' supermassive black holes. Along with this AGN feedback into the ICM, the merging of galaxies within clusters sloshes the hot gas in the ICM around and injects energy in the form of shocks. These high-energy astrophysical processes that occur within clusters, combined with many more interesting astrophysical phenomena, make studying the interior of clusters compelling.

The work presented in this thesis is the culmination of efforts to create next-generation

images of galaxy clusters at millimeter wavelengths. These efforts encompass technological advancements, simulations, and analysis methods. In the following chapters, I will detail the work carried out to advance millimeter-wave observations of galaxy clusters. In Chapter 2, I discuss the cosmological and astronomical value in observing clusters, and the mechanism to observe clusters at millimeter wavelengths. Chapter 3 introduces two instruments, the TolTEC camera and the Simons Observatory Large Aperture Telescope (SO LAT), and describe their features that enable them to advance cluster cosmology. I describe the design, fabrication, and performance state-of-the-art metamaterial anti-reflection coatings on the silicon and alumina optics that enable instruments in Chapter 4. I describe maximum-likelihood mapmaking and its advantages in making unbiased images in Chapter 5. In Chapter 6 I present three-color polarization sensitive images of the Crab Nebula from TolTEC's 2022 commissioning campaign. In Chapter 7, I conclude with forecasts of the cluster science the SO LAT will achieve, simulated observations of clusters with TolTEC, and the expected recovery of critical cluster observables from those images.

CHAPTER 2

SCIENCE BACKGROUND

Observations of galaxy clusters probe the distribution of baryons and dark matter, and the impact of dark energy. They also enable the investigation of how energy is injected into the ICM via AGN feedback and the physics of cluster mergers. The goal of this chapter is to explain some fundamental concepts and to firmly motivate millimeter-wave cluster observations.

We will start from the basics of how initial density perturbations in the matter field in the early universe grow and become galaxy clusters. This generates a redshift dependant prediction for the number of clusters in a given mass range called the cluster mass function. We discuss analytical treatments of the cluster mass function and more sophisticated numerical simulation efforts to understand the formation of clusters. We will conclude our discussion of cluster formation with the astrophysical processes that occur within clusters, mainly shocks and AGN feedback, and how observations of them are essential for calibration of simulations.

After the discussion of the cosmological and astrophysical background associated with clusters, we turn to how clusters are observed at millimeter wavelengths. We introduce the Sunyaev-Zeldovich (SZ) effect which is the backbone of observing clusters at millimeter wavelengths. We discuss arcminute wide-scale observations of clusters with CMB telescopes, and targeted arcsecond scale follow-up observations of those clusters with high-resolution instruments. Along with describing those observations, we discuss some of the science outcomes that they produce. Thus demonstrating why studying clusters is poignant for understanding the nature of the universe.

2.1 Galaxy Cluster Formation

According to the ΛCDM standard model of cosmology, the current best cosmological model that describes our universe, clusters are the result of an extraordinary process that started with a nearly uniform matter field with random quantum-scale fluctuations. These were blown up to macroscopic scales by inflation. Once the energy density from matter began dominating the universe, those fluctuations began to grow and regions where the matter density was above a critical density collapse into halos in a finite time. Those halos are hosts to the galaxies we observe in the universe today, and the most massive halos became galaxy clusters.

With some assumptions, the abundance of clusters with a particular mass that form as a result of the above process can be derived analytically. We will outline some of the steps to analytically deriving the cluster mass function below, however reality does not often conform to simple analytical calculations. That is where simulations of cosmological large scale structure formation come into play. These simulations can include gravitational merging effects and hydrodynamical processes that cannot be captured in pencil-and-paper work. We will review how the cluster mass function as computed via simulations differs from the analytical results.

2.1.1 Structure Growth and the Halo Mass Function

The mass function of galaxy clusters can be derived using linear perturbation theory. In this formalism one is concerned with density perturbation in the matter field above the average, $\delta = \frac{\rho}{\bar{\rho}} - 1$. Given the expansion of the universe from the Friedmann equations one finds that spherically symmetric density perturbations will expand to a finite size and then collapse. Given that collapse time, one finds that the critical density above which spherical perturbations are guaranteed to collapse is $\delta_c \sim 1.68$. While there is some subtleties regarding whether one is considering the Friedmann equations for either a flat universe with

or without a cosmological constant, the dependence caused by that is subdominant to the matter density dependence, and so for most cosmologies $\delta_c \sim 1.68$ is a good approximation for the critical density for collapse [1].

This result means that given a linear density perturbation field, which is growing during the matter domination era of the universe, one can identify which perturbations will collapse to a form a virialized halo. This underpins the assumptions that Press and Schechter used to analytically derive the cluster mass function [2]. We follow the steps given in [1]. They posited that given a perturbation field that is smoothed with a spherical top-hat and has a mass variance σ, the probability that a perturbation is above the critical density for collapse is given by integrating a normal distribution

$$P(\delta_s > \delta_c) = \frac{1}{\sqrt{2\pi}\sigma} \int_{\delta_c}^{\infty} \exp\left(\frac{-\delta_s^2}{2\sigma^2}\right) d\delta_s = \frac{1}{2}\mathrm{erfc}\left(\frac{\delta_c}{\sqrt{2}\sigma}\right)$$

Where erfc is the complementary error function. This result then becomes the fraction of halos above a mass. Press and Schechter introduce a factor of two when relating this probability to the fraction of halos of above a mass, due to the result of the calculation not ending up with what has to be the correct answer. In the above relation, if $\sigma \to \infty$, so considering an infinite mass variance where one would expect all perturbations to collapse, $P(\delta_s > \delta_c) \to \frac{1}{2}$, not 1 as expected. Press and Schechter thus introduce a "fudge factor" so that the answer becomes 1. This is because the above argument neglects underdense regions within the overdensities. There has been more sophisticate work on the population of collapsed halos that arrive at the same result as Press and Schechter but without introducing the fudge factor [3].

The cluster mass function, or the number of halos with mass M in a dM wide bin, derived by Press and Schecter is given as [1]

$$n(M,t)dM = \sqrt{\frac{2}{\pi}} \frac{\bar{\rho}\delta_c}{M^2\sigma} \exp\left(\frac{-\delta_c}{2\sigma^2}\right) \left|\frac{d\ln\sigma}{d\ln M}\right| dM$$

All of the dependencies on cosmological parameters, the dark matter density and the primordial distribution of matter, are contained in the mass variance, σ, in the above expression which is essentially a windowed matter power spectrum. With this result one can then constrain those cosmological parameters simply by counting the number of halos, determining the cluster redshift, and measuring their mass.

2.1.2 Galaxy Cluster Formation in Simulations

The previous discussion on the Press-Schechter halo mass function was entire based on a simple model of spherical collapse of top-hat density perturbations. The real world does not fit into this simple box. Comparing the Press-Schechter mass function to simulations and real world data finds that it under-predicts the number of massive halos and over-predicts the number of less massive one [4]. Therefore work must be done to better connect cosmological parameters to the number count of observed clusters. Cosmological simulations are the best way to do that.

Simulations can include dynamics that is as simple gravity-only N-body, up to complex hydrodynamics within forming halos. The more sophisticated simulations are important for determining the cluster mass function, as the energy that is injected into halos via hydrodynamical processes are the type of effects that analytical calculations miss. Modern simulation codes like `ART` and `GADGET` have been used to generate populations of cluster and then functional form of the cluster mass function are fit to those populations. [5]. These outperform the Press-Schechter mass function. That Tinker et al. 2008 result shows that functional forms can be fit to simulated clusters but highlights the difficulty of making a single universal cluster mass function that is accurate to less than 5%. Therefore simulations are needed to inform how differences from universality occur.

We will conclude by pointing out that cosmological simulations are only getting better. The last decade has seen non-radiative hydrodynamic simulations, like `GADGET`, make

images of clusters that appear real [6]. Current progress in adding in radiative processes has made realistic galaxy-scale images [7, 8]. The Illustris-TNG project intends to make a cosmological-scale simulation that includes radiative processes and magnetohydrodynamics [9]. All of these next-generation simulation efforts will greatly expand the understanding of the population of galaxy clusters by including more realistic astrophysical phenomena. With the inclusion of those effects though it will become more important to have an understanding and constraints of those effects in real-world clusters.

2.2 Galaxy Cluster Astrophysics

The hydrodynamical processes that occur within clusters give the advantage to simulations at determining the cluster mass function. These include feedback mechanism within clusters such as shock heating, star formation, and AGN feedback. We discuss some of those mechanisms in this section and review their current best observations.

2.2.1 Shocks in Clusters

In the previous parts of this chapter, we discussed clusters as the spherical collapse of the matter distribution but once those halos collapse they still interact with one another. This is the picture of hierarchical structure formation, that small over-densities collapse first and build up to cluster-scale over-densities. As the merging halos become more and more massive effects from the mergers become more pronounced. These mergers are some of the most energetic events in the universe and the energy from those events manifests itself in shocks and turbulent mixing in the ICM. Those processes heat up the ICM to energies that match the gravitational potential of the cluster [10]. Shocks manifest as discontinuities in the temperature in the ICM, this can be seen in the X-ray and is observed in objects like the Coma cluster and the Bullet cluster [11, 12].

In addition to the cataclysmic shocks from cluster mergers there are also shocks and cold

fronts that occur from the infall of matter from the cosmic web into the cluster. These types of shocks have high Mach number as the infalling gas from filaments are very cold compared to the gas in the ICM. They are thought to be one of the mechanism that drives heating in even relaxed clusters that have not undergone mergers recently and prevents runaway cooling in the ICM [13]. Moreover, shocks within cluster and particularly the ones from cosmic accretion could also drive cosmic ray acceleration [14].

Shocks from the dynamic mixing of gas in clusters is a well studied phenomenon and is one of the most energetic processes within clusters. Studying those processes is interesting in terms of the gas physics within clusters and is important to make simulations of clusters more realistic.

2.2.2 AGN Feedback

The high-energies contained in shocks from mergers and cosmic accretion can be matched by the energy injected into the ICM through AGN feedback. AGN are supermassive black holes in the center of galaxies. These black holes accrete a gargantuan amount of matter and produce high-energy jets [15]. Those jets are extremely energetic and blow energy into the ICM. This is another process that is theorized to prevent runaway cooling in cluster cores. As the hot gas in the ICM cools, it more easily accretes into the black hole which then causes the black hole to have an outburst of jets. That outburst heats up the ICM and arrests accretion onto the black hole until the gas cools and the process repeats [16].

The importance of the energy AGN inject into the ICM cannot be understated and is why many simulations aim to include this process. Therefore, observations of AGN feedback are important for the purpose of calibrating their role in simulations and how that feedback scales with cluster properties such as cluster mass and the mass of the central galaxy.

2.3 Observing Galaxy Clusters at Millimeter Wavelengths

Galaxy clusters are made of both baryonic matter and dark matter. Imaging clusters at different wavelengths is sensitive to complimentary baryonic physics and provides complimentary tracers for the dark matter. At visible and infrared wavelengths, the starlight from cluster member galaxies can be imaged. This light probes the positions and shapes of galaxies within the cluster which are expected to trace the dark matter halo.

The distribution of dark matter in clusters can be studied by observing optical and IR emission from galaxies that are in the background of clusters. As the light from these background galaxies travels toward Earth, it is gravitationally lensed by intervening matter. This effect is especially pronounced if there is a cluster between the background galaxy and Earth as the dark matter density in clusters is as large as it can be in the universe. Weak lensing is the minute magnification and shearing of background galaxies due to a cluster's dark matter distribution. This area of study has been successfully used to image the dark matter distribution in clusters.

At X-ray wavelengths, the thermal bremsstrahlung from the electrons that are in the ICM is visible. This radiation comes from the interaction of electrons with ions in the low density gas between clusters that has a typical temperature of $10^7 - 10^8$ K. Observations of clusters at these wavelengths are critical for cosmological analyses that relate to the cluster mass function as the total integrated emission from the ICM is a good proxy for the total mass of the cluster.

In a similar vein, the electrons in the ICM can also scatter background light which produces a measurable probe of the ICM at millimeter wavelengths. In this section, we introduce that scattering process, the Sunyaev-Zeldovich effect, and describe how observing clusters via that effect can advance the understanding of the universe and the thermodynamical processes in the ICM.

2.3.1 The Sunyaev-Zeldovich Effect

The observation of galaxy clusters via a secondary anisotropy of the Cosmic Microwave Background (CMB) was first posited by Sunyaev and Zeldovich in 1970 [17]. The basic premise of the SZ effect is that CMB photons are scattered by energetic electrons found in the hot gas constituting the ICM through an inverse Compton scattering process. The interactions with the electrons in the ICM causes a shift in the blackbody spectrum of the CMB photons that has a unique spectral signature.

The SZ effect predicts a redshift independant, athermal shift in the CMB blackbody spectrum [18]. This shift is related to the pressure of the electrons in the ICM integrated along the line-of-sight. It is referred to as the thermal SZ effect (tSZ) and can be written in the non-relativistic limit as

$$\frac{\Delta I}{I_0}(\nu) = y \frac{x^2 e^x}{(e^x - 1)^2} \left(x \frac{e^x + 1}{e^x - 1} - 4 \right)$$

where $x = h\nu / k_B T_{\rm CMB}$ which contains the CMB temperature, $T_{\rm CMB} = 2.7$ K, and y is referred to as the Compton y parameter which is the electron pressure integrated along the line of sight given by

$$y(\theta, \phi) = \frac{\sigma_T k_B}{m_e c^2} \int dl \; n_e(\theta, \phi) T_e(\theta, \phi)$$

where σ_T is the Thomson cross section, $m_e c^2$ is the rest mass of the electron, n_e the is electron number density, and T_e is the electron temperature in the ICM. A consequence of the spectral shape of the tSZ effect is at frequencies lower than 220 GHz there is a decrement in the CMB flux, at frequencies higher than 220 GHz there is an increment in CMB flux, and at 220 GHz there is a null in the effect. Typical values of Compton y are of the order 10^{-4} making the decrement at 150 GHz of order -0.1 MJy/sr and the increment at 280 GHz of order 0.1 MJy/sr. Since the SZ effect is due to a shift in the spectrum of CMB photons and not direct emission from the cluster it does not suffer from cosmological dimming. Therefore,

high redshift clusters can be detected via the SZ effect.

In addition to the tSZ effect, there is the kinematic SZ (kSZ) effect which is due to the bulk motion of the cluster and its substructure. This doppler shifts CMB photons either postively or negatively depending on the velocity of the electrons. Since this is only a doppler shift the kSZ keeps the same spectral shape as the CMB but the intensity is either minutely increased or decreased. The kSZ shift in CMB blackbody spectral intensity is given by

$$\frac{\Delta I}{I_0}(\nu) = -\tau_e \left(\frac{v_{\rm pec}}{c}\right) \frac{x^4 e^x}{(e^x - 1)^2}$$

where $v_{\rm pec}$ is the line of sight motion of the free electrons in the cluster, τ_e is the optical depth due to the electrons, and x is the same as given above for the tSZ effect. Typical values of $\tau_e \, v_{\rm pec}/c$ are order 10^{-5} making the spectral distortions of this effect an order of magnitude smaller than the tSZ effect.

Figure 2.1 illustrates the spectral distortion to the CMB by the tSZ and kSZ effects for typical values of Compton y, $v_{\rm pec}$, and τ_e. The figure shows that the magnitude of the effect is most prominent from 50 GHz to a little above 400 GHz. However the effects from relativistic electrons are not shown in that figure which typically causes a smaller decrement between 50 and 220 GHz and a broader increment from 220 up to 600 GHz [19].

2.3.2 Cosmology with Wide-Field Cluster Surveys

To constrain the cluster mass function described in section 2.1.1, the mass of many clusters need to be measured. To realize this goal, one would ideally like to image a large fraction of the sky to great depth in the millimeter bands to build a mass limited cluster catalogue. Fortunately, this survey design is identical to CMB surveys which image in the bands needed for measurement of the SZ effects. What follows is a description of how CMB surveys make catalogs of galaxy clusters and constrain cosmological parameters with those catalogs.

CMB instruments with arcminute resolution have been surveying hundreds to thousands

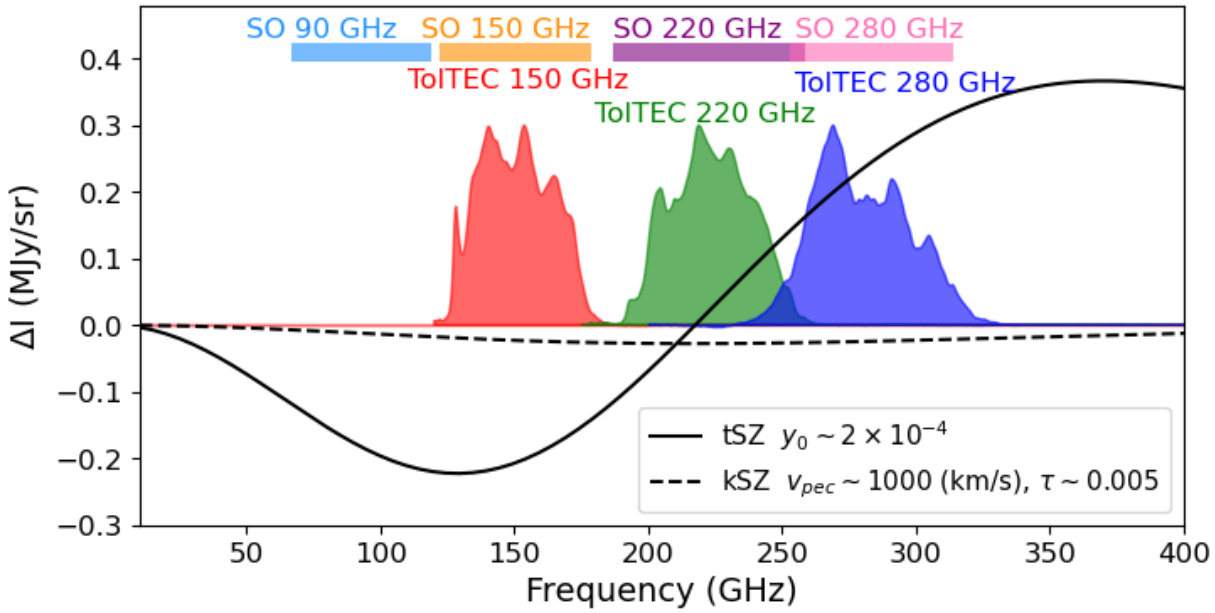

Figure 2.1: Shift in CMB spectral intensity due to the tSZ and kSZ effects for typical values of Compton y, peculiar velocity, and optical depth. Measured TolTEC bandpasses are overlayed to represent its sensitivity to the effects. SO band edges are plotted to show how they compliment the TolTEC bands.

of squared degrees of the sky since the early 2010s. Two of the most impactful CMB instruments of this kind are the South Pole Telescope (SPT) and the Atacama Cosmology Telescope (ACT) [20, 21]. Since 2007, these instruments have mapped thousands of square degrees of the sky from the South Pole and the Atacama Desert. From those maps, they have discovered thousands of galaxy clusters over a broad range of masses and redshifts [22–24].

Clusters are discovered by those experiments by exploiting the frequency dependence of the tSZ effect described in section 2.3.1 and the instruments' beam. Except for the closest clusters like Coma and Virgo, the angular extent of clusters on the sky are of the order of a few arcminutes which is at the beam scale of ACT and SPT. Figure 2.2 shows a subset of the ACT field at 150 GHz [25]. In that map there are clusters located at roughly (-162, -1.1) and (-150, 2.8). One can see that clusters appear as negative point-like sources in these maps. A matched filter can be implemented on the maps to identify these clusters and quantify the significance of the detection.

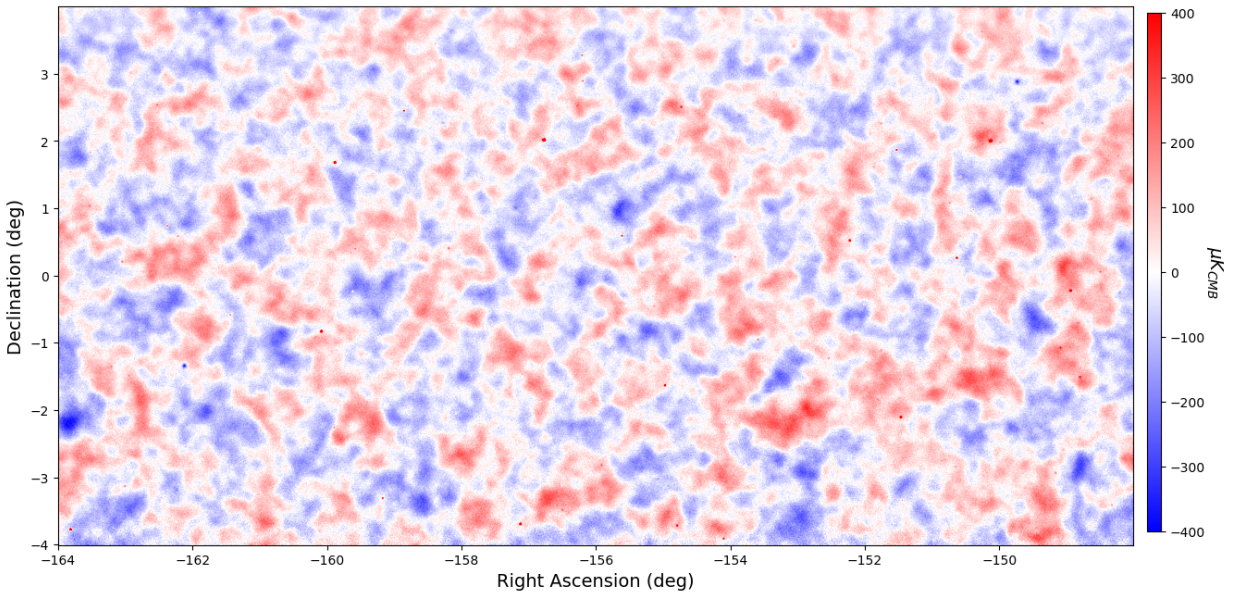

Figure 2.2: A subset of the ACT map of the sky at 150 GHz. There are clusters at roughly (-162, -1.2) and (-150,2.8) and appear as negative point sources.

ACT uses a multifrequency matched filter that incorporates the instrument beam, the map noise at different frequencies, the spectral shape of the tSZ effect, and the expected angular profile of the clusters based on a universal pressure profile [26]. This allows for a more robust detection of clusters by leveraging the two different photometric bands at which ACT is most sensitive. The map-based cluster finder is tested with simulated clusters injected into the maps and for cluster masses greater than roughly 4×10^{14} $M_{\odot}$ the ACT catalog is 90% complete for redshifts greater than roughly 0.2 [24]. It is necessary to confirm that the clusters identified are actually clusters and not false positives. This is done by cross reference with cluster catalogs from optical observatories such as the Dark Energy Survey (DES). The redshift of the clusters are also retrieved from the optical catalogs. The maps are then match filtered with a common 2.4 arcminute filter which corresponds to a fixed cluster mass at a fixed redshift. This allows for the estimation of the cluster mass using a scaling relation.

Scaling relations are a vital part of cosmological analyses with clusters. The integrated

Compton y value that is measured via the SZ effect is a good proxy of the cluster mass however it does not directly measure the cluster mass. Instead an empirical scaling relation between the integrated Compton y signal and the cluster mass is employed [27, 28]. Within these scaling relations there is generally scatter at the tens of percent level, so the scaling relations are generally accepted to be the limiting systematic to performing cosmological analyses with SZ clusters.

To place constraints on cosmological parameters like σ_8 and Ω_M a model that relates cluster number counts to those parameters is required, such as the Press-Schacter mass function or a cluster mass function from simulations [2,5,29]. With those models a likelihood can be made to marginalize over cosmological parameters as well as parameters in cluster mass-observable scaling relations.

One of the most constraining and recent cosmological analyses of SZ cluster is from the SPT collaboration [30]. This work also constrains the masses of clusters in the SPT catalog via weak lensing measurements from DES and HST, which reduces uncertainties associated with the Compton y cluster mass scaling relation by marginalizing over free parameters in that relation. To illustrate the constraining power clusters have on cosmology we show their results in figure 2.3. While the SPT result does not have tighter constraints on the matter content or the clumpiness of matter in the universe compared to those from Planck primary CMB measurements, it is competitive with other constraints from CMB lensing and optical surveys. The SPT constraints will only be improved with the inclusion of more data and improved mass and redshift estimates of the clusters in their catalog.

Wide-field surveys of the millimeter-wave sky naturally lead to catalogs of thousands of clusters. From those catalogs, along with some assumptions about observables and cluster masses, analyses can be performed that constrain important cosmological parameters like the matter content of the universe and the clumpiness of matter at a certain scale. The latter is an interesting parameter to constrain given the present disagreements between optical

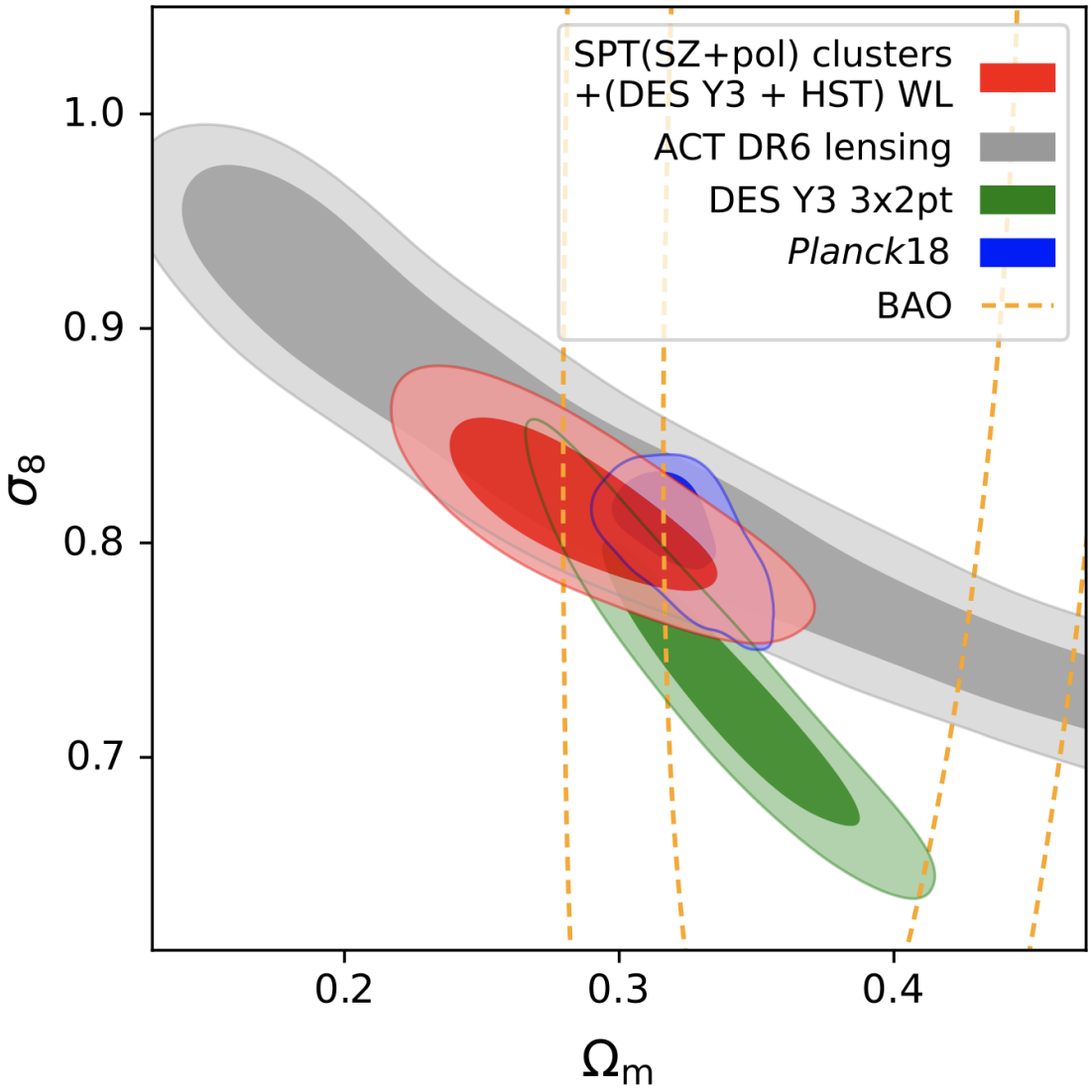

Figure 2.3: Constraints on Ω_M and σ_8 (68% and 95% credible regions) in a ΛCDM universe with massive neutrinos from the abundance of SPT clusters. Contours from ACT CMB lensing, DES lensing and shear, BAO, and Planck primary CMB analyses are shown for comparison [30].

determinations of σ_8 based on local measurements of galaxies and the value derived from the primary CMB anisotropy and ΛCDM [31]. This highlights the importance of wide-field cluster observations and with improving CMB instruments we anticipate a new paradigm of constraining cosmology with millimeter wavelength observations of clusters at arcminute resolutions.

2.3.3 Astrophysics with Targeted Cluster Observations

While the wide-field cluster surveys described in the previous section are useful for constraining cosmology with clusters, the limited angular resolution of CMB instruments means the internal structure in the ICM is not resolved. Studying resolved SZ observations of clusters can reveal interesting astrophysics within clusters as outlined in section 2.2 and help reduce scatter and systematics of scaling relations for cluster masses.

To resolve some of the effects that occur within the ICM, clusters need to be observed with instruments that have resolution on the order of 10 arcseconds or less. While instruments with that resolution exist, they usually do not have a large field of view, typically smaller than a quarter of a degree. That means those instruments are unable to efficiently survey the sky and instead must be used for targeted follow-up.

This creates a symbiotic relationship between wide-field millimeter surveys and high-resolution millimeter observatories. Clusters are discovered and cataloged with the surveys, confirmed via optical observations, and then clusters with promising features are followed up with high-resolution instruments. The high-resolution observations of clusters can identify features in clusters that are unresolved by arcminute-scale observations that can potentially cause systematics in estimating the cluster mass. We outline a few results from high-resolution millimeter-wave observations of clusters made by MUSTANG [32] and Bolocam [33] to showcase the astrophysics that can be probed from high-resolution measurements of cluster and how those observations can improve measurements of clusters at low resolution.

First let us consider Abell 1835, a cluster that is observed both with arcminute resolution by ACT and with 9 arcsecond resolution with MUSTANG. This cluster has a particularly bright SZ decrement which has made it a target of many observatories [34, 35]. The cluster decrement appears in the ACT maps at 90 and 150 GHz, and there is no detection of the cluster at 220 GHz as expected from the SZ signal. The top row of figure 2.4 shows the multifrequency ACT maps. While the cluster appears to be unassuming in the ACT maps,

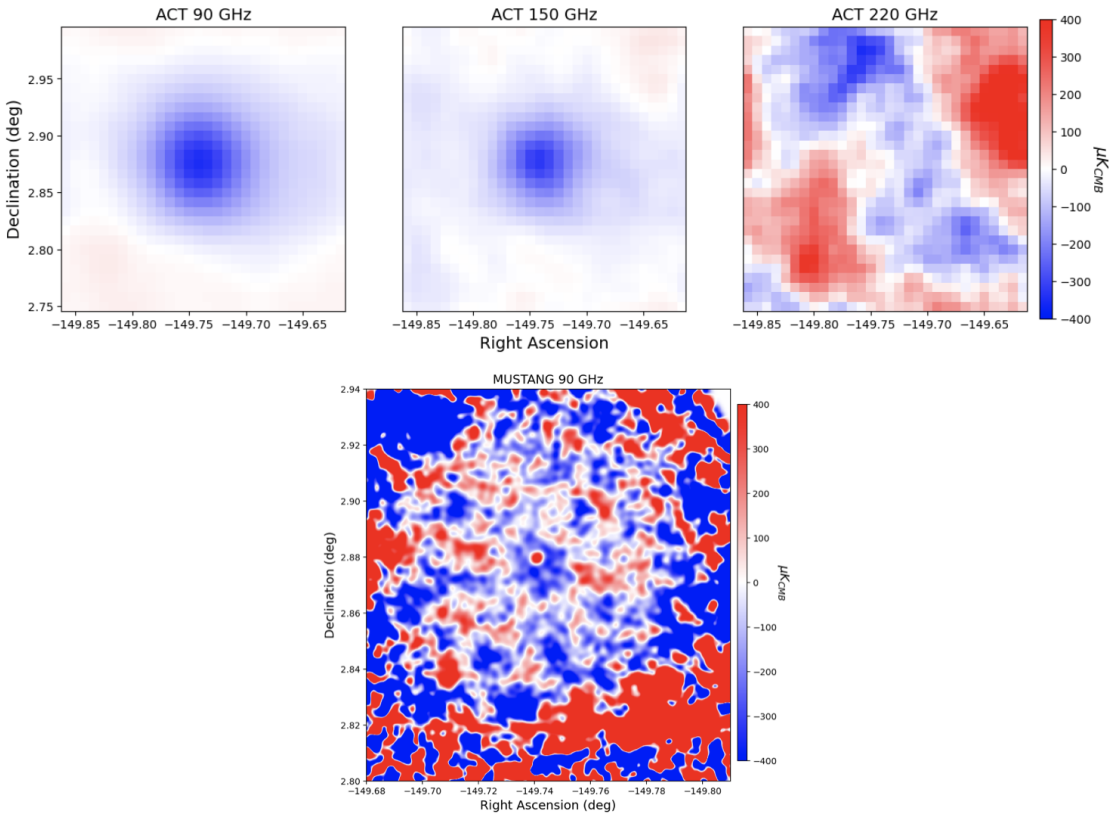

Figure 2.4: (Top) ACT maps of Abell 1835 at 90, 150, and 220 GHz. The 90, 150, and 220 GHz maps have been smoothed with respective instrument beams of 2.1, 1.4, and 1.0 arcmin FWHM. (Bottom) MUSTANG map of Abell 1835 at 90 GHz [36]. This map was smoothed with a 9 arcsec FWHM beam.

MUSTANG observations of Abell 1835 show there is a bright radio source in the cluster [36]. This is shown in the bottom of figure 2.4. The noise in the MUSTANG map is quite high so the cluster decrement is not as prominent, but it is clear that there is a bright point source in the cluster. Additional observations of the cluster made with Bolocam at 273 GHz unambiguously detect the SZ effect increment but also detect bright lensed sub-millimeter galaxies [35].

The detection of lensed sub-millimeter galaxies are interesting in their own right and are an example of the astrophysics that can be achieved via high-resolution imaging of clusters. Moreover, the observations from Bolocam also highlight the importance of imaging clusters at high resolution and at higher frequencies where the emission from dusty star forming

galaxies (DSFGs) is more prominent. In the case of Abell 1835, the bright source that is several hundred μK biases the Compton y signal. This bias can be handled in the ACT maps by leveraging multifrequency maps simultaneously as the point source spectral energy density will be different than the tSZ spectral shape, but given that most of the sensitivity is concentrated in the 90 and 150 GHz bands such a mitigation is not presently effective.

A systematic study of point sources contaminating the signal recovered by ACT observations of clusters was presented in Dicker et al. 2021 [37]. They show that sources impact the recovered Compton y signal by 10% and can even result in non-detections of low mass clusters with particularly bright point sources. They conclude in the necessity for high-resolution observations of clusters to understand source properties.

High-resolution observations of clusters trace phenomena within the ICM. The hot gas that makes up the ICM has been shown in X-ray observations to trace a range of processes such as AGN feedback in the cluster [38], shocks from mergers [39], and have even been used to show the existence of collisionless dark matter [11, 40]. Since SZ observations trace the same physics, hot electrons in the ICM, it can observe similar phenomena but has a few distinct advantages. For one, X-ray emission from the ICM is proportional to the square of the density of electrons in the ICM whereas the SZ effect is linearly proportional to the electron density. This means that the SZ effect can image the ICM at the cluster outskirts where effects from mergers and infall from cosmological accretion are more prominent [41]. Since the SZ effect is a scattering process and not direct emission it does not suffer from cosmological dimming which means clusters can be observed at higher redshift.

These advantages have lead to incredible images of phenomena within clusters. One example of how high-resolution images of cluster reveal information about clusters undergoing mergers comes from NIKA2's images of MACS J0717.5+3745 [42, 43]. NIKA2 observes at 150 and 260 GHz with 17 and 10 arcsecond resolution in those respective bands, so it is able to spatially resolve both the tSZ and kSZ effects within clusters. Figure 2.5 shows the

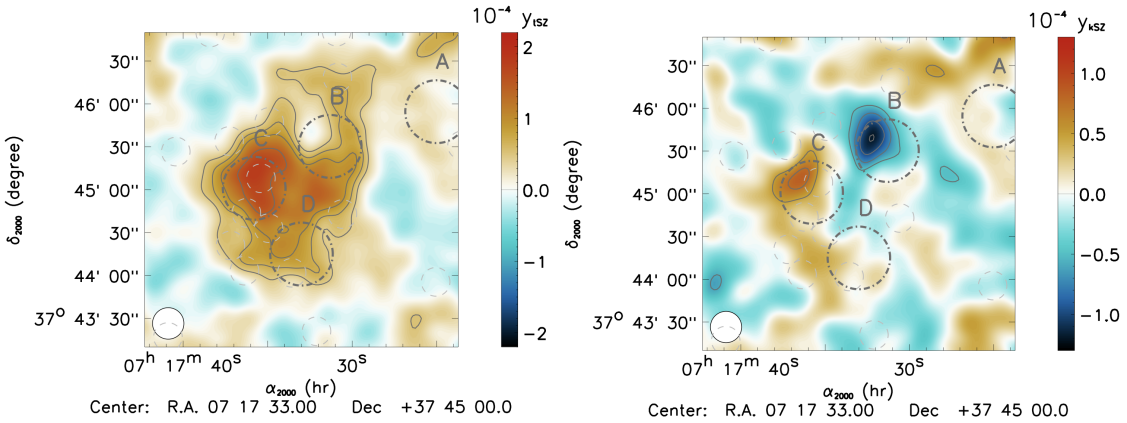

Figure 2.5: (Left) Map of the Compton y from the tSZ effect in MACS J0717. (Right) Map of the kSZ Compton y in MACS J0717. Figure from [43].

tSZ and kSZ maps derived from NIKA2 data. The kSZ map shows the velocity structure of merging systems directly imaged at millimeter wavelengths. The negative kSZ values near the B sub-cluster and the positive values ear the C sub-cluster are at the two sigma level so this maps is actually resolving hot gas in the ICM moving away and towards the observer respectively.

The SZ effect is not limited to probing cluster mergers, another example of high-resolution SZ measurements probing high-energy phenomena in clusters is from MUSTANG2 observations of MS0735.6+7421 [32, 44]. This cluster has energetic jets from an AGN. Those jets are bright in the radio and they produce cavities in the x-ray emission [45]. Observations of processes like these are vital to understanding how AGN heat cluster cores and limit cooling in clusters [46]. MUSTANG2 observations of MS0735 also show evidence of cavities as seen in figure 2.6. The exciting prospect of the agreement between the cavities seen by MUSTANG2 and X-ray observations is the ability for SZ observations to potentially image effects like this at a higher redshifts where integration time of X-ray observations is not feasible which would constrain feedback effects across the history of cluster formation and evolution. Such observations would help clarify how AGN feedback limits cooling in clusters and if other processes are needed to prevent runaway cooling in cluster cores.

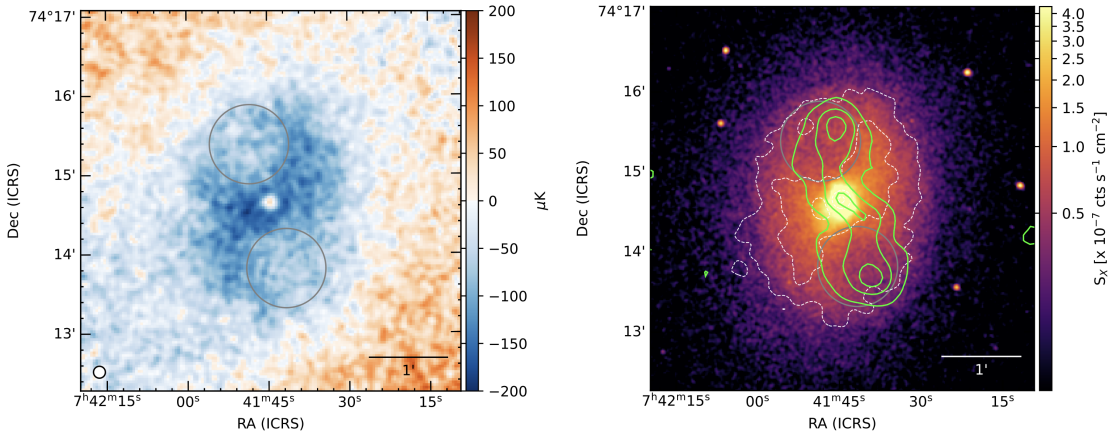

Figure 2.6: (Left) Map of the Compton y from the tSZ effect in MS0735 made by MUSTANG2 with grey circles denoting the cavities identified in the X-ray. (Right) Map of the X-ray emission from *Chandra* with MUSTANG2 tSZ contours overlaid in white. The green contours denote the radio emission. Figure from [44].

High-resolution images of clusters also constrain scales that energy is injected into the ICM. This can be done by studying the fluctuations of pressure around the smooth universal pressure profile [26]. One example of this analysis was done with X-ray observations of the core of the Coma Cluster [47]. The authors there found deviations around the universal pressure profile that are consistent with pressure fluctuations and attribute the cause to turbulent mixing of ICM gas among other possibilities. This analysis was repeated with SZ observations of Coma made by *Planck* [48]. Those authors find that the injection scale of fluctuations in Coma is roughly 500 kpc. That scale combined with the associated Mach number leads the authors to claim that the fluctuations are consistent with driving due to mergers. The SZ studies of pressure fluctuations in Coma represent the first use of SZ observations to constrain turbulence in clusters in that fashion.

The Coma cluster is relatively close to Earth, so the pressure fluctuations can be resolved with *Planck*. To image pressure fluctuations in more distant clusters, sensitive higher-resolution SZ measurements are needed. This was demonstrated by members of the MUSTANG2 collaboration for the cluster Zwicky 3146 which is one of the MUSTANG2 clusters that has the most integration time [49, 50]. The authors of that study found that, when

considering X-ray and SZ data, the innermost core of the cluster has fluctuations that are consistent with sloshing and could be explained with cavities due to AGN feedback. The signal-to-noise in the SZ measurements of fluctuations for Zwicky 3146 in the outermost parts of the cluster were not good enough to constrain much so the X-ray measurements were more impactful.

These studies of pressure fluctuations show promise in constraining the turbulence in the gas in the ICM. The study of gas dynamics within the ICM is important for calibrating hydrodynamical simulations of clusters which are in turn important for the cosmological analyses previously described. This field of study with the SZ effect will rapidly mature as TolTEC begins cluster observations.

CHAPTER 3

INSTRUMENTS

It is practically impossible to build a single millimeter-wave telescope that can both survey the entire sky to discover galaxy clusters and have high enough angular resolution to resolve the arcsecond-scale features within those clusters. The practical solution is to use two telescopes of different capabilities. One telescope with a large field of view (FOV) surveys large fields on the sky at arcminute resolution to create a mass limited catalog of clusters. The other telescope would have arcsecond angular resolution and make targeted follow-up images of the more interesting clusters identified by the first telescope.

In order to extract the highest fidelity cosmological constraints from a arcminute - resolution millimeter-wave cluster catalog, sub-beam scale systematics need to be understood and constrained through targeted follow-up observations by the arcsecond resolution telescope. The arcminute resolution maps can be combined with the arcsecond imaging to produce maps with high fidelity over the full range of angular scales.

In this chapter we present two instruments that fit nicely requirements outlined above: the Simons Observatory Large Aperture Telescope (SO LAT) [51] and the TolTEC camera on the Large Millimeter Telescope (LMT) [52]. We provide overviews of these instruments including their beam sizes and FOVs, their detector properties, and the location of the instruments. We pay particular attention to the state-of-the-art hardware, such as the optics and detectors, that go into those instruments and make them the next-generation cluster imaging telescopes.

3.1 The Simons Observatory Large Aperture Telescope

The Simons Observatory (SO) consists of four telescopes, a 6-meter Large Aperture Telescope (LAT) and three half-meter aperture Small Aperture Telescopes (SATs). The SATs are

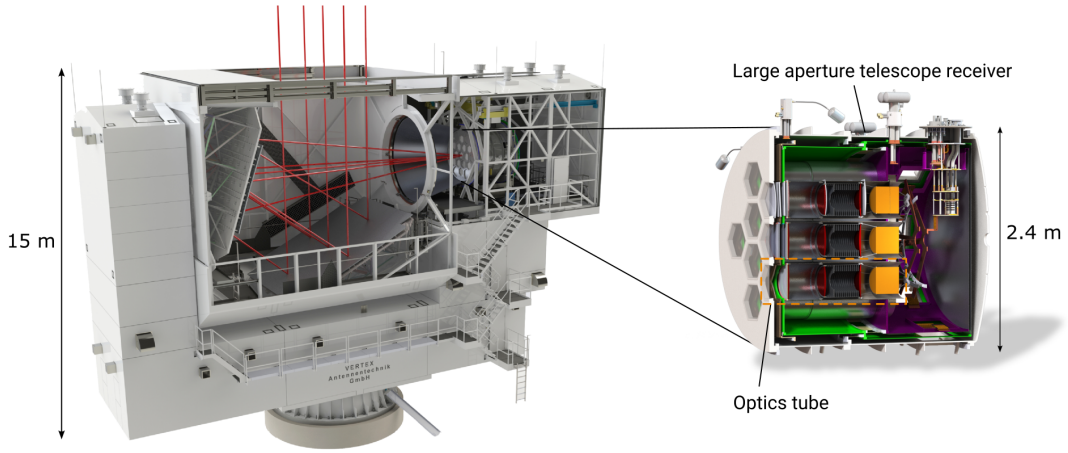

Figure 3.1: (Left) A model of the SO LAT. (Right) A model of the LAT receiver with a cutaway showing the modular optics tubes and the cold optical elements it contains.

optimized for searches for inflationary gravitational waves and other CMB-specific science goals and do not have the resolution needed for imaging of galaxy clusters. The LAT, with its arcminute-scale beam will be incredible for observing clusters.

The 6 meter LAT will observe the sky with a 7.8° diffraction limited field-of-view (FOV) and 2 arcminute resolution at 90 GHz [53]. This is achieved with a state-of-the-art optical design that will usher in a new generation of millimeter-wave observations. Figure 3.1 shows a model of the LAT and its cryogenic receiver which contains reimaging optics and detectors. It will observe in three different dichroic bands centered at 20/40 GHz (the Low Frequency bands, or LF), 90/150 GHz (the Mid-Frequency bands or MF) and 220/280 GHz (the Ultra High-Frequency bands or UHF). At those frequencies, the SO LAT is leading the field in several areas: The 280 GHz channel will be the highest frequency band deployed for a large-scale CMB survey; The number of detectors observing at those frequencies will be the most ever deployed in one telescope at these frequencies, leading to a near order of magnitude improvement over what has previously been deployed.

That impressive sensitivity means that the SO LAT is an ideal instrument to survey galaxy clusters via the SZ effect. We highlight the location of the telescope, its optical

design, and detector technology and they contribute to cluster observations. We conclude this section with the status of instrument and a time frame for when observations will begin.

3.1.1 The SO Site

The SO LAT is being constructed in the Atacama Desert in Northern Chile. It is situated near the peak of the Cerro Toco at an altitude of nearly 5200 meters. This area has been home to millimeter-wave telescopes for nearly two decades. The SO project is significantly larger in scale than the previous and current observatories on Cerro Toco. Construction on the SO site began in 2020. Instruments began being deployed at the site in 2023. Figure 3.2 shows the SO site in Fall 2024. The unfinished LAT is the leftmost structure in that figure. Construction of SO will be completed by the end of 2024 with all of its instruments coming online in 2025.

The majority of the sky can be seen from this site. The LAT will leverage this to observe more than 40% of the sky which is vital for building the large catalog of galaxy clusters required for cosmological analyses [54].

The Atacama Desert is incredibly dry. This is important because water vapor in the atmosphere absorbs and re-radiates light at millimeter wavelengths. This increases loading on detectors and adds large scale correlated noise in images which degrades sensitivity at large scales. The atmospheric transmission and brightness temperature for the SO site are shown in figure 3.3. The curves presented in that figure were generated using the atmospheric code *am* [55]. The different percentiles correspond to the water vapor present in the atmosphere, so the 5th percentile corresponds to some of the lowest water vapor present in the atmosphere whereas the 50th percentile is the average atmospheric water content. The coverage of the SO bands are overlaid in color. One can see that they were chosen to avoid the strong absorption features in the atmosphere due to water and oxygen lines.

The two key aspects encapsulated in figure 3.3 are the high atmospheric transmission

Figure 3.2: A picture of the SO site in the Atacama desert. The SO LAT is leftmost structure in the image. Another millimeter-wave telescopes, the Cosmology Large Angular Scale Surveyor, located in the foreground.

and the low brightness temperature. The atmospheric transmission being above 80% for all the photometric bands, even on a median day, means that a significant number of astrophysical photons reach the LAT. Since the LAT detectors are photon noise limited this means that the telescope is more sensitive. This is especially important at frequencies above 200 GHz where the atmospheric transmission begins to fall. In addition to high transmission, the atmospheric brightness temperature at the SO site is relatively low, between 5-20 K depending on the frequency with ideal water vapor content, compared to typical everyday atmosphere's brightness temperature, for example above Cambridge, Massachusetts the brightness temperature is between 20-60 K over the same frequency range. The significant

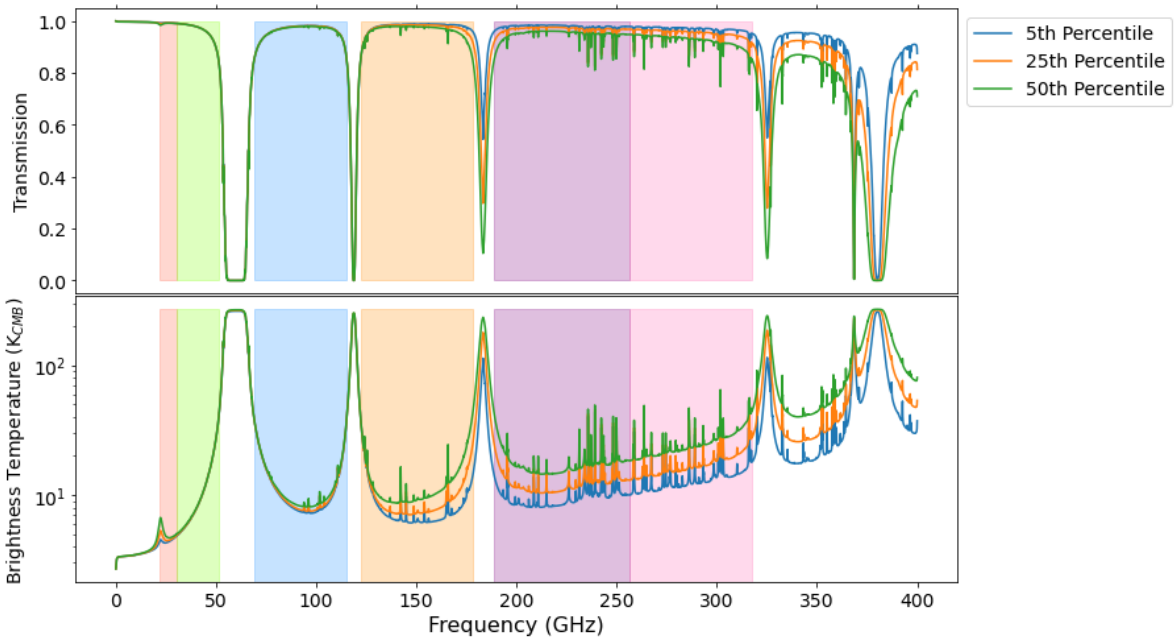

Figure 3.3: Plot of the atmospheric transmission (top) and brightness temperature (bottom) at the SO site atop Cerro Toco. The SO photometric bands are represented with the colored boxes. The percentiles refer to the amount of water vapor in the atmosphere.

reduction in atmospheric brightness temperature strongly supports the rationale for placing SO in the Atacama Desert. This reduction implies lower loading on the detectors, which in turn enhances sensitivity to astrophysical radiation. This is important since the atmospheric emission dwarfs the order 100 μK signal expected from galaxy clusters.

3.1.2 Optics

The SO LAT uses a system of warm and cold optical elements to direct light from the sky onto the detectors. The warm optical system consists of the primary and secondary mirrors. The cold optics are more complex and consists of metal mesh filters, alumina IR blocking filters, and silicon lenses. The cold optics are packaged in modular units called "optics tubes." The tubes contain the detectors that observe the millimeter-wave sky.

Light from the sky first interacts with the warm optics. It is imaged on the primary,

reflected onto the secondary, and is then incident on the window of the LAT receiver. After it enters the receiver, the light passes through the cold optical elements and is finally imaged onto the feedhorn arrays that begin the universal focal module (UFM). The components of the UFM will be described in section 3.1.3. The rest of this section will describe the optical components between the sky and the UFM, and role those optics play in making state-of-the-art measurements of the millimeter-wave sky.

The LAT warm optics define the ultimate resolution of the telescope. The six meter diameter primary and similarly sized hyperbolic secondary result in a far-field beam full width at half maximum (FWHM) of 2.0, 1.2, 0.9, and 0.8 arcminutes at 93, 145, 225, and 280 GHz respectively. Those band edges are plotted along side the spectral shifts caused by the SZ effect in figure 2.1 and in that figure one can clearly see that the SO LAT has the correct frequency coverage to observe the SZ effect. Since the LAT will deploy the most detectors of any millimeter-wave observatory that drives a very large FOV requirement for the telescope. A crossed-Dragone design was chosen for the LAT [56, 57]. That arrangement satisfied the LAT FOV requirement and is compact enough to practically be constructed. To correct for aberrations at the observed wavelengths and maintain low cross-polarization, perturbations from the standard parabolic and hyperbolic conic sections were made to the primary and secondary surfaces respectively.

The primary and secondary mirror surfaces are composed of segmented aluminum panels, roughly 70 cm by 70 cm in size, that can individually be adjusted to achieve the desired surface shape. The panels themselves, their support structures, and their alignment are the largest contributors to the total wavefront error of the LAT [58]. The error budget from the combined tolerance of the mirror panels, support structure, and anticipated deformations due to gravitational sag, thermal contraction and expansion, and wind is roughly 15 microns. The required half wavefront error is 35 microns rms, this requires a panel setting error of 20 microns which can be achieved using photogrammetry.

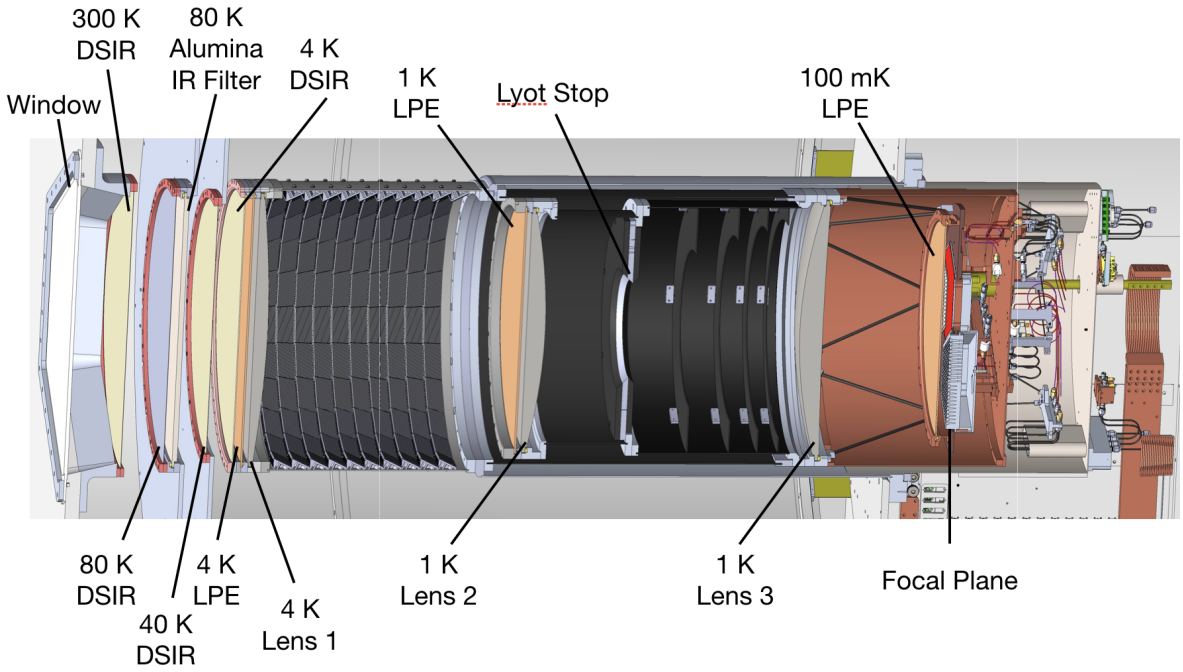

Figure 3.4: Model of a LAT optics tube with the optical components labeled and their corresponding temperatures.

The LAT warm optics direct and focus light onto the LAT receiver shown on the right side of figure 3.1. The LAT receiver is a 2.5 meter diameter cryostat that will be populated with up to 13 modular optics tubes [59]. The optics tubes are 40 cm in diameter and 130 cm long. They contain the cold reimaging optics that focus incident light onto the detectors. The reimaging optics also enable a larger field of view than what is possible with the primary and secondary mirrors alone, so they are crucial to achieve the LAT's goals of surveying a large area of the sky. Each optics tube contains similar optical elements, but with frequency band specific properties. For example, the anti-reflection coatings and freespace low-pass filter bandpasses are specific to the LF, MF, and UHF bands.

A model of a LAT optics tube is shown in figure 3.4 and shows the different filters, lenses, window, and stop contained in the optics tube. The path of light moves from left to right in that figure. First, light is incident on room-temperature the high-density polyethylene (HDPE) window and a double-sided infrared blocking filter (DSIR). The DSIR filters are

featured throughout the different cryogenic stages of the optics tubes. They are of the metal mesh design that has been featured on numerous previous millimeter-wave experiments [60]. These filters work by patterning sub-wavelength features onto plastic substrates and then stacking layers of these together to achieve transmission in the detector passbands, but reflect radiation at shorter wavelengths.

After the ambient-temperature elements, the light then enters the 80 K cryogenic stage through another DSIR filter and then passes through an alumina IR blocking filter. The alumina filters and their anti-reflection coatings are described in more detail in section 4.2. Alumina is transparent to millimeter wavelength radiation but absorptive in the IR [61, 62]. Those features, coupled with its high thermal conductivity, mean that alumina can absorb the incident IR light, and be operated at a cool enough temperature that they do not re-emit. This makes a good IR filter for millimeter-wave experiments to supplement the reflective DSIR filters. The alumina filters in the LAT also serve an optical purpose. The alumina filters in the optics of non-central optics tubes are wedged and act as a prism to slightly bend the light rays to be parallel to the central optics tube. This is necessary to reduce the footprint of the LAT receiver otherwise the angled optics tubes would require an infeasibly large cryostat.

Light then passes through a 40 K DSIR and onto the 4 K stage where it passes through a DSIR, a low-pass edge (LPE) filter which is based off the same metal mesh technology as the DSIRs [60], and the first lens. After the lens the light passes through the 4 K stage which has walls lined with custom metamaterial absorbing tiles that act as baffling to absorb scattered and stray light [63]. The next optical element encountered is the 1 K LPE and then the second lens. Light then passes through the blackened Lyot stop which is at 1 K and is essential to define the illumination of primary mirror. The stop produces 5.5 meter Gaussian illumination of the primary. This under-illumination of the primary produces sufficient resolution to achieve the science goals for the LAT.

The final optical element in the 1 K stage is the third lens. All three lenses are made of silicon. Silicon was chosen because its high index of refraction bends light more efficiently than other materials like HDPE. When cooled to cryogenic temperatures it is highly transparent at millimeter wavelengths. Previous millimeter-wave observatories, such as the Atacama Cosmology Telescope, utilized silicon lenses, and the SO LAT leverages experience that builds from that heritage, such as metamaterial anti-reflection coatings for the silicon optics which is described further in section 4.1 [64, 65]. The lens designs for lens 1 and 2 are plano-convex and concave-convex for lens 3. Each curved lens surface is a standard conic with higher-order aspheric terms which help to reduce aberrations.

Lastly, after lens 3 the light passes through a final LPE filter at 100 mK and then onto the UFMs. In all, the cold optics in the LAT optics tubes build on technologies that have been deployed on previous generations of millimeter-wave telescopes, but scale them up in diameter and quantity to achieve the LAT's science goals.

3.1.3 Detectors

The detector modules for the Simons Observatory are called universal focal modules (UFMs) [66, 67]. These consist of the elements that couple free space radiation onto the detectors, the detectors themselves, and the readout that turns individual detector signals into a multiplexed signal that is then transmitted to 300 K.

The LAT arrays use feedhorn-coupled OMTs as the antenna for coupling free space radiation to the detectors [68, 69]. Feedhorns are profiled waveguides that are designed to have low cross-polarization response across a wide bandwidth. In the case of SO, the feedhorn arrays are single blocks of aluminum with the feedhorn profile drilled into them. These are then gold-plated so the surface is an ideal conductor. The output of the feedhorn is a cylindrical waveguide that defines the low frequency edge of the first of the dichroic bandpasses. The output of the waveguide is coupled to an OMT antenna on a silicon wafer.

The OMT consists of two linear antennae that are oriented orthogonal to each other. This orientation enables the recovery of the intensity of linearly polarized light. There is a quarter-wave backshort behind the OMT to ensure maximal coupling to the antenna. The feedhorn and OMT are designed such that only the lowest waveguide mode is coupled between the two which ensures a simple beam pattern produced by the feed, in the time-reversed sense of light propagation.

The feedhorn-coupled OMTs transmit incident radiation onto planner transmission lines on a silicon wafer. Along these transmission lines, the two different dichroic frequency channels are split via a diplexer and then the two separate bandpasses are defined using on-chip filters [70]. On-chip filtering is achieved with stub filters and the filtered radiation is deposited onto a transition edge sensor (TES) [71, 72].

The TES bolometer has been a staple of astronomical millimeter-wave detection for over a decade. The principle behind this detector technology is to place a superconducting material below its critical temperature and then provide it with a bias voltage that places it right on the transition between superconducting and normal. The superconductor is then weakly coupled to a thermal bath. So when radiation transmits through the telescope and onto the superconductor, the energy from the light changes the resistance of the superconductor which is detected as a change in current. This results in an extremely sensitive bolometer that can detect picowatt-level changes in energy which makes them an ideal detector for millimeter-wave observations.

Since each pixel is dichroic and has two antennae to make it sensitive to linear polarization, there are four TES bolometers per pixel. At 420 pixels per detector array for the MF band and three arrays per optics tube, there are approximately 5000 detectors to read out of a single MF optics tube. To read these out SO is using a new multiplexing approach called microwave multiplexing, or μ-mux [73]. In this multiplexing scheme each TES is linked to an inductor in a resonance circuit. Each of these inductors have a different inductance so

each circuit has a different resonant frequency. When the signal from the TES is incident on the resonator, its kinetic inductance changes minutely which in turn changes its resonant frequency. Groups of 840 resonators, or half of the UFM, are combined onto a single transmission line that reaches from the UFM at 100 mK to outside the LAT receiver. A probe signal is then injected into that transmission line and the different resonant dips from the inductors is received. When the power on the TES changes, the resonant frequency for that inductor changes, which is measured as a shift in the dip on the transmission line. This readout scheme allows for a multiplexing roughly one thousand detectors per multiplexing unit. For each SO detector array there are two banks of resonators meaning that each detector array can be read out with just two sets of transmission lines.

The optical coupling, TES bolometers, and μ-mux readout comprise the SO UFM and enable observing the millimeter sky with unprecedented sensitivity. Table 3.1 summarizes the resolution, detector count, and total noise equivalent temperature (NET) of each SO LAT frequency channel [59].

Table 3.1: Summary of the SO LAT detectors based on the designed parameters.

Frequency	**Angular Resolution (arcmin)**	**Detector Count**	**Total NET (μK$\sqrt{\text{s}}$)**
27 GHz	8.4	222	48.4
39 GHz	5.4	222	25.7
90 GHz	2.0	10,320	5.4
150 GHz	1.2	10,320	6.7
220 GHz	0.9	5160	15.0
280 GHz	0.8	5160	35.9

3.1.4 Instrument Status

The SO project was conceived in 2019 and construction of the site and the instrument's elements began in 2020. As of early 2024, the bulk of the LAT is completed. The telescope structure is complete, the LAT receiver is in the telescope, and the receiver has been cooled

Figure 3.5: A photo of the LAT taken in April 2024.

down. A photo of the LAT at the site in April 2024 is shown in figure 3.5. The receiver currently contains all of the MF and UHF optic tubes. Dark testing of the detectors and readout system, which is a useful end-to-end test of the data acquisition system, are ongoing and nearly complete.

The remaining components to be deployed are a single LF optics tube, the primary, and secondary mirrors. The LF optics tube will be completed by the end of 2024. The mirrors are scheduled to be delivered by early 2025. First light is expected in early 2025.

3.2 TolTEC

The TolTEC camera is a trichroic polarimeter installed on the 50-meter Large Millimeter Telescope (LMT) with photometric bands centered at 150, 220, and 280 GHz. TolTEC's angular resolution is 10, 6, and 5 arcsecond at 150, 220, and 280 GHz respectively and has a 4 arcminute FOV [52, 74]. This angular resolution is exceeded only by the ALMA interferometer at these frequencies, but the FOV is much larger meaning TolTEC is the only instrument in the world capable of imaging scales from 5 arcseconds up to several arcminutes at these frequencies.

TolTEC was installed as a facility instrument on the LMT in the Summer of 2022 with commissioning observations beginning in December 2022. Trouble with the LMT in 2023 meant that no commissioning observations occurred. The LMT came back on-sky in early 2024 and at that time TolTEC resumed commissioning observations. It is anticipated that commissioning will be completed by the end of 2024 and science observations can commence.

We will describe the aspects of the TolTEC instrument that enable groundbreaking cluster observations. We will describe the LMT site and its suitability for observations at millimeter wavelengths. We then describe the warm optics that TolTEC utilizes which includes the LMT warm optics. That leads to a description of the TolTEC cryostat and the cold optics it contains. We then describe the detector arrays and technology TolTEC uses to measure millimeter-wave light. Finally, we conclude with a summary of the status of the TolTEC instrument and remark on the timeline for science observations.

3.2.1 The LMT Site

The LMT is situated on Sierra Negra (known as Tliltépetl, Atlitzin, or Iztactepetl Icni in native mexican languages) in the Mexican province of Puebla. At an altitude of 4600 meters, it is one of the highest telescopes in the northern hemisphere. A photo of the LMT atop Sierra Negra is shown in figure 3.6. Construction of the telescope began in the late 1990s

Figure 3.6: A photo of the LMT site atop Sierra Negra. [75]

and was partially completed in 2010 with a primary mirror diameter of 32 meters. This initial configuration of the primary allowed the telescope to achieve first light in 2011. The remainder of the diameter of the primary was completed in 2018.

The LMT site is located in a somewhat tropical climate at a latitude of nearly 19 degrees North. Therefore the atmopshere is not as arid as the climate of the Atacama Desert. Moisture in the atmophere during the Summer months limits the quality of observations made at higher frequencies, meaning that optimal observing conditions are achieved mostly in the Winter and Spring.

We show the atmospheric transmission and brightness temperature in figure 3.7 [55]. The colored boxes in that figure denote the TolTEC bandpasses. There is a steep roll-off in the atmospheric transmission at roughly 100 GHz and consequently means that TolTEC's higher frequency bands can only really be used in ideal conditions. Comparing these atmospheric quantities to those of the Atacama depicted in figure 3.3 show the benefit of moving to a

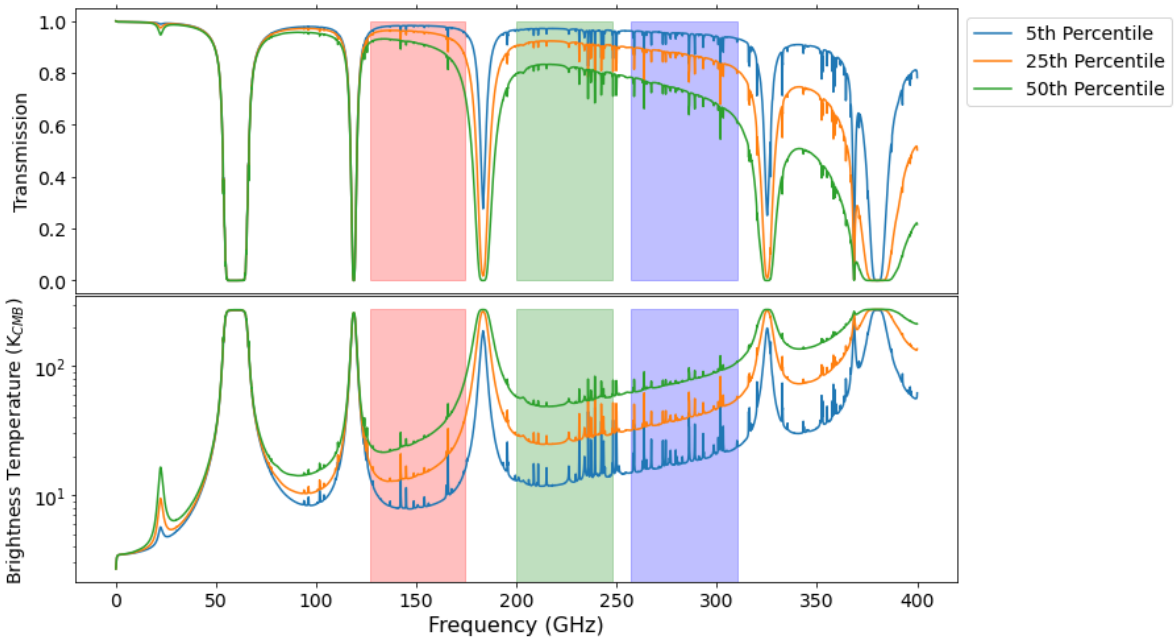

Figure 3.7: Plot of the atmospheric transmission (top) and brightness temperature (bottom) at the LMT site atop Sierra Negra. The TolTEC photometric bands are represented with the colored boxes. The percentiles refer to the amount of water vapor in the atmosphere.

higher-drier site. Despite this atmospheric limitation, the LMT site is still a more than adequate location for millimeter-wave astronomy as has been demonstrated by numerous instruments.

There is significant infrastructure built around the LMT which enable its scientific operations [75]. The telescope base camp is located in Ciudad Serdàn, roughly an hour drive away from the telescope. This close proximity allows observers to stay at the lower alititude (2600 meters) and make a nightly trip up to the telescope for observations. The road up Sierra Negra is paved and well maintained, making it one of the highest driveable roads in North America.

The LMT itself contains several lab spaces where instruments can be worked on before deployment. The LMT structure contains an elevator which makes working at altitude less stressful on the body and generally makes it possible to not require supplemental oxygen

while working at the telescope. These conditions permit nightly shifts for observers at the telescope. These in-person observations, as opposed to remote, are a valuable part of observing with the LMT, especially during instrument commissioning, as having trained observers at the telescope means that the instrument can be debugged in real time as observations are taking place.

The LMT site is not without its problems and several of these have contributed delays to the commissioning of TolTEC. Firstly, in early 2023 a wildfire at the base of Sierra Negra damaged the fiber optic cable that carries internet data to the telescope. This paused observations for many weeks until the cable could be repaired. Some observations did take place with data being transmitted via a Starlink satellite, however no major commissioning occurred during this time. Later in 2023, a severe lightning storm struck near the site. This caused an electrical surge which damaged transformers in the LMT electrical substation, rendering them inoperable. The repair of the transformers took many months and essentially meant that no TolTEC commissioning observations took place in 2023. These problems pertaining to and around the LMT site have since been rectified and the LMT resumed observations in 2024.

The LMT is one of the largest telescopes in the world and the site it is located has all of the infrastructure it needs to be a premier site for observations at millimeter wavelengths. The atmosphere is adequate for observations roughly 25% of the time although the increased atmospheric emission at the other times does not entirely prohibit observations.

3.2.2 Warm Optics

Light from the sky make their way through two ambient temperature optical systems in order to reach the TolTEC detectors, the LMT mirrors and the TolTEC warm optics system. The LMT's optics in order are the 50 meter diameter primary mirror, the 2 meter convex secondary, and a folding tertiary mirror inside of the receiver cabin. Once light reflects off

that folding mirror it is directed into the TolTEC warm optical system which consists of two parabolic and a flat mirror.

Details of the LMT optical system are given in Hughes et al. (2020) and we reproduce the pertinent facts about the warm optical system here [75]. The LMT is an on-axis Cassegrain reflector telescope. The primary and secondary mirrors are state-of-the-art and permit observations at 280 GHz without excessive scatter or aberrations. The surface of the 50-meter primary mirror is made of over one thousand aluminum panels with a surface RMS of 15 microns. Groups of six to eight panels are attached to actuators that allow for adjustments to be made to the panel's position. The actuators are electronically controlled so that the mirror surface can be refined at different elevations to counteract any sag in the mirror surface. The overall surface is set using photogrametry measurements during the daytime. Then during nighttime, observations of point sources are used to further tune the beam shape and antenna gain. This optimization procedure has been shown to reduce surface errors of the primary mirror to under 50 microns RMS.

The 2.7 meter diameter convex secondary mirror is also made of segmented aluminum panels. There is a central 1.2 meter diameter panel surrounded by eight other panels to make up the entire mirror. The secondary mirror assembly is mounted on a motorized hexapod so that it can be translated in three linear dimensions and also allows for the tilt of the mirror to be adjusted. The mirrors ability to move along the optical axis means that the focus of the telescope can be tuned by making brief observations of an unresolved source at several z positions and finding the position that maximizes the measured peak flux of the source. These observations can also be used for out-of-focus holography analyses which can be used to improve the understanding of the primary mirror surface. The entire secondary mirror system is suspended in front of the primary mirror by a tetrapod.

The last LMT optical element encountered by light before the TolTEC warm optics is the tertiary mirror. Located just before the Cassegrain focus, this tertiary mirror directs

light to one of the several instruments located in the LMT receiver cabin. The primary and secondary mirrors move to point the telescope but the instruments within the receiver cabin remain stationary, so the tertiary mirror is mounted on a system that tracks the primary and maintains alignment between that surface and instruments in the receiver cabin as the telescope slews in elevation.

Three mirrors make up the TolTEC warm optics which in order are a parabolic mirror, a flat, and another parabolic mirror [76]. These mirrors shape the beam from the telescope and direct them through the TolTEC window.

TolTEC also includes a warm halfwave plate (HWP) [77]. The HWP can be used to increase TolTEC's sensitivity to polarized light by modulating the polarization of the incident radiation by spinning the HWP at a fixed frequency and then measuring the modulated signal. Since TolTEC's cold optical elements are after the HWP in the optical path, any polarized signal they introduce is unmodulated and thus suppressed when demodulating the detector signal at the HWP frequency. This technique has successfully been used by other millimeter-wave observatories in the past to reduce the impact of instrumental polarization and mitigate atmospheric noise. Since the detection of the faint polarized signal from the SZ effect is beyond the scope of this work we will not discuss the HWP further.

3.2.3 Cold Optics

Light from the warm optics is incident on the UHMWPE window of the TolTEC cryostat. All the optical elements after that are kept at cryogenic temperatures. This includes silicon lenses, IR filters, dichroic beamspliters, and LPE filters [74]. The optics are mounted on a 2 meter by 1.5 meter optical bench that fits in a cryostat. Figure 3.8 shows this system with the outer shells of the cryostat removed. TolTEC uses beam spliters that pass certain frequencies and reflect others to direct signals defining its three bands to their respective detector arrays. The optical paths to the three detector arrays indicated in figure 3.8 by the

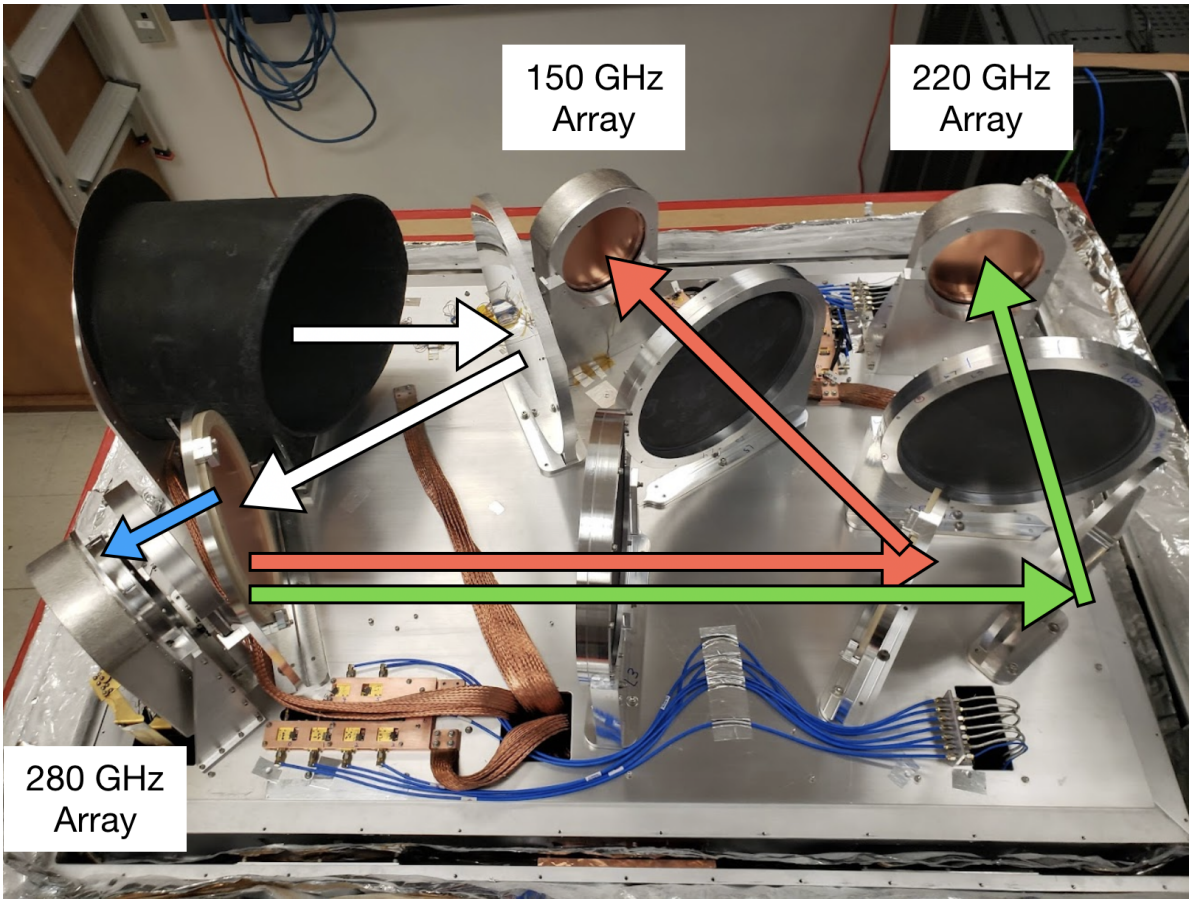

Figure 3.8: A picture of the TolTEC cold optical system with the cryostat shells removed. The different detector arrays are annotated and the paths of light from the different bands are denoted by the red, green, and blue arrows for the 150, 220, and 280 GHz arrays respectively.

red, green, and blue arrows for the 150, 220, and 280 GHz light respectively. The brief path that is shared by all light is indicated with the white arrows.

The optical path that is common for all light starts with the window and ends at the first dichroic beam splitter. After the incident light passes through the window it encounters an ambient temperature reflective IR filter to reject IR radiation. There is an additional IR filter located at 40 K and another at 4 K. Next to that filter is the cold Lyot stop. The light is then focused with an aluminum parabolic mirror and directed at the first dichroic filter.

This is where the paths of the different photometric bands diverge. The dichroic passes the 280 GHz radiation which is then focused by two silicon lenses, passes through a LPE

filter, and then is incident on the 280 GHz feedhorn array. The 150 and 220 GHz light is reflected by the dichroic, focused by another silicon lens, and incident on a second dichroic filter. This filter passes the 220 GHz light which is reflected by a flat mirror, focused by a silicon lens, filtered by a LPE, and then incident on the 220 GHz feedhorns. The 150 GHz light that is reflected by the second dichroic is focused by a silicon lens, filtered by a LPE filter, and imaged onto the 150 GHz feedhorns. All of the silicon lenses are coated with metamaterial anti-reflection coating methods described in chapter 4.

Since this optics bench is a large cavity where stray light can reflect off several surfaces and increase loading on the cryogenic stages, the lid of the 4 K cryogenic stage is blackened and a charcoal cloth is placed on the aluminum bench the optics are mounted on. This charcoal cloth is not shown in figure 3.8. Testing in lab with a thermometer suspended in the middle of the 4 K cavity by thermally insulating threads showed that the loading due to light reflected around the cavity was sufficiently low.

3.2.4 Detectors

TolTEC's three detector arrays are feedhorn-couple microwave kinetic inductance detectors (MKIDs). The three bandpasses cover 150, 220, and 280 GHz and are plotted in figure 2.1. Again, from that figure one can clearly see how the TolTEC bandpasses are ideal for measuring the SZ effect.

Feedhorns couple free space radiation onto the detectors in a controlled manner. The design of the TolTEC feedhorns is somewhat simpler than the SO feedhorn design since the TolTEC detectors are monochroic and do not have as wide bandwidth as the SO detectors. The TolTEC feedhorns are fabricated by stacking layers of thin silicon wafers, glueing those wafers together, and then gold plating them. Each silicon wafer has an array of closely packed holes, created by deep reactive ion etching. The diameter of the holes are varied for each layer so when stacked up and glued they become a splined feedhorn profile. They are

Figure 3.9: (Left Top) The TolTEC 150 GHz feedhorn array. (Left Bottom) The assembled TolTEC 280 GHz detector array. (Right) A microscope image of 280 GHz MKID detectors. (Image credit: NIST and the TolTEC collaboration.)

gold-plated to make the surface conductive. The TolTEC 150 GHz feedhorn array is shown in the top left of figure 3.9 and the different layers of the silicon wafers that are stacked to realize the entire array are visible. The advantage of a stacked-silicon feedhorn array is that it is cryomechanically matched to the detector wafer, meaning that there is no need to account for differential thermal contraction between the feedhorn array and the detector array. Therefore, alignment of the feedhorns and detectors can occur at room temperature and they will remain aligned as the arrays are cooled down to 100 mK.

At the output of the feedhorn waveguides are the MKID detectors [78,79]. The operating principle behind MKIDs is similar to the μ-mux readout system described in section 3.1.3. In the case of the TolTEC detectors there is no OMT, instead the light that is output by the feedhorns is incident directly on a TiN/Ti/TiN trilayer superconducting thin film that

makes up the inductor. This inductor is coupled to a capacitor that make up a quarter-wave resonant circuit. When photons are absorbed by the inductor, the energy from that photon is enough to break Cooper pairs in the superconductor which changes its quasiparticle density. This in turn changes the kinetic inductance of that superconductor which changes the resonant frequency of the circuit it is in with the the capacitor. The shift in resonant frequency is measured and that directly correlates with the energy of the incident photon.

A microscope image of a 280 GHz MKID array is shown on the right side of figure 3.9. The cross or plus shapes encompassed in a circle are the inductor probes that couple to the output of the feedhorns. Each leg is one detector. Since they are arranged at angles of 0, 45, 90, and 135 degrees that means the combination of the signals from those detectors give TolTEC its polarization sensitivity. The rectangular blocks to the left and right of the inductors are the interdigiated capacitors that complete the LC circuit of the detector. This LC circuit is capacitively coupled to the transmission line that is below the detector.

The detectors in the array are grouped into networks and each network is is read out with a single transmission line. Warm readout electronics send probe tones down the transmission line, these tones then encounter the MKID resonator circuits, and where there is a resonance there is no transmission of the probe tone. The detectors' signals are then interpreted by interrogating the transmission of the probe tones. Monitoring shifts in nulls of the transmission spectrum directly corresponds to the amount of power on a detector. Since many detectors are grouped onto a single transmission line, the readout is naturally multiplexed. TolTEC groups between 500 and 700 MKIDS on a single readout network. Although the multiplexing limit is theoretically higher for MKID detectors, the TolTEC multiplexing factor was chosen such that there is adequate frequency spacing between the resonators in the readout frequency sweep. That mitigates issues with collided resonator tones which can arise from variations in detector fabrications.

The TolTEC detectors combine the traditional feedhorn optical coupling with MKID

detector technology. Table 3.2 provides a summary of the angular resolution, detector count, and total array NET of each photometric array. The TolTEC detector sensitivities result in an instrument that is capable of imaging arcminute to degree scale fields to micro-Kelvin depths in a few hours of observing time. This makes it ideal to image galaxy clusters which manifest as $\sim$100 μK signal on $\sim$5 arcminute scales, so five hours of TolTEC observations should be more than sufficient to image a cluster.

Table 3.2: Summary of the TolTEC detectors based on the designed parameters.

	150 GHz	**220 GHz**	**280 GHz**
Angular Resolution (arcsecond)	10	6	5
Detector Count	1172	2532	4012
Array NET ($\mu K_{CMB}\sqrt{s}$)	18.9	39.3	70.5

3.2.5 Instrument Status

TolTEC achieved first light in 2022 with commissioning observations beginning in December of that year. The purpose of the commissioning campaign is to make observations that demonstrate the telescope is operating as close to its design sensitivity as possible. A subsample of the observations made during the December 2022 commissioning are presented later in section 6.2. The December 2022 commissioning campaign showed that TolTEC has an impressive angular resolution that will produce state-of-the-art images at millimeter wavelengths. It also showed that there are areas where the instrument needs to be improved to bring it more in-line with designed expectations.

An example for where TolTEC could be improved was in the quality of the instrument beams. In observations of pointing sources there were persistent aberrations in the beam profile. Misalignment between TolTEC and the LMT secondary is the likely cause, but additional investigation using out-of-focus holography is underway to confirm this. It is anticipated that this can be brought under control by adjusting the secondary mirror position and improving the primary mirror surface. Correcting this is expected to improve the

instrument gain by approximately 20%.

The noise of the instrument was significantly higher than what was achieved in the lab environment. It was determined that amplifiers in the readout chain where being overdriven which caused clipping and could explain the increased noise. To remedy this, attenuators were placed before the amplifiers to prevent overdriving and clipping in the readout chain. This improvement will make the TolTEC system photon noise limited for the next phase of commissioning.

TolTEC resumed commissioning observations in 2024. The initial improvements to the secondary position seem to have improved the beam shape but there are still improvements to be made with detector noise before commissioning finishes at the end of 2024. After that, science observations of the project's legacy surveys and PI-lead proposed projects will begin and will usher in a new generation of high-resolution millimeter wavelength images.

CHAPTER 4

METAMATERIAL ANTI-REFLECTION COATINGS

Instruments that observe at millimeter wavelengths, such as the Simons Observatory and TolTEC, rely on lenses with high indices of refraction to make compact optical systems. The usual materials of choice for these lenses are silicon and alumina with indices of refraction at millimeter wavelengths of approximately 3.4 and 3.1 [80]. While the high index of refraction for these two materials means that incident light can be refracted significantly to create a faster optical system with a wide field of view, it also means that more light is reflected off the bare optical surface. For silicon and alumina, roughly 30% and 26% of normally incident light would be reflected per optical surface in the absence of anti-reflection (AR) coatings.

Reflected light within an optical system leads to undesirable systematic effects. In extreme cases, multiple reflections occurring within an optical element can lead a coherent re-imaging of an object at a spurious location in an image which is often referred to as ghosting. More pervasive issues with reflected light is the reduction of the amount of transmitted power that reach the detectors, degraded image quality, and reduced polarization purity. Therefore, it is vital that reflections are reduced within optical systems.

This necessitates the use of AR coatings. One way that coatings can be realized is by adding materials with carefully selected dielectric properties and thicknesses to the surface of interest. In the simplest realization, a quarter-wavelength thick layer of material with dielectric index $\sqrt{n}$ can be added to the surface of a material with index n. This quarter wavelength coating can perfectly cancel reflections at a particular wavelength and provide acceptable performance over a moderate bandwidth. Broader band performance is possible with multiple layer coatings or by extending these to the continuum limit to realize a gradient index coating.

Complications arise when attempting to apply traditional AR coatings, like laminate plastics, to the surface of optical elements that operate at cryogenic temperatures. The

mismatch in the coefficent of thermal expansion between the laminate AR coating and the optic causes differential thermal contraction. This can lead to delamination of the coating from the optic surface. The problems that arise from a complete failure of the coating include ghosting and loss of efficiency, however partial delamination can lead to more subtle frequency-dependant optical effects which can be hard to track down and mitigate. AR coating delamination might not occur immediately, it may take several cryogenic cycles for issues to arise, so every time an instrument is warmed up and cooled back down there is the risk of coating failure. Over the lifetime of millimeter-wave receivers like SO and TolTEC those cryo cycles occur dozens of times. Thus, it is vital to develop and impliment AR coatings that do not suffer from differential thermal contraction to ensure the success of millimeter-wave instruments.

Metamaterial AR coatings offer a solution to differential thermal contraction. The coatings are made of sub-wavelength features machined into the optical element and so the coating is made out of the optical material itself. Metamaterial AR coatings are realized by creating a periodic array of features that are sufficiently smaller than the wavelength of the incident light. By tuning the geometries of those features, reflections can be minimized across a given bandwidth. The geometry and fabrication of the sub-wavelength features varies greatly depending on the application and the wavelength of the incident light. Raut et al (2011) gives a general review of designs and fabrication techniques used to create AR coatings [81]

The design, fabrication process, and performance of diced metamaterial AR coatings for the silicon lenses and alumina IR blocking filters for SO are described in this chapter.

4.1 Design and Fabrication of Silicon Metamaterial Anti-Reflection Coatings for the Simons Observatory

We present the work done to realize metamaterial AR coatings for lenses in the three SO observing bands and at the necessary production scale for an experiment the size of SO. The work for the TolTEC metamaterial AR coatings was similar, but the coatings were simpler due to the narrower required bandwidth. This section is organized as follows: the design of the AR coatings for all three SO observing bands is presented in Section 4.1.1. Section 4.1.2 describes the production process of the AR coatings and presents the achieved production rates. In Section 4.1.3 the results of reflection measurements taken of the AR coatings are presented.

4.1.1 Design

The design of the sub-wavelength features follows the geometry presented in Datta et al (2013) [64]. The features consist of metamaterial layers that are an array of square "stepped-pyramids". This design was chosen because these features are easily fabricated with a silicon dicing saw, where the saw makes a series of nested cuts across an optic, the optic is then rotated 90 degrees, and the series of cuts are made again. Figure 4.1 shows a fiducial model of a three-layer metamaterial AR coating. In principle, the number of layers can be increased to accommodate large bandwidth coverage, but this is subject to physical constraints such as dicing blade thickness and aspect ratio. Metamaterial coatings with five-layers have been demonstrated and show excellent performance over more than an octave bandwidth [82]. The pitch, or the spacing between the periodic cuts, each layer's width (kerf), and depth must be optimized to minimize the reflections across the observing bands.

The SO will observe in three dichroic frequency bands; the low frequency (LF), mid frequency (MF), and ultra-high frequency (UHF). The band edges for those three channels

observe from 23-47 GHz, 70-170 GHz, and 195-310 GHz for the respective LF, MF, and UHF bands. We begin the optimization process by modeling the physical AR coating structure in the finite-element analysis software, Ansys High Frequency Structure Simulator (HFSS)[1]. We began the optimization process with the three-layer 75-170 GHz metamaterial AR coating presented in Coughlin et al (2018).

The pitch of the sub-wavelength features is set by the criterion for scattering which is given by Equation 1 in Datta et al (2013) [64]

$$p < \frac{\lambda}{n_{\mathrm{si}} + n_{\mathrm{i}} \sin\theta_i} \tag{4.1}$$

Where p is the pitch, λ is the wavelength corresponding to the upper edge of the frequency band, n_{si} and n_{i} are the indices of refraction of silicon and the incident medium (in this case vacuum) respectively, and θ_i is the angle of incidence of light on the surface of the lens. We choose the pitch such that this criterion is met up to the upper edge of the observing frequency band at an angle of 15 degrees which is roughly the average angle of incidence of a light ray in the telescopes.

We then optimize the AR coating design for the free parameters, the kerf and depth, per each metamaterial layer. For a three layer coating there are six parameters to optimize and for a two layer coating there are four. An optimization algorithm in HFSS is used to vary these parameters to achieve the lowest reflection possible across the SO MF band. Since the size of the sub-wavelength features dictate what frequencies the coating is effective, the dimensions of the parameters of the AR coating can be scaled up or down to cover the LF and UHF bands. However, that scaling may not produce an optimized AR coatings in that new frequency band or the resulting design may not be physically realizable with dicing saw blades.

1. https://www.ansys.com/products/electronics/ansys-hfss

For the SO LF band, the MF AR coating design parameters were scaled up and then re-optimized. The resulting coating achieved sub-percent reflection across the LF band. Finally, the MF AR coating was scaled down to try and cover the UHF band, but kerf of the third layer became thinner than any physically producible dicing saw blade. This drove the design of the UHF coating from a three-layer design to a two-layer design. After optimizing the two-layer UHF design we still achieved a simulated sub-percent reflection across the band due to the UHF's more narrow fractional bandpass.

After the completed optimization we then have three AR coating designs that all achieve sub-percent reflection across their respective frequency bands. The dimensions of the three optimized AR coatings for the LF, MF, and UHF bands are presented in Table 4.1. The parameters refer to figure 4.1. Note that the UHF design is a two-layer and therefore the dimensions of the third layer are non-applicable. The simulated performance of the AR coatings at normal incidence are presented later in Section 4.1.3.

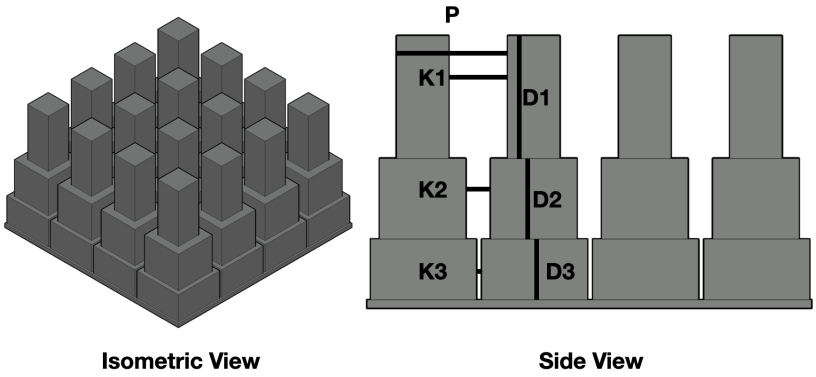

Figure 4.1: (Left) Isometric view of a fiducial three-layer AR coating design. (Right) Side view of the fiducial three-layer design with the relevant design parameters labeled.

4.1.2 Production

The SO will deploy over 30 silicon lenses which is the most by any single experiment to date and therefore the production rate of the metamaterial AR coatings for those lenses must be

Table 4.1: Parameters of the three SO silicon AR coating designs

	LF	MF	UHF
Pitch (P)	1.375 mm	0.450 mm	0.266 mm
Kerf 1 (K1)	0.735 mm	0.245 mm	0.122 mm
Depth 1 (D1)	1.520 mm	0.425 mm	0.200 mm
Kerf 2 (K2)	0.310 mm	0.110 mm	0.033 mm
Depth 2 (D2)	1.000 mm	0.294 mm	0.120 mm
Kerf 3 (K3)	0.070 mm	0.025 mm	-
Depth 3 (D3)	0.750 mm	0.234 mm	-

high enough to follow the deployment timeline. This combined with the added complications that we need to dice the largest diameter silicon lenses deployed on an experiment to date and the complex surface profiles of some of the lenses [83] lead to the development of a custom silicon dicing saw system.

The metamaterial AR coatings were fabricated using a custom-built multi-axis dicing saw system. This system (shown in figure 4.2) consists of three dicing saw spindles mounted on independent z-axes (100 mm of travel) on a common y-axis (±600mm of travel). A ruby-tipped metrology probe with sub-micron accuracy is mounted on the forth z-axis. This probe is used to map the surface of the mounted optics to be cut. The optics to be machined are secured on a chuck mounted on a rotary stage with 360° rotation on top of an x-axis (±275mm of travel). These axes allow the complete fabrication of an AR coating on one side of an up to 600 mm diameter optic without need to dismount the optic. There are numerous features that allows for significant increases in production rate compared to previous efforts to produce metamaterial AR coatings for CMB experiments such as the multiple dicing spindles which can each be fit with a different blade corresponding to different cuts in the AR coating's design. By mounting all of the blades at once we can AR coat an entire optical surface without changing any blades. This provides for nearly continuous operation of the saw system. Careful commissioning and calibration of this dicing saw system lead to micron accurate stage positioning and repeatability which is well within the tolerances required for AR coating application presented here.

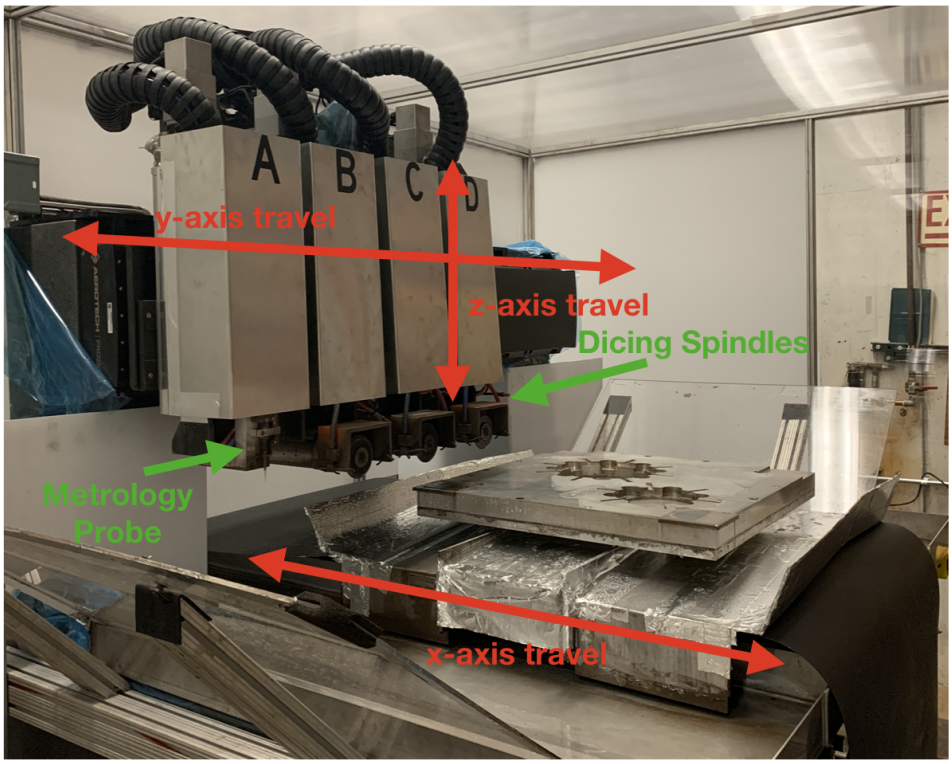

Figure 4.2: An image of the dicing saw system used to fabricate metamaterial ARCs. The independent dicing spindles are labeled B, C, and D with the metrology axis labeled A.

To create an AR coating, a lens is mounted to the dicing saw and metrology is taken of its surface using a sub-micron accurate metrology probe mounted to the system. A model surface is fit to that data, and code generates program files that are used to command the system to dice the cuts. The room that the dicing saw is situated in is temperature regulated and the dicing process uses temperature controlled flood cooling. This temperature regulation is necessary to ensure the fabrication machine does not thermally expand or contract during the cutting process. The design-specific blades are then mounted to the spindles, and are conditioned to eliminate diamond burs on the blade and to ensure the blade is circular by making several cuts in a special ceramic material made to hone dicing saw blades. Test cuts are then diced into a small silicon wafer affixed to the side of the mounted lens. These cuts are then inspected and their dimensions verified with a microscope.

The layers of the AR coating are diced into the lens, one at a time, from the largest to the smallest cut. After the layers are diced into the lens, it is then rotated 90 degrees and the process is repeated to complete the AR coating. After the AR coating is finished, test cuts are made in the sacrificial wafer to monitor if any cutting abnormalities may have arisen during the fabrication. After one optical surface of a lens is finished it is flipped and the procedure repeated on the other side. After both sides of a lens have been AR coated, the lens is cleaned in an ultrasonic cleaning bath.

That is the process for the MF and the UHF coatings but for longer wavelengths where the feature size is much larger we must modify this approach. Dicing blades are not available in widths to make the top two layers of the LF coating. For those layers, we use three defining cuts and two clearing cuts to create a feature that is much wider than the maximum blade thickness. In order to not load the dicing blades with too much cutting force we make multiple passes of defining and clearing cuts to realize the full depth of the top two LF layers.

Figure 4.3 shows an image of one of the MF lenses installed inside an SO optics tube. It also shows a zoomed in picture of the fabricated coating. At the end of the fabrication run for the MF lenses we achieved a production rate of one lens per week. The defect rate was around 100 broken pyramid features out of a million which is not expected to impact the lens quality or the AR coating performance.

4.1.3 Optical Performance

The lenses were tested and the optical performance measured using a coherent reflectometer. The reflectometer setup is described in detail in Chesmore et al.(2018) [84]. The lenses are mounted like in figure 1 of the Chesmore paper with the flat side down toward the parabolic mirrors. In cases where the lens does not have a flat side, we measure the concave side as close to the center of the lens as possible where it is the most flat. The results of the

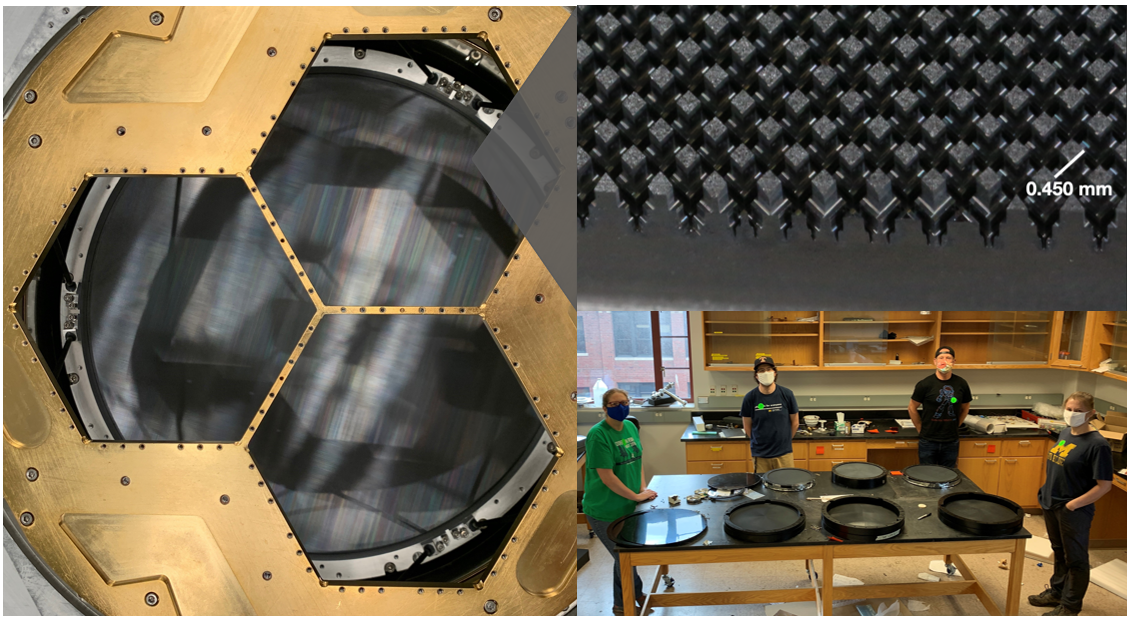

Figure 4.3: (Left) Picture of a SO LAT lens installed in an optics tube. (Right Top) A zoomed in image of the MF metamaterial AR coating. (Right Bottom) A Picture of the production team with six SO lenses. The three closest to the camera are a set of SO Small Aperture Telescope lenses and the three farther away are a set of SO Large Aperture Telescope lenses.

reflection measurements for the SO MF and UHF AR coatings are summarized in figure 4.4. The presented data for the LF AR coating is from lenses made for the AdvACTPol experiment which share the same design and fabrication procedure as the SO lenses. This data shows good agreement with simulations with sub-percent reflections across the LF bands. The performance of all of the measured coatings so far have achieved sub-percent reflection across their bands.

4.2 Broadband Metamaterial Anti-Reflection Cuttings for Large Aperture Alumina Optics

Alumina is a ceramic material that can be machined into large diameter optics for millimeter wave bands and its use as an IR rejecting filter is critical to the function of next-generation

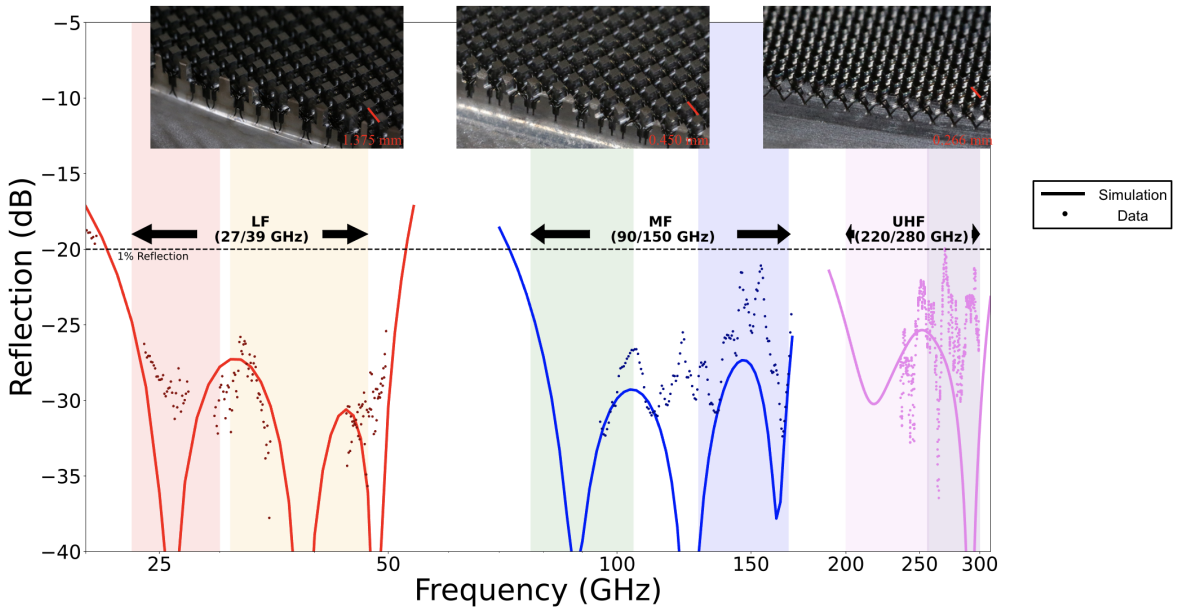

Figure 4.4: Plot of the reflection performance of the SO AR coatings. The solid line represent the simulated performance of the AR coating and the dots represent measurements.

instruments. For the optics considered here, we sourced our low-dielectric loss type alumina from NTK Ceratek in Japan[2]. High-purity (>99.%) sintered alumina exhibits low dielectric absorption at millimeter wavelengths, but has relatively high dielectric losses in the sub-millimeter [85–87]. This property, combined with strong restrahlen bands at infrared wavelengths, makes alumina an ideal filter material by effectively rejecting infrared radiation by scattering it out of the optical path or absorbing and efficiently thermally conducting it to a cryogenic system without significant heating. However, alumina's high index of refraction ($n = \sqrt{\epsilon_r} = 3.14$) is approximately constant in the microwave [61, 80, 88, 89] and causes 26% of incident light to be reflected per surface in the absence of AR coatings. We focus on two-layer metamaterial cuttings that function as an homogeneous two-layer coating which can achieve percent-level control of reflectance over an octave of bandwidth when applied to alumina.

2. `https://www.ceratech.co.jp/en/product/material/alumina/a9951ld/`

Enormous efforts have gone into developing multi-layer AR coatings for alumina. This includes laminated plastics [90], laminated epoxy [88, 91–93], laminates of commercial materials [94], and laser machined metamaterial cuttings [92, 95, 96]. The laminates require identifying materials with the required indices of refraction, controlling changes in the thickness and index throughout the lamination process, and control of cryomechanical delamination. The latter poses a critical risk for applications which require a high reliability. The recent results on laser machining shows promise as they have demonstrated coatings on deployed optics though it has yet to control reflections at the percent-level across an octave of bandwidth.

We present a new approach whereby we use dicing saw blades to cut metamaterial structures, comprised of sub-wavelength stepped pyramids, into the alumina surface. This approach is based on previous work on silicon metamaterial AR coatings [64, 65, 82] which are now deployed on AdvACTPol [21], CLASS [97, 98], TolTEC [52], and the Simons Observatory [51], but it is necessary to expand this technology to alumina substrates as well to take advantage of the IR rejecting material properties inherent in alumina that are not present in silicon. We demonstrate this technique on the alumina filters for SO.

The organization of this section is as follows: Section 4.2.1 contains a brief description of the designs of the AR coatings for two dichroic observing bands centered at 90/150 GHz (the Mid-Frequency bands or MF) and 220/280 GHz (the Ultra High-Frequency bands or UHF). The fabrication procedure of the alumina coatings with the dicing saw is described in section 4.2.2 and meteorology of the machined coatings follow in section 4.2.3. We present measurements of the reflection and transmission of the MF and UHF AR coatings in section 4.2.4, along with the description of the apparatus used to make those measurements.

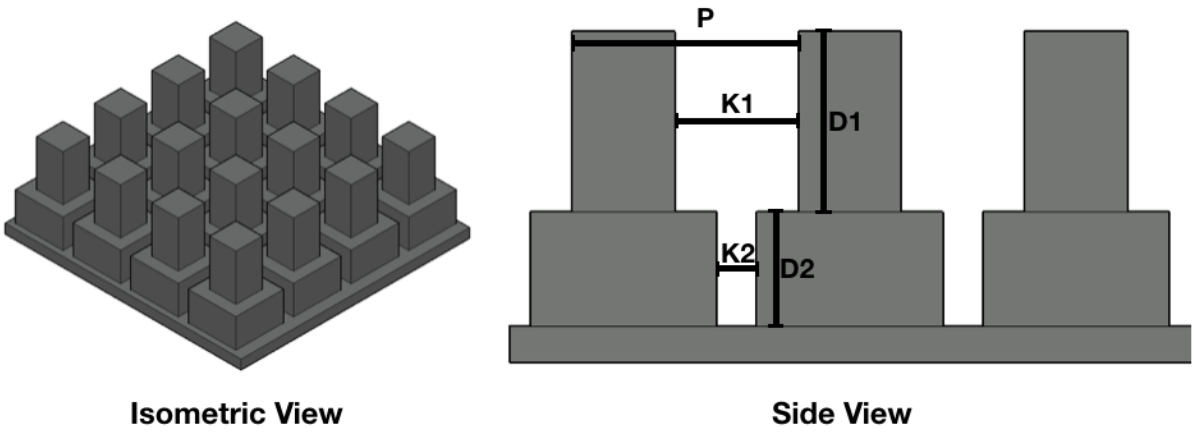

Figure 4.5: (Left) Isometric view of a fiducial two-layer ARC design. (Right) Side view of the fiducial two-layer design with the relevant design parameters labeled.

4.2.1 Design

We adopt the same geometry and design process for the alumina AR coatings as for the silicon metamaterial AR coatings described in 4.1.1. The main differences between the alumina AR coating designs and the silicon designs is that all of the alumina coatings are a two layer design shown in figure 4.5.

The UHF design was numerically optimized for the 200-300 GHz band. In this case, the simple scaling of the AR coating design was not possible due to blade limitations with regards to the thinner of the nested cuts. To overcome this issue, the kerf of the thinner cut (K2) was fixed to the smallest achievable kerf in alumina, 50 microns, and the optimization process adjusted the remaining three free parameters. In both the MF and UHF cases the optimal designs result in percent-level control of reflections across the bands which satisfies the design requirements for SO.

The initial optimal designs were prototyped and the measured profile of the cuts revealed that the dicing blade tool wear resulted in rounded rather than flat bottoms as shown in figure 4.6. This rounded geometry was incorporated into the HFSS simulation and the designs

were re-optimized. The resulting final design parameters for the MF and UHF coatings are summarized in table 4.2.

Table 4.2: Parameters of the two alumina AR coating designs

	MF	UHF
Pitch (P)	0.522 mm	0.295 mm
Kerf 1 (K1)	0.220 mm	0.160 mm
Depth 1 (D1)	0.425 mm	0.250 mm
Kerf 2 (K2)	0.070 mm	0.050 mm
Depth 2 (D2)	0.289 mm	0.138 mm

After the optimal designs were chosen, the tolerance of the performance to errors in cut depth was analyzed. The dicing blade thicknesses are controlled to a three micron tolerance which has little to no effect on the performance. Depth errors dominate the tolerance budget of the machining process. The AR coatings were simulated at normal incidence with combinations of depth errors of ±20 microns in steps of 10 microns for each effective layer. The results of this analysis, along with the nominal coating performance, are shown in figure 4.7. Note that the simulations were performed on a single-sided AR coating model and so the results represent the reflection per surface. All simulations that deviate from the nominal design are below 2% reflection in the observing bands which is the design goal for SO and so we fix 20 microns as the requirement for depth control for the fabrication of the coatings.

4.2.2 Fabrication

The dicing saw used to fabricate the AR coatings is described in secion 4.1.2. The dicing procedure for the alumina AR coating is similar to the process used for silicon presented in section 4.1.2, but because alumina is considerably harder than silicon extra steps must be taken to ensure the cuts maintain the correct depth. The procedure starts with mounting an alumina filter and using the metrology probe to map its surface. These data are fit to a flat plane model with Fourier corrections to account for deformations due to how the filter is clamped. The residuals of this fitting procedure are normally less than five microns. The

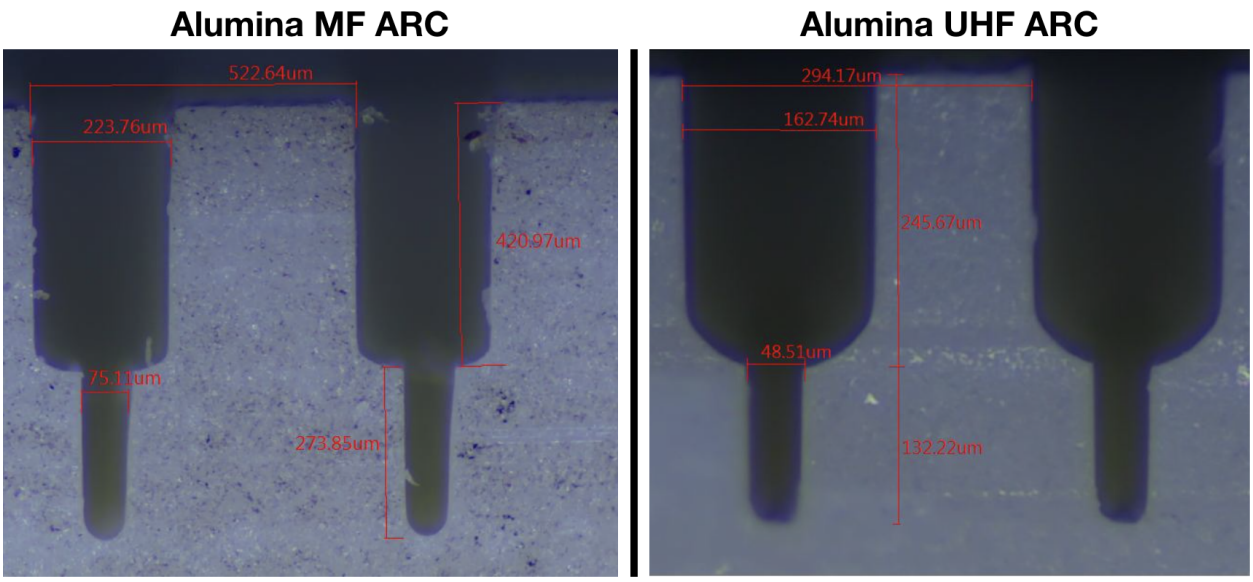

Figure 4.6: (Left) Microscope image of the alumina MF metamaterial AR coating prototype. (Right) Microscope image of the alumina UHF AR coating prototype.

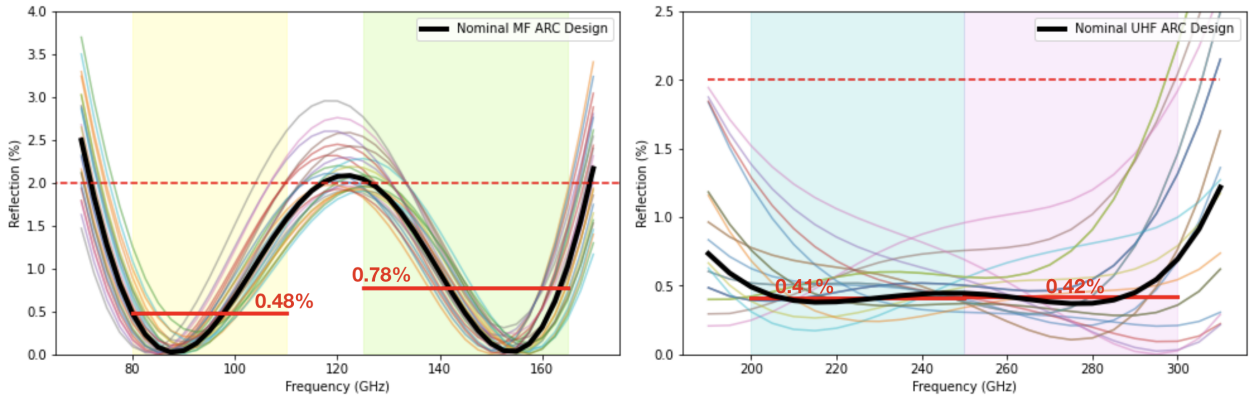

Figure 4.7: (Left) Results of the MF tolerancing analysis. (Right) Results of the UHF tolerancing analysis. The semi-transparent curves denote variations from the nominal designed depths of the cuts. The solid red lines denote the average reflection across the bands and the red dotted lines denotes 2% reflection.

cut trajectories are then generated for each dicing spindle. To confirm the absolute depth of the cuts, test touches are then performed with the dicing saw blades on the filter surface. These serve two purposes: the first is to confirm that the fit to the metrology data and the model is accurate; the second is to correct for any z-offset between the model surface and the actual filter which can arise from slight differences in the blade diameters.

A set of test touches are additionally performed on a test silicon wafer mounted to the same aluminum chuck as the alumina filter, which serves as a relative reference for blade wear. After every 25 lines are diced on the filter, the system automatically makes a test touch on the silicon wafer. The test touches are chosen to be approximately 50 microns deep. The length of the test touch represents a chord across the 78 mm diameter circle defined by our round blades. Measurement of this chord allows a micron accurate determination of the depth of the cuts. This measurement is used to determine the blade wear (diameter loss) as a function of millimeters of alumina diced.

Controlling for tool wear of the dicing blades is the critical development needed to realize these coatings. Different blades are used to realize the two different kerfs in both the MF and UHF coatings. These blades differ not only in thickness, but also in how the zinc composite material they are made of is bonded and blade exposure which leads to multiple blade wear coefficients to track. Moreover, the blade wear also depends on which orientation of the coating is being diced. Since the second set of cuts (rotated 90° relative to the first set) dices through previously diced material, the blades need to remove roughly half the alumina and thus have a lower blade wear. For reference, for the MF AR coating we have found that the most the blades wear on average is 6 microns per meter of alumina diced for the thick blade and 20 microns per meter for the thin blade. One 42 cm diameter MF filter requires roughly 260 meters of total length diced. With the maximum blade exposure without compromising cut quality, the dicing process requires roughly two thick and 12 thin blades to completely fabricate a filter. To streamline the fabrication process, we mount one of the thick blades on one spindle and thin blades on the remaining two spindles. This allows for longer cutting periods without blade changes. Every time the blade is changed the test touches on the silicon reference wafer calibrate the depth the new blades are cutting and allow new wear coefficients to be inferred.

Using the procedures outlined in this section, four full-scale SO Large Aperture Telescope

(LAT) MF filters were fabricated as well as a two-inch diameter UHF prototype. The ultimate production rate that was achieved for the MF filters (one of which is shown in figure 4.8) was 15 days per 42 cm diameter filter. We believe that a higher rate can be achieved if the inspection of the test touches on the silicon reference wafer is automated. If a microscope is added to the system this test touch process could be done remotely or automated completely. This would allow for nearly continuous operation of the saw system and could cut the production rate to less than a week per filter.

4.2.3 Metrology

Throughout the development of the AR coatings, measurements of the coating need to be made to confirm that the cuts are being diced to specification. We use several techniques to make these measurements including microscopy and photography.

Microscopy was performed on the smaller prototypes since the larger filters do not fit in the available microscope. The microscope is also used during the fabrication process to inspect cuts diced into a test silicon wafer to ensure the dicing blades are not excessively worn such that the profile is compromised. Images taken with the microscope of the MF and UHF AR coatings are shown in figure 4.6 and one can clearly see that the profile is similar to the fiducial stepped pyramid design but with rounded bottoms due to the tool wear. The microscope images also confirm that the kerf of the cuts are to specification. The difference between the measured depths and the nominal values are within the 20 micron machining tolerance which confirms that the machining procedure outlined in the previous section is successful at achieving the design specifications for the ARCs.

We use a 5:1 macro lens on a digital camera to verify that there are no large scale variations in the ARCs and to inspect any defects that may appear. The resulting images from the camera serve as the quality assurance step in the fabrication procedure of the filters. The photos shown on the right side of figure 4.8 confirm that there is essentially no chipping

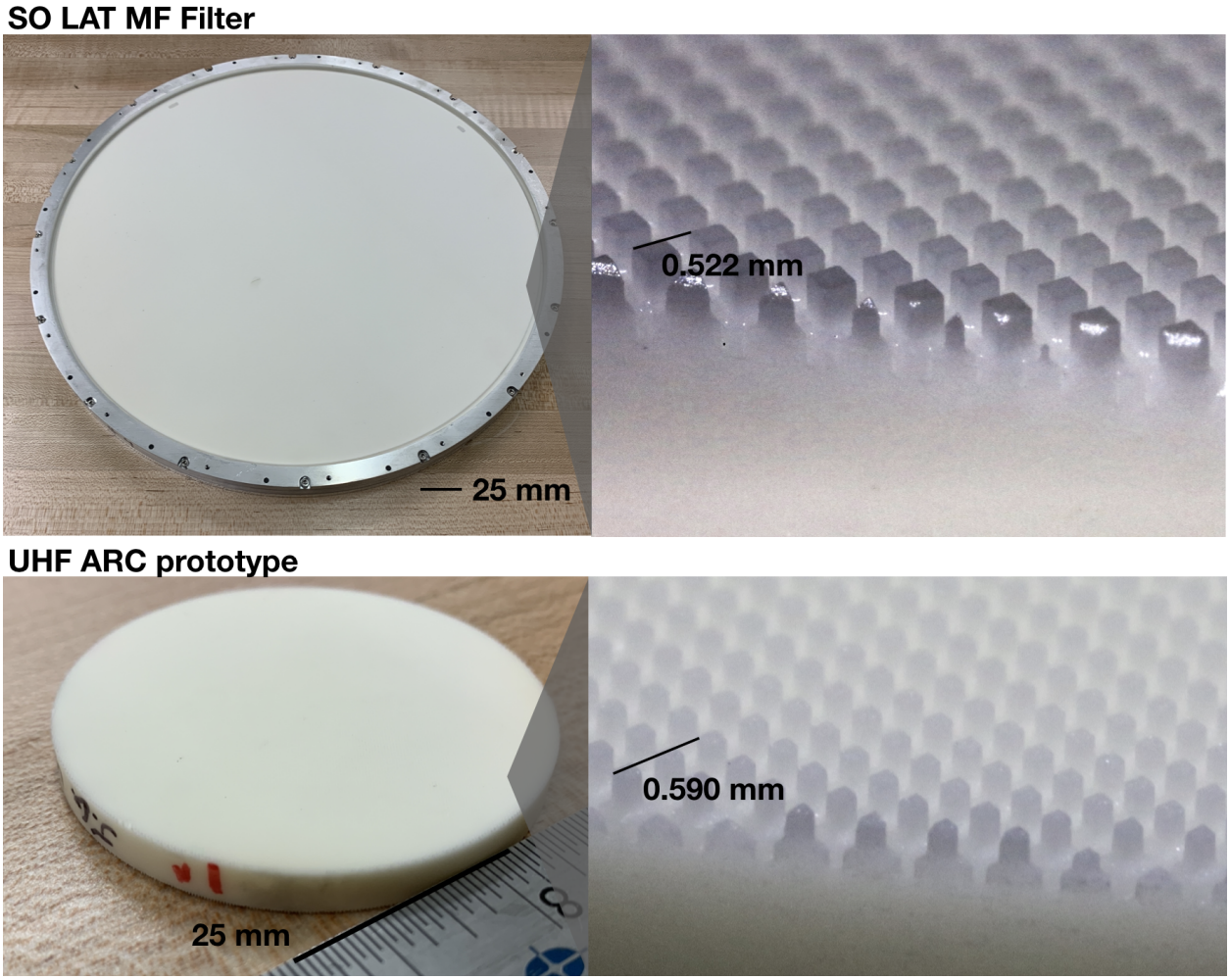

Figure 4.8: (Top Left) Full sized image of an AR coated SO LAT MF filter. (Top Right) A zoomed in picture of the MF AR coating. (Bottom Left) Full sized image of the UHF prototype. (Bottom Right) A zoomed in picture of the UHF AR coating.

or other defects that can be associated with the dicing procedure. Additionally, no defects appeared after thermally cycling the filter between room temperature and 80 Kelvin which is the operating temperature of these filters in the SO LAT cyrostat. Due to the robustness of alumina, the defect rate is extremely low with less than a dozen broken sub-wavelength pillars across the filter which contains over 500,000 pillars in total.

4.2.4 Reflection and Transmission

The reflection and transmission of the AR coated filters and prototypes were measured using an ultra-broadband (20-1200 GHz) source and detector coupled to the sample using parabolic mirrors. The measurements presented here are made at ambient room temperature. The operating temperatures of the alumina filters in the SO optical systems are 80 K and below. While the index of refraction will not change appreciably from room temperature to those temperatures, the dielectric losses will decrease by as much as a factor of four [88]. This will not to affect the reflection performance presented here, but it will result in improved in-band transmission. The cryogenic dielectric loss was accounted for in the design of the IR blocking filters [59].

The ultra-broadband coherent source used to measure reflection and transmission uses two distributed feedback (DFB) lasers with indium gallium arsenide transmitter and receiver photomixers purchased from Toptica Photonics[3]. The two DFB diode lasers send near-infrared frequencies to the emitter photomixer. The difference frequency from these two tuned lasers dictates the terahertz frequency generated in the photomixer. These two diode lasers are temperature controlled automatically by the accompanying digital controller. The emitter photomixer, i.e. the transmitter, outputs a beam with a divergence angle ranging from 12 to 15 degrees from a 25 mm diameter silicon lens encasing.

The transmitter (also referred to as the source) generates a continuous wave (cw) terahertz frequency signal. This photomixer is a metal-semiconductor-metal structure with interdigitated electrodes and a bow-tie antenna. The electrodes produce a photocurrent which oscillates at the difference frequency. This photocurrent is then output as our desired terahertz signal by the log-spiral antenna surrounding the photomixer.

The receiver photomixer, also encased in a silicon lens, is illuminated by both the terahertz wave and the laser beat. The photocurrent induced in the receiver photomixer is

3. `https://www.toptica.com/products/terahertz-systems/frequency-domain/terascan`

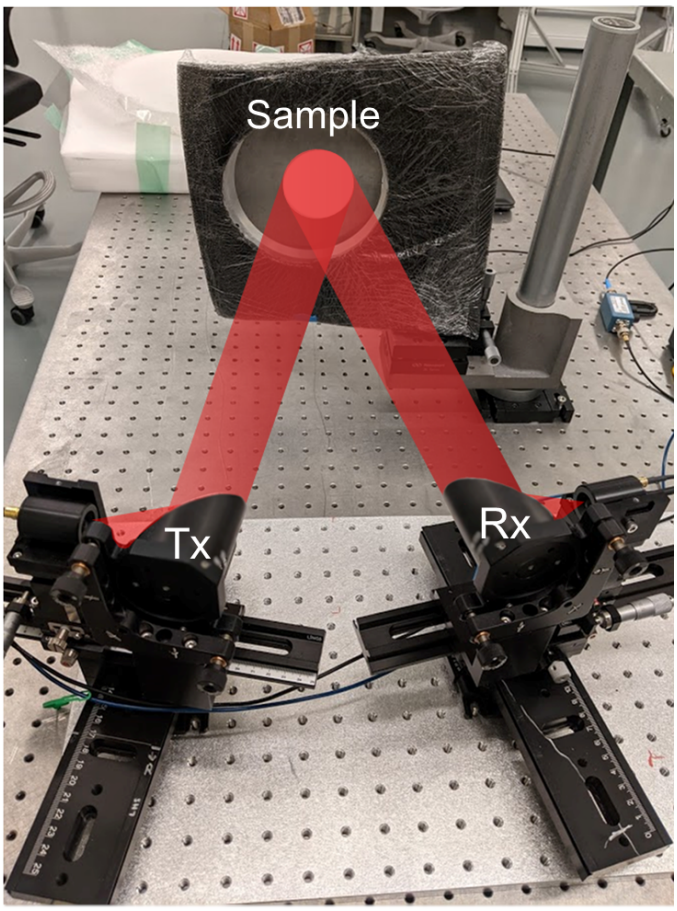

Figure 4.9: The setup for the reflection measurement. The polished plate is pictured here in the sample holder. (Tx is the transmitter, Rx is the receiver.)

proportional to the amplitude of the signal's electric field.

A fiber stretcher extension, which adjusts the optical path length difference between the transmitter and receiver, is used to modulate the phase at kHz frequencies. The output of the receiver is then demodulated to get the amplitude and phase of the electric field. The minimum frequency resolution is 1 MHz when using the fiber stretcher and the source can sweep from 20-1200 GHz in 0.2 GHz steps in approximately thirteen minutes.

Figure 4.9 shows the setup for measuring reflection. Reflection measurements were made by mounting the sample on an adjustable mount that precisely aligns the sample to couple optimally between the source and receiver. The mount is made of aluminum and covered in an Eccosorb HR-10 layer to mitigate unwanted reflections. The setup of the system can

support standing waves which reflect through the full optical path between the transmitter and receiver. These are reduced by two carbon-loaded polyethylene flat sheets, typically 0.5 mm thick (not pictured in figure 4.9), placed in the optical path just following the transmitter and receiver to work as attenuators. These plates are oriented at 45° relative to the beam propagation direction so that reflected light exits the system.

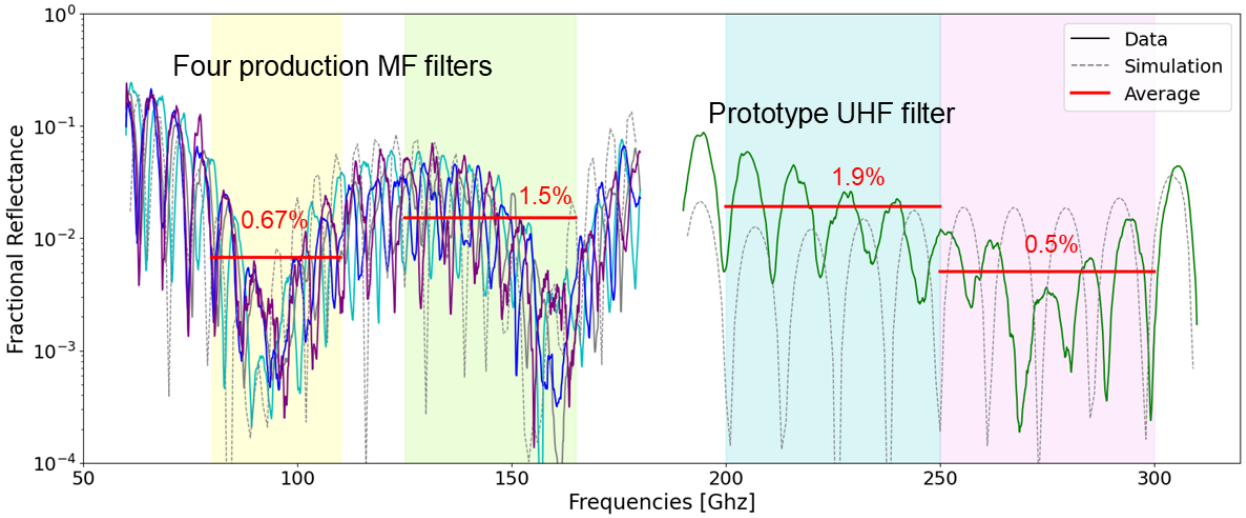

Figure 4.10: Measured reflection of ARC of four 450 mm diameter MF filters and one 50 mm diameter prototype UHF filter. The red lines indicate the average reflection across the observing bands. The reflection measurements were made by Shreya Sutariya.

Calibration is done by measuring the reflected signal from a polished aluminum plate. The reflection from the sample is then measured with the surface of the AR coating placed in the same optical plane as the aluminum plate. The ratio of the measurement and calibration are squared to find the fractional reflected power. The reflection was measured from 60-180 GHz for the MF alumina filters, and from 190-330 GHz for the UHF filter. The step size was set to 0.1 GHz with an integration time of 3.02 ms per frequency bin. The wedged MF filters are roughly 8 mm thick (the thickness varies between 5 and 11 mm) and the UHF filter prototype is 5 mm thick, so the 0.1 GHz frequency spacing of the reflection measurements is adequate to resolve fringing within the samples which should be on the order of several GHz. The measurements were carried out at an angle of incidence of 14 degrees for the first

MF filter and at 10 degrees for the other three MF and the UHF filters.

The reflection measurements of four SO MF LAT filters and the prototype UHF filter are shown in figure 4.10. The four MF filters all have mean reflections less than 2% in the observing bands which meets the SO design requirements for the alumina filters. Due to the wedge design of the filters, the reflection performance between all four filters are not identical since they were measured at different locations on the filter with varying thicknesses. However, all the filters produced are in line with HFSS simulations of the ARC.

The UHF prototype also has a mean reflection less than 2% across the UHF bands but performs slightly worse than predicted by the design HFSS simulation. Measurements of the coating dimensions with a microscope revealed that the cuts were too deep by as much as 20 microns at points which caused poor performance in the lower frequency band. This error was confirmed post-fabrication by investigating the variability of the test touches made on the silicon reference wafer during fabrication. Even with this error, the prototype achieves less than 2% reflectance across this band. We anticipate improved UHF ARC performance when these filters enter production for SO since better active care will be taken to control the cut depths during fabrication.

The transmission was measured with the beam from the source aligned to point directly to the parabolic mirror pairing it to the receiver. Calibration was performed by dividing the power received with the samples in place by the power received when the transmitter-to-receiver path is unblocked. These measurements were carried out from 50 GHz to 1.2 THz in 0.1 GHz steps. The results are shown in figure 4.11 (see [61] for the transmission spectra of alumina without an AR coating).

The results for the MF and UHF coatings place a lower limit on in-band transmission at $> 80\%$. The ability to assess transmission in-band are limited by the control of alignment and standing waves in the system which are not perfectly controlled. Given the reflectance measurements, and separate measurements of the loss-tangent of alumina [88], we interpreted

this as consistent with 97% transmission in-band.

Both the MF and UHF coatings show a dramatic decrease in transmission above their respective bands. This apparent attenuation is more than an order of magnitude larger than what is expected from the loss tangent of the alumina material. This was confirmed by measuring the transmission of an uncoated alumina plate which showed no such attenuation at high frequency. We interpret this above band attenuation as the onset of scattering in these coatings which is anticipated as the wavelength of the incident light becomes comparable to the pitch of the AR coating. In this wavelength regime, the AR coating grating no longer satisfies the "quasi-static limit" condition where only the zeroth-order diffraction mode propagates and instead multi-mode propagation occurs [99–102]. While a rigorous theoretical model that encompasses this behavior is beyond the scope of this paper, we can test our interpretation by scaling the frequency axis relative to the metamaterial breakdown frequency, or the frequency where the coating grating enters the diffractive or multi-mode limit. This is given by [102]

$$f_0 = \frac{c}{P(n_{\text{alumina}} + n_{\text{vacuum}} \sin\theta_i)} \tag{4.2}$$

where P is the pitch of the coating previously defined in section 4.2.1, n_{alumina} and n_{vacuum} are the optical indices of alumina and vacuum respectively, θ_i is the angle of incidence, and c is the speed of light. The scattering threshold frequency as stated here is dependant on the pitch dimensions and therefore is a scale dependant property of the coating. For the two filter designs presented in this work the diffractive limit threshold frequencies are $f_{0,\,\text{MF}} = 184$ GHz and $f_{0,\,\text{UHF}} = 326$ GHz, for the MF and UHF filters respectively. We plot the transmission after scaling, $f_{\text{scaled}} = f/f_0$, in the right panel of figure 4.11. The qualitative agreement of these two measurements supports our interpretation with a change in transmission by approximately -10 dB per octave after entering the diffractive limit.

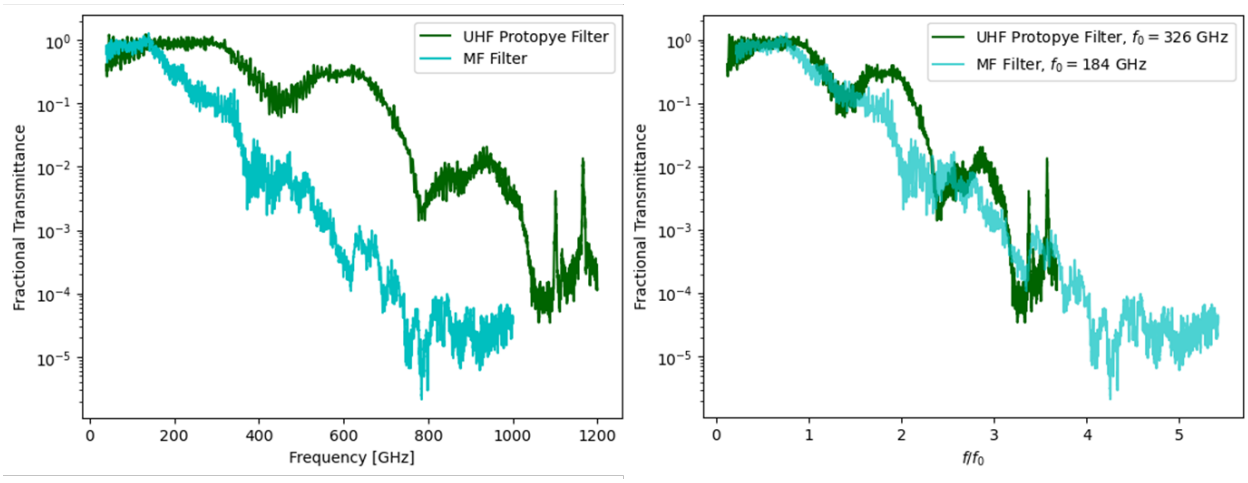

Figure 4.11: Transmission of the UHF AR coated alumina prototype and a MF AR coated alumina production filter. (Left) The fractional fractional transmittance of the filters as a function of frequency. (Right) The transmittance as a function of scaled frequency where the frequencies are divided by f_0, the diffractive limit threshold frequency of the filter. This is done to highlight the transmission falling off at similar rates in both filters.

4.3 Conclusion

We presented metamaterial AR coatings for silicon lenses in the SO LF, MF, and UHF bands and coatings for alumina filters in the SO MF and UHF bands. Similar coatings were fabricated for the silicon lenses for the TolTEC experiment. The silicon AR coatings achieve sub-percent control of reflections across up to an octave of bandwidth and the alumina coatings achieve percent-level control averaged across the observing bands. That performance satisfies SO's requirements for reflections per optic which brings that aspect of the instrument inline with achieving its performance goals.

The production rate of the silicon AR coatings was around four days per lens and the alumina AR coating production rate was around 15 days per filter. That is sufficiently fast so that optics could be manufactured, tested, and integrated into instruments within the SO deployment schedule. This is remarkable for a project at the scale of SO which includes dozens of optics.

The AR coated optics have been integrated into the SO LAT optics tubes and the TolTEC

camera. The performance of a MF SO LAT optics tube has been measured in-lab. Near-field beam maps and radio holography measurements show that all of the lenses and filters are performing as designed and do not contribute any measurable systematic effect to the optics [103, 104]. On-sky beammaps made with TolTEC also show that the cold optics are not the dominate source of systematics within that optical system, and there is no sign of ghosting or other undesirable optical effects that would be associated with faulty AR coatings.

The reliability of the metamaterial AR coatings for silicon and alumina optics makes it a compelling technology for future millimeter and sub-millimeter experiments. The robustness of the coatings to thermal cycling, their state-of-the-art performance, and the proven record across many experiments make them the standard for AR coatings for high-index millimeter-wave optics.

CHAPTER 5

MAXIMUM-LIKELIHOOD MAPMAKING

Images from millimeter-wave telescopes are made in a different way than an ordinary camera. Telescopes scan across the sky and record detector response as a function of time. Through calibration procedures, the detector response is then converted to a flux. The goal of mapmaking is to take this detector response that is a function of time and turn it into an image of an astronomical source. There is a large scientific effort to make optimal procedures to create images, or maps, from time-ordered data (TODs).

Two methods to methods to create maps from TODs are filter-and-bin mapmakers and maximum-likelihood mapmakers. Filter-and-bin mapmakers are relatively straightforward to implement. TODs are filtered in timestream-space and frequency-space to mitigate atmospheric and instrumental noise. Then those filtered timestreams are binned into a pixelated representation of the sky. The filtering can be as simple as a combination of low-pass and high-pass filters, or as complex as removing the largest eigenvalues from the timestreams in a principle component analysis. The upside to this method is that filtering and binning are simple computationally and can make high-quality maps quickly. The downside is that the filtering introduces biases in the final maps that can reduce recovered flux on the larger angular scales. Filtering out the atmosphere or other sources of $\frac{1}{f}$-like noise also reduces the signal flux that may appear at scales similar to the atmosphere.

Maximum-likelihood mapmaking is an alternative method to make images with data that does not rely on filtering to remove noise. Instead, a combination of the pointing matrix and an estimation of the noise covariance are combined with the data to produce an unbiased realization of the sky. Since no filtering is required in maximum-likelihood mapmaking, larger angular scales can be reconstructed from the data so signal more signal on larger angular scales can be recovered compared to filter-and-bin mapmakers. The lack of filtering produces an unbiased image of the sky which is important for imaging signals

from extended astrophysical objects. However, this comes at a cost of computation time. Maximum-likelihood mapmaking usually requires manipulations of extremely large matrices and other time consuming algorithms. However, these are tractable and the timescales for producing a map do not become so large as to be infeasible. The time trade-off is permissible given the more optimal reconstruction of the sky.

In this chapter we present the maximum-likelihood mapmaking pipeline developed for the TolTEC collaboration and maps made from early commissioning data. We begin with an introduction to maximum-likelihood mapmaking and then move onto how it is implemented by TolTEC. We conclude with presenting a comparison between the performance of TolTEC's maximum-likelihood mapmaker and its filter-and-bin mapmaker.

5.1 Introduction to Maximum-likelihood Mapmkaing

Maximum-likelihood mapmaking solves a single linear equation called the mapmaking equation. To understand that equation, we begin with a model of telescope timestreams.

Data from a millimeter-wave telescope like TolTEC can be modeled as the true sky signal acted on by an observation's pointing matrix plus noise. Mathematically this can be represented as

$$d = Pm + n \tag{5.1}$$

where the true sky is m, the pointing matrix is P, the noise is n, and the data is d. Note that m, n, and d are all vectors in the above equation and P is a matrix. If we assume that the noise is Gaussian and can be described by a covariance matrix defined as $N = \langle nn^T \rangle$ then we can use a standard Gaussian likelihood for m given our data d which is given by

$$\mathcal{L}(m) = (2\pi N)^{-\frac{1}{2}} \exp\Big[-\frac{1}{2}(d-Pm)^T N^{-1}(d-Pm)\Big] \tag{5.2}$$

Since our goal is to find the solution m that maximizes this likelihood (i.e. we differentiate this expression and then find m that make it the differentiated expression zero), we can consider the log-likelihood. Since log is a monotonically increasing function, extremal solutions must be maxima. The log-likelihood is proportional to

$$\log \mathcal{L}(m) \propto (d-Pm)^T N^{-1}(d-Pm) \tag{5.3}$$

Differentiating this and setting this equal to zero gives

$$P^T N^{-1} d = P^T N^{-1} P m \tag{5.4}$$

Which means the most likely sky m given the data d is

$$m = (P^T N^{-1} P)^{-1} P^T N^{-1} d \tag{5.5}$$

This relatively simple expression means that if an observation is made, the pointing information is known, and the noise covariance of that observation is known, an optimal representation of the true sky can be reconstructed by simply evaluating the above equation. However, there are several complications to that ideal world.

The first complication is the $(P^T N^{-1} P)^{-1}$ term on the right hand side. For an experiment like TolTEC which has an order of 1000 detectors in each frequency band and a

small map containing tens of millions of pixels, that term becomes impractical to invert. We instead approximate the solution iteratively by solving equation 5.4.

The second complication comes from the noise covariance matrix N. This is not known *a priori* and must be estimated from the data itself.

5.2 Maximum-likelihood Mapmaking for TolTEC

In this section we outline the process to make maximum-likelihood maps with TolTEC data. We will take particular care to explain how we are estimating the noise covariance from the timestreams and will detail the iterative mapmaking approach to recover flux from bright extended sources.

Data from the observation are first analyzed using TolTEC's filter-and-bin mapmaker that is a part of the standard data reduction pipeline, `citlali`. The maximum-likelihood mapmaking pipeline for TolTEC is built on the `minkasi` mapmaker that was developed for the MUSTANG-2 collaboration [32, 49][1].

The process for making TolTEC maps with `minkasi` is as follows: raw timestreams with only a flux calibration and a correction for atmospheric extinction applied are output from the `citlali` data reduction pipeline, those timestreams are then fed into the `minkasi` mapmaker. In `minkasi`, a second order polynomial is fit to approximately 15 minutes of data or the entire observation if it is shorter than 15 minutes. The fitted polynomial is removed from the timestreams to generally account for detector drifts. Then the noise covariance matrix is estimated.

There are two important aspects that are necessary to represent when estimating a noise covariance matrix, the correlated noise between the detectors that are due to sources like the detector readout, and the correlated noise that varies with time such as the atmosphere. To estimate the noise we use the default function in `minkasi`. This function take the

1. `https://github.com/sievers/minkasi`

timestreams, which are a matrix that is $n_{\text{detectors}}$ by n_{samples} and performs a singular value decomposition (SVD) on that matrix, rotates the timestreams into the detector eigenspace defined by that SVD, and computes the power spectrum of the rotated timestreams. This is a complex and important process so it is worthwhile go over those steps in more detail.

A SVD is a generalization of an eigenvalue decomposition for a rectangular matrix. It takes any rectangular matrix as an input and represents it as two square matrices and a rectangular-diagonal matrix. For matrices with real elements which is the case for the timestream matrix, this can be represented as

$$T = USV^T \tag{5.6}$$

where T is the $n_{\text{detectors}}$ by n_{samples} timestream matrix, U is a $n_{\text{detectors}}$ by $n_{\text{detectors}}$ unitary matrix, S is a $n_{\text{detectors}}$ by n_{samples} rectangular diagonal matrix, and V^T is a n_{samples} by n_{samples} unitary matrix. If T was a square matrix this reduces to a usual eigenvalue decomposition where U becomes a matrix of the eigenvectors, S a diagonal matrix of the eigenvalues, and $V^T = U^T$. However in this general case one can think of the U matrix as the principle vectors that span the detector space and so define the most important modes common to all detectors. Therefore to capture the important correlations between detectors we can take the T matrix and perform a rotation via the U matrix so we have

$$T' = UT \tag{5.7}$$

The rotated individual timestreams (i.e. the individual rows of T') then capture the principle correlations between the detectors ranked by from the largest to smallest eigenvalue.

Now we have to capture the time varying correlated noise between the detectors which is

mostly $\frac{1}{f}$ noise from the atmosphere and detector readout. To do this, we Fourier transform the rows of the T' matrix and then multiply that by its complex conjugate to get a matrix of one dimensional power spectra,

$$N_i = \mathcal{F}(T'_i)\mathcal{F}(T'_i)^* \tag{5.8}$$

This matrix N is how we define the noise covariance. We use the subscript i above to denote that we are defining the ith row of the N matrix. We then define the weights in this rotated space as $1/N$ where we are taking the element by element inverse and are not finding the inverse matrix.

Now anytime we want to perform the operation on the right hand side of equation 5.4 all we need to do is rotate timestream matrix into singular space as define by equation 5.7, take the Fourier transform of that rotated matrix, multiply it by the weights defined by $1/N$, inverse Fourier transform back into the time domain, and then perform the inverse rotation of equation 5.7.

This model of the noise is adequate for our application. The SVD involves computations on a vary large matrix and for long observations it becomes necessary to chunk the data into smaller timestreams, estimate the noise of those smaller timestreams, and then put them back together during the mapmaking step. As long as those chunks are sufficiently long to encompass the $\frac{1}{f}$ noise this will not degrade the estimation of the noise and so we generally make our chunks of order five minutes long which represents many scans across the observed field.

With the noise covariance estimated we determine the weights for the detectors. This is done by summing the inverse of the noise power spectra calculated above, making a diagonal matrix with the diagonal entries equal to the summed power spectra, and then rotating that diagonal matrix back into the original timestream space. With these weights in hand we

observe that some detectors have erroneously high weights. This is generally due to those detectors having low variance compared to the other detectors. This can be because they never scanned over a source or because they are not active and only sense readout noise. While those detectors are generally cut on the `citlali` side of this pipeline, some do make it through and we cut them here based on the weights. Detectors with weights that are six standard deviations above the median are then identified and cut from the remaining analysis, and then the noise covariance is saved for the first mapmaking iteration.

The mapmaking procedure proceeds by making a pointing matrix for the observation, calculating the hits map, and the weights map. `minkasi` then proceeds to the preconditioned conjugate gradient (PCG) algorithm to solve the maximum-likelihood mapmaker equation. To improve convergence of the PCG algorithm, we chose a preconditioner map that is the inverse of the hits map. This preconditioner generally helps with small scale converge of the map.

After the PCG solves the mapmaking equation the first time, the output map is re-projected into timestream-space and differenced from the data. This results in residual timestreams that more closely resemble noise. We then use these residual timestreams to re-estimate the noise covariance matrix and then repeat the mapmaking procedure from the proceeding paragraph. This iterative mapmaking approach is essential for observations of high signal-to-noise sources like the Crab Nebula since a single iteration of maximum-likelihood mapmaking underestimates the source flux. This is due to a weighting imbalance between detectors on and off the source. Detectors on the source will have a higher variance than those off the source which erroneously causes them to be downweighted. By iterating the noise estimation, we get rid of this issue of lower flux and find that 50 mapmaking iterations is sufficient to reach a plateau of flux recovered. We run an additional 20 mapmaking iterations for a total of 70 as a conservative choice.

5.3 Comparing Maximum-likelihood Maps to Filter-and-Bin Maps

We use simulations to see how images of extended low signal-to-noise objects differ between the `minkasi` maximum-likelihood mapmaker and TolTEC's naive filter-and-bin. We simulated five hours of observations with TolTEC of a simulated cluster with realistic tSZ and kSZ signals. The simulations are described in more detail in section 7.2.2. For this comparison of the two mapmakers it is important to note that the simulations contain realistic atmospheric noise.

For the naive filter-and-bin mapmaker, which uses PCA cleaning to remove atmospheric noise, we had to cut 10 eigenvalues in the PCA cleaning to get a map that was free of large scale noise. We also used 100 iterations of iterative mapmaking to improve the recovered flux at large scales. This is similar to the iterative mapmaking approach described for the maximum-likelihood mapmaking procedure, but instead of trying to better estimate the noise covariance this method is attempting to add back in extended flux that was removed as part of the PCA cleaning. A low signal-to-noise threshold for adding signal back in was used since the signal from the simulated cluster is weak.

For the maximum-likelihood images of the cluster we used the procedure outlined in the previous section. Since five hours of observations is too much to read into the mapmaker at once, we took the individual 30 minute observations of the simulated cluster and broke them up into 15 minute chunks. This length is sufficient to capture the large scale noise in the noise covariance estimation. We only used one iteration of mapmaking since we found that more iterations did not improve the recovered signal or reduce the large scale noise.

We show the simulated 150 GHz maps of the cluster in figure 5.1. The extended emission of the cluster is better recovered in the maximum-likelihood map compared to the filter-and-bin mapmaker, however the noise outside of the cluster signal is more uniform in the filter-and-bin map. Both of these aspects can be explained by the PCA cleaning algorithm that the filter-and-bin mapmaker uses. It biases the recovered signals to be on scales that are not

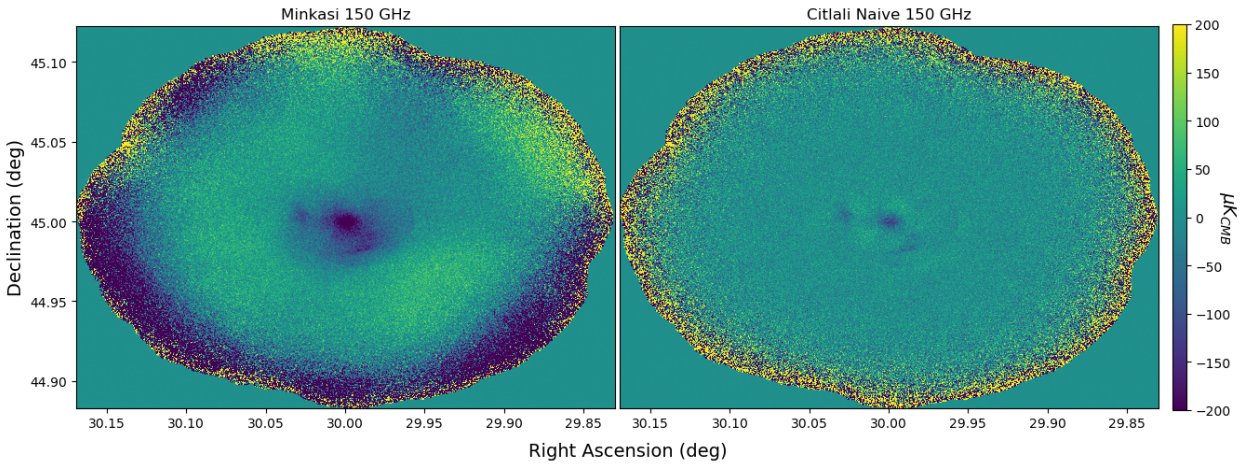

Figure 5.1: (Left) A maximum-likelihood map of a simulated cluster at 150 GHz. (Right) A map of the same cluster at the same frequency made with a naive filter-and-bin mapmaker.

correlated between groups of detectors which adequately removes atmospheric emission while sacrificing extended emission from the cluster. The maximum-likelihood map's unbiased reconstruction of the sky allows more signal from extended low signal-to-noise objects to be recovered.

CHAPTER 6

EARLY RESULTS FROM TOLTEC COMMISSIONING

The TolTEC instrument achieved first light on the LMT in June 2022. Commissioning observations took place in December of that year. In total, around 10 nights were spent observing extended and unresolved sources. However due to weather, improper observing scripts, and issues with the detectors, only around two nights had satisfactory observing. During those two nights, TolTEC observed the Crab Nebula and the Moncerous R2 molecular cloud (MonR2). Those objects are bright at millimeter wavelengths and are excellent objects to commission TolTEC and demonstrate the instruments capabilities. We focus on the early maps of the Crab Nebula. The Crab Nebula (also known as M1, Taurus A, or NGC 1952) is a supernova remnant that has been well studied across the electromagnetic spectrum [105–107]. Its bright emission at millimeter wavelengths makes it an ideal target to use for instrument commissioning. However interest in millimeter-wave observations of the Crab Nebula go beyond its bright emission, it is of particular interest to the millimeter-wave community as the polarized synchrotron emission from electrons in the pulsar's magnetic field are particularly bright. This makes the Crab Nebula a valuable astrophysical polarization calibrator, with applications in CMB experiments seeking to detect a faint polarization signal in the relic radiation, which could indicate the presence of gravitational waves, a signature of cosmic inflation [108].

We present the preliminary results from TolTEC commissioning observations of the Crab Nebula in this chapter. All of the maps presented were made using the `minkasi` maximum-likelihood mapmaker. First we show images of the pointing observation taken directly before the Crab Nebula observations. We introduce a model of the instrument's point spread function, or beam, derived from that pointing observation. We then present images of the Crab Nebula in three frequencies both in intensity and polarization. Finally, we conclude with measurements of the integrated flux derived from the TolTEC intensity maps and

several images of the polarization properties of the Crab Nebula.

6.1 Pointing Observations and Beam Model

Before a science target is observed, TolTEC's observing procedures require a brief 60 second observation of a bright unresolved radio source. This source is usually selected from the SMA catalog of bright radio sources [1] or from the ALMA Calibrator list [2]. It is chosen such that it is roughly in the same area of the sky as the science target. This observation serves several purposes among which are to make sure the telescope is properly in focus, to measure any telescope pointing offset, and to confirm that the detector flux calibration is reasonable.

During observations, quick maps of the pointing source are made with `citlali` which can produce maps in seconds. The quick maps are consulted to see if the instrument beam looks reasonable. If the beam looks unsatisfactory, for example if the FWHM of the 280 GHz beam is larger than its fiducial 5 arcseconds, then a focusing procedure takes place. That procedure consists of making a series of quick 20 second observations of the same bright source with the secondary mirror offset by various values along the optical axis. The flux of the sources is quickly measured in those maps, fit to a function of the secondary mirror position, and the position of the secondary where the point source flux is maximal is declared "in focus." If moving the secondary does not achieve a quality beam, then the surface of the primary mirror can also be adjusted. This process is referred to as "tuning the dish." Similar to the optimization of the secondary position, several 20 second observations of the bright source are made with the primary mirror distorted according to the Y-Tilt Zernike polynomial. The distortion where the measured point source flux is maximal is considered the optimal shape of the primary mirror. If the primary mirror's shape is changed, then secondary focus procedure is usually repeated. These procedures together result in a satisfactory instrument

1. `http://sma1.sma.hawaii.edu/callist/callist.html`

2. `https://almascience.eso.org/sc/`

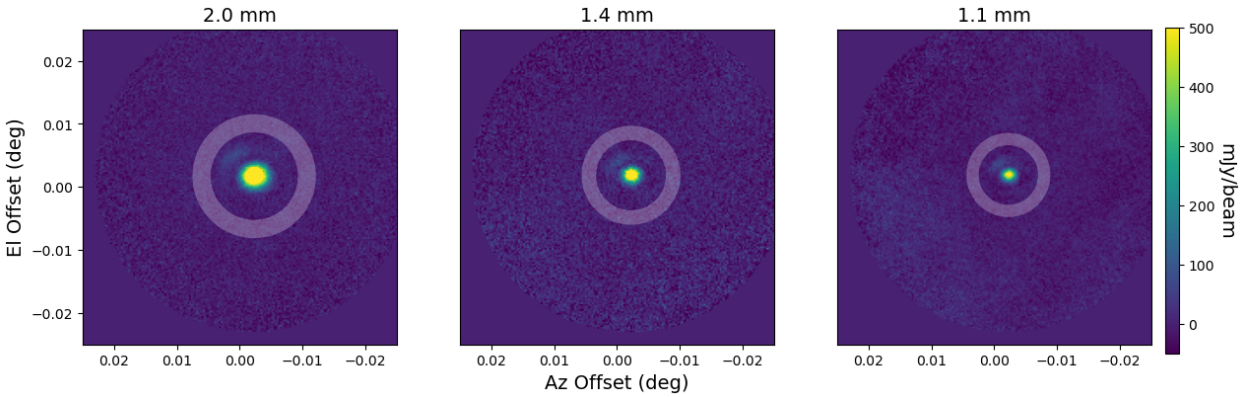

Figure 6.1: Maximum-likelihood maps of the pointing observation of 0510+180. The white annuli represent the region used for background subtraction in aperture photometry.

beam. Once the instrument is focused following the above procedures, a final 60 second observation of the pointing sources is taken. From this final images is where any pointing offset is derived for the science target observations.

For the Crab Nebula observations on the night of December 16, 2022, the pointing source 0510+180 was used. This source (also known as QSO B0507+179) is a radio bright quasar that is identified in numerous surveys. Importantly, it is included in both the SMA Submillimeter Calibrator List and the ALMA Calibrator Source Catalog. In fact, ALMA also observed this target on the same night [109].

Cropped 3 arcmin by 3 arcmin images of the TolTEC observation of 0510+180 at 150, 220, and 280 GHz (2.0, 1.4, and 1.1 mm) are shown in figure 6.1. The beams for the three frequency bands are approximately Gaussian, however there is a somewhat significant aberration located to the North-East of the main beam. This type of aberration is expected as the focus procedure outlined above is imperfect and improving it is an ongoing goal for the TolTEC team.

The first task for analyzing this observation is to measure the flux of the source. We do this by performing aperture photometry which is as follows: for each image we define a circular aperture that encompasses the main Gaussian source and the aberrations around it. We also define an annular aperture that has an inner radius equal to the radius of the

circular aperture and an outer radius that is the inner radius times the square root of two so that the annulus has the same area as the circular aperture. We then sum up all of the pixels in the circular and annular apertures. Since there is no emission from the source inside the annulus, we use that as an estimate of the background and subtract its sum from the circular aperture to get the total flux from the source.

The annular apertures used to estimate the background of the pointing source maps are shown in white in figure 6.1. The circular aperture is not shown, but is the area within the inner radius of the shown annuli.

We find that the statistical uncertainty from this measurement, calculated as the RMS flux within the annular aperture, to be a fraction of a percent of the source flux. However, the systematic uncertainty is much larger than that. This was determined by comparing the measured flux of all the TolTEC pointing sources from the commissioning data to known values from the SMA and ALMA. The scatter of these measured fluxes was around 10% so we adopt this value as the uncertainty in our estimation of the flux of 0510+180. This systematic uncertainty is as large as it is because during TolTEC's commissioning campaign it was forced to calibrate the instrument gain off of a radio galaxy. A thermal source, such as a planet or asteroid, would have been a better calibrator, but none were available during the nights TolTEC was observing.

The measured fluxes are plotted, along with the fluxes measured by ALMA on the same night, in figure 6.2. A power law was fit to the ALMA measurements so that a comparison could be made at TolTEC's frequencies and that is shown as the black dotted line. The agreement between the ALMA fit and the TolTEC data is remarkable, although unsurprising considering the large uncertainty in the TolTEC measurement.

We now turn to modeling the TolTEC beam from the pointing observations. Since the observed aberration is a known deviation from a simple Gaussian beam model, a more sophisticated model of the TolTEC beam is required for two reasons. The first is that beam

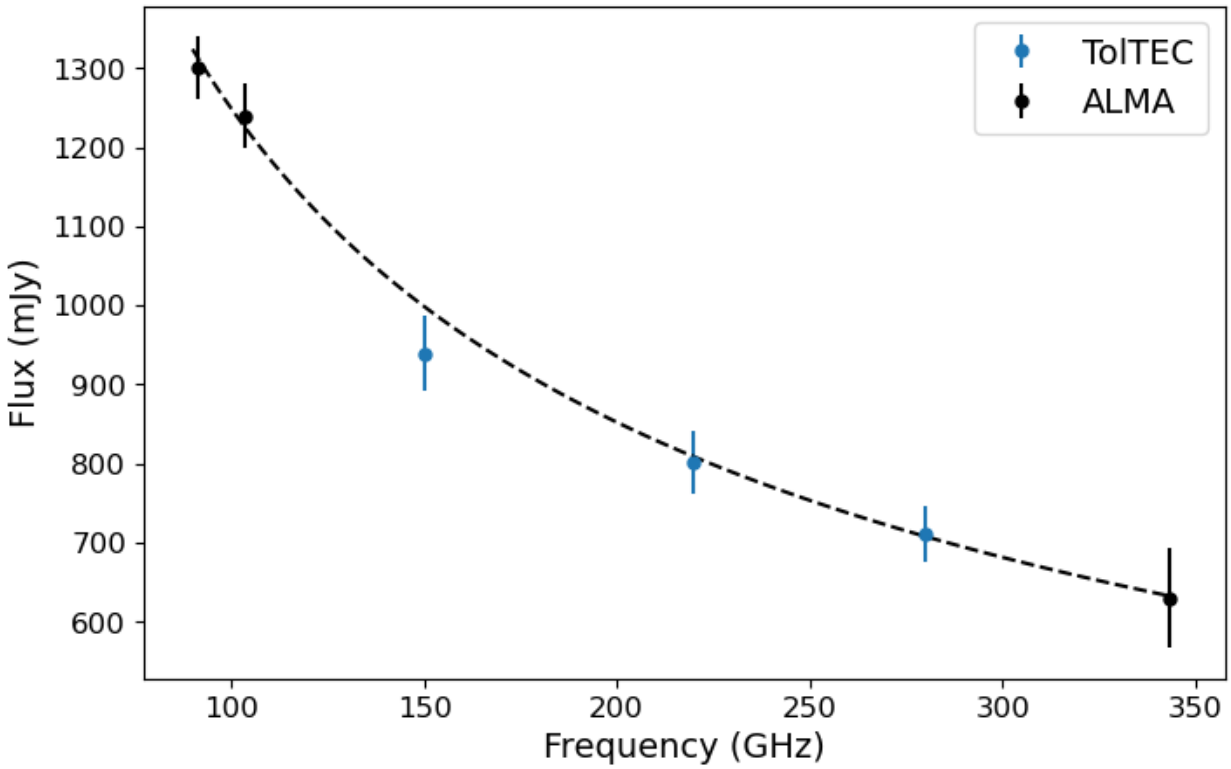

Figure 6.2: Measurements of the flux of 0510+180 made by TolTEC and ALMA on the night of December 16, 2022. The black dashed line represents the best fit to a power-law by the ALMA data.

models are needed for more sophisticated analyses of images that will be performed in the future, such as combining low-resolution millimeter wave images with the high-resolution TolTEC images which requires deconvolutions. Second, by building a model of the beam and measuring how much power is outside of the main beam we can understand what sort of improvements in instrument sensitivity we can make by improving the focus and primary mirror surface.

Our straightforward approach to model the TolTEC beam is to make an image of the telescope aperture, add phase errors at the aperture plane, and then apply the Fraunhofer diffraction equation to make an image of the instrument beam in the far-field. The telescope aperture is 50 meters in diameter with a 2.5 meter diameter occlusion in the center due to the secondary mirror. The legs that support the secondary also provide some occlusion

however the resolution of our model in the aperture plane is not fine enough to resolve the legs of the quadripod. TolTEC illuminates the LMT's primary with a Gaussian that has -3 dB of power at a radius of 24 meters. The instrument's Lyot stop provides a harsh cut at that point, so the outer 2 meters of the primary is not illuminated by TolTEC.

In the absence of phase errors at the primary, that aperture and illumination will produce a Guassian beam in the far-field with approximate FWHM of 10, 6, and 5 arcseconds at 150, 220, and 280 GHz. However, we know that the observed instrument beam is not Gaussian. To reproduce the aberrations that are seen in the field, we include phase errors at the aperture in our model. These errors allow for imperfections in the instrument's optical chain to be included in the beam model. However they are not directly included, instead we assume all the phase errors can be modeled by linear combinations of the first 28 Zernike polynomials. The Zernike polynomials are a natural basis for modeling phase errors at the instruments aperture.

With this beam model in hand, we fit the coefficients to the 28 Zernike polynomial model to the data. The resulting best fit beams are presented in the middle column of figure 6.3. Our model clearly does a better job including the aberrations present in the real beam than a Gaussian beam would alone. The residuals are shown in the right column of figure 6.3 and are of order $\pm$100 mJy per beam which is less than 10% of the source flux. The resulting phase errors are shown in figure 6.4. While we would expect that the phase should be similar between all three frequency bands this is not guaranteed to be true since the optical path for the three arrays are different in the cold optical system. Thus, the difference between the phase in the 1.1 mm plot and the other two arrays could be attributed to optics unique to that area. Nonetheless, the agreement between the far-field modeled beams and the data is satisfactory.

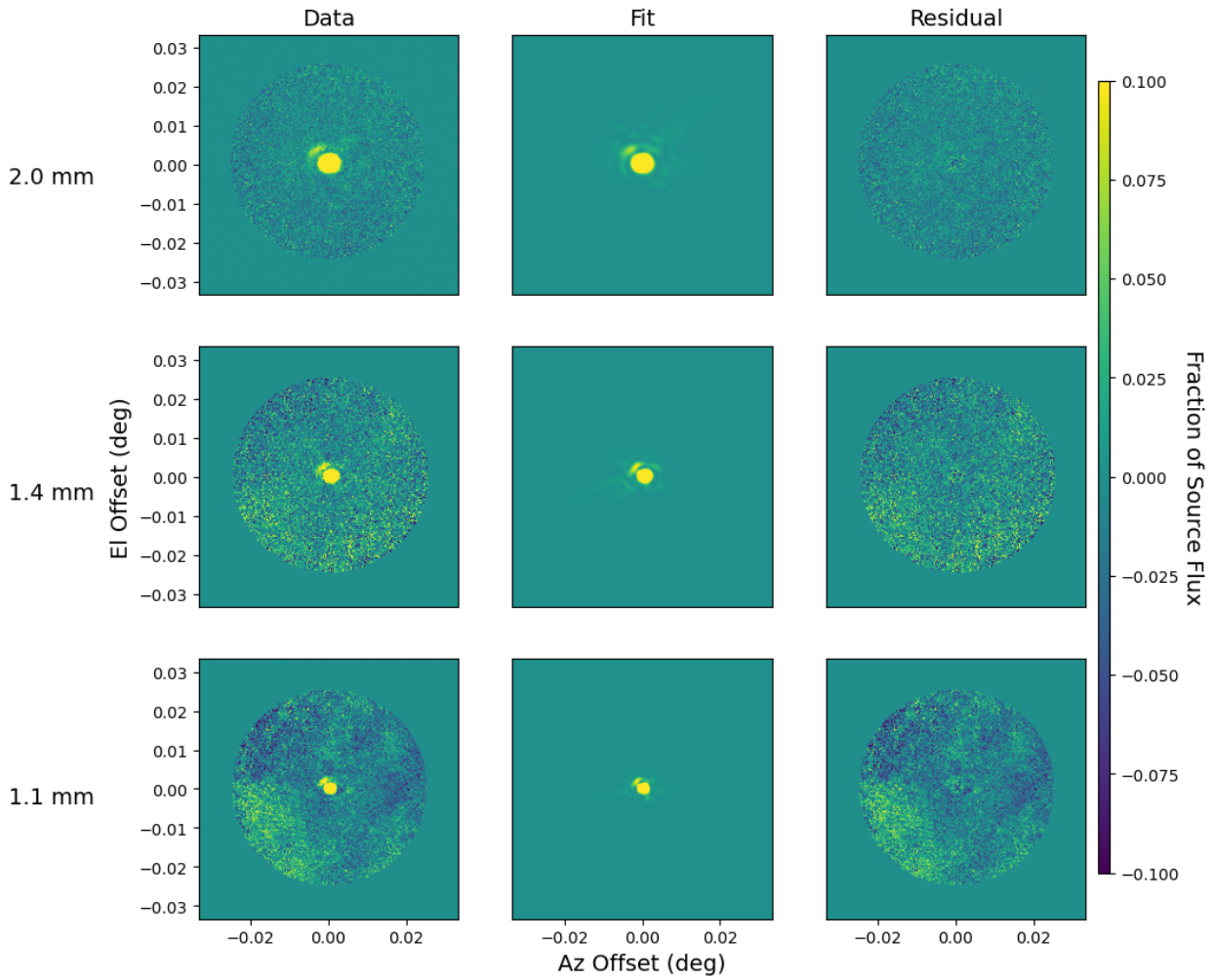

Figure 6.3: Results fitting a beam model to the Crab Nebula pointing data. The left column is the data from the pointing observation. The middle column is the fitted model beam. The left most column is the residual between the data and the model. The rows correspond to the different photometric bands with 2.0, 1.4, and 1.1 mm going from top to bottom. The colorbar is in fraction of the source flux to show that the residuals are less than 10% of the source flux.

6.2 Three Color Images of the Crab Nebula in Intensity and Polarization

TolTEC observed the Crab Nebula for a total of 22 minutes, spread across six different observations. A raster scan strategy measuring 12' by 10.5' was employed, with a scan rate of 2 arcminutes per second and step of 30 arcseconds between rows in the scan. The scan

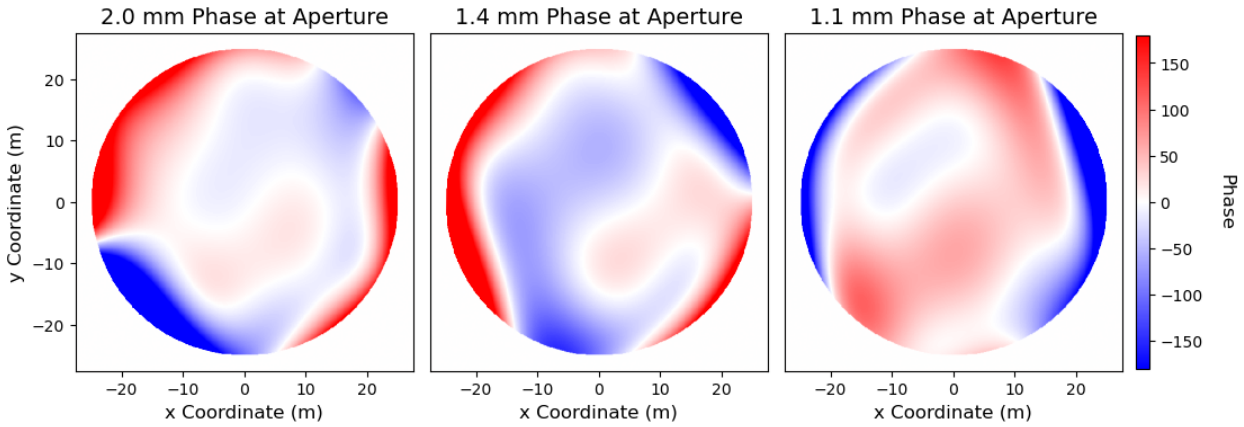

Figure 6.4: Plots of the best fit phase at the aperture for the 2.0, 1.4, and 1.1 mm arrays from left to right.

strategy was rotated relative to the celestial equator a couple of times. As a result, two observations were made with a raster scan along lines of declination, two were performed with the raster pattern angled at 45° to the previous frame, and two were conducted with the raster orthogonal to the original frame. Although TolTEC has the capability to observe with a warm half-wave plate to modulate the polarization of the incident radiation on the camera, this half-wave plate was not utilized during the commissioning observations of the Crab Nebula.

Before presenting the TolTEC images of the Crab Nebula in intensity and polarization, it is useful to briefly cover how the polarization of light is quantified in astronomical images and how the these polarization images were made. Classically, electromagnetic radiation is a wave composed of oscillating electric and magnetic vector fields. These fields oscillate orthogonal to the direction of propagation and the direction of the electric field vector defines the polarization of an electromagnetic wave. Radiation can either be linearly polarized, elliptically polarized, or unpolarized (meaning that the radiation is an incoherent addition of many polarizations). It is also possible for light to be mostly unpolarized but have fraction that is linearly polarized. Due to TolTEC's antenna design, it is only sensitive to linearly polarized or unpolarized light.

Since there is no universal basis for the polarization plane of light, an issue arises for quantifying the direction of polarization. The most common way to quantify the polarization is in terms of the scalar Stokes parameters: I, Q, U, and V. The V Stokes parameter is strictly zero for linearly polarized light, so in the context of TolTEC it can be ignored. The I parameter regards the total intensity of the light whereas the Q and U parameters regard to what degree the light is linearly polarized. The formal definition of the Q and U quantities involves the phase of the electric field, but since TolTEC is not sensitive to the phase the incident light these definitions are not particularly illuminating. Instead, we take advantage of the fact that the I, Q, and U parameters can be completely characterized by carefully planned intensity measurements, and the design of the TolTEC detector array to make a more illuminating definition of Q and U. Each pixel on the TolTEC camera consists of two orthogonal antennae that each independently measure the intensity of incident light. Alternating pixels are rotated 45 degrees with respect to each other, so there are two pixel orientations which we call the + and × pixels. These can be seen in figure 3.9. With these pixel orientations we can then define I, Q, and U as

$$I \equiv S_{+,1} + S_{+,2} = S_{\times,1} + S_{\times,2} = \frac{1}{2}(S_{+,1} + S_{+,2} + S_{\times,1} + S_{\times,2}) \tag{6.1}$$

$$Q \equiv S_{+,1} - S_{+,2} \tag{6.2}$$

$$U \equiv S_{\times,1} - S_{\times,2} \tag{6.3}$$

Where $S_{i,j}$ denotes the intensity measured by an antenna, with i being either the + and × pixel and j denoting which orthogonal antenna in the pixel. This is equivalent to writing the Stokes parameters in terms of the normalized real Jones vectors.

With these definitions of I, Q, and U settled we turn to how we make maps of the Stokes parameters with preliminary TolTEC data. The I maps are straightforward to compute, however the Q and U maps require some care. In the timeframe that TolTEC data was

taken there was not enough time to identify which detectors on the arrays exactly correspond which resonantors tones that are being read out. So we did not have enough information to match timestreams to orthogonal detector pairs and construct the above Stokes parameters directly in timestream space. Fortunately, resonators of antennae with alike orientation are grouped together in the readout frequency sweeps, so we can leverage that information to construct the maps of the Stokes parameters. First, we make intensity maps of each antenna orientation so we essentially make maps of the $S_{i,j}$ defined above. Then we difference these maps as in equations 6.2 and 6.3 to construct the maps of the Stokes parameters in map space. While this is not the ideal way to construct these maps (systematics associated with counts of each antenna type per pixel can arise) for brightly polarized objects like those studied in the TolTEC commissioning this construction is sufficient. The last step for the Q and U maps is to rotate the maps to conform to the convention for the Stokes parameters that the International Astronomy Union uses.

With the knowledge of how to construct the maps for intensity and polarization we are finally able to reveal the maps. We present the resulting coadded maximum-likelihood maps of the Crab Nebula in Stokes I, Q, and U in figure 6.5. Qualitatively we see that the intensity decreases as a function of wavelength which is indicative of sychrotron emission from the nebula. Comparing the 150 GHz image to the image produced by a NIKA, a camera on the 30-meter IRAM telescope, we see the TolTEC images are more detailed owing to the near factor of two increase in aperture size. We present a more quantitative comparison in section 6.2.2.

A unique aspect of TolTEC that sets it apart from other instruments at this angular resolution is its three photometric bands. This means that the intensity images from above can be easily combined into a a single RGB image. To do this, we first convert the units of the maps from mJy per beam to a brightness temperature in μK Rayleigh-Jeans which is an aperture independent unit. This puts the intensity for the three different bands on equal

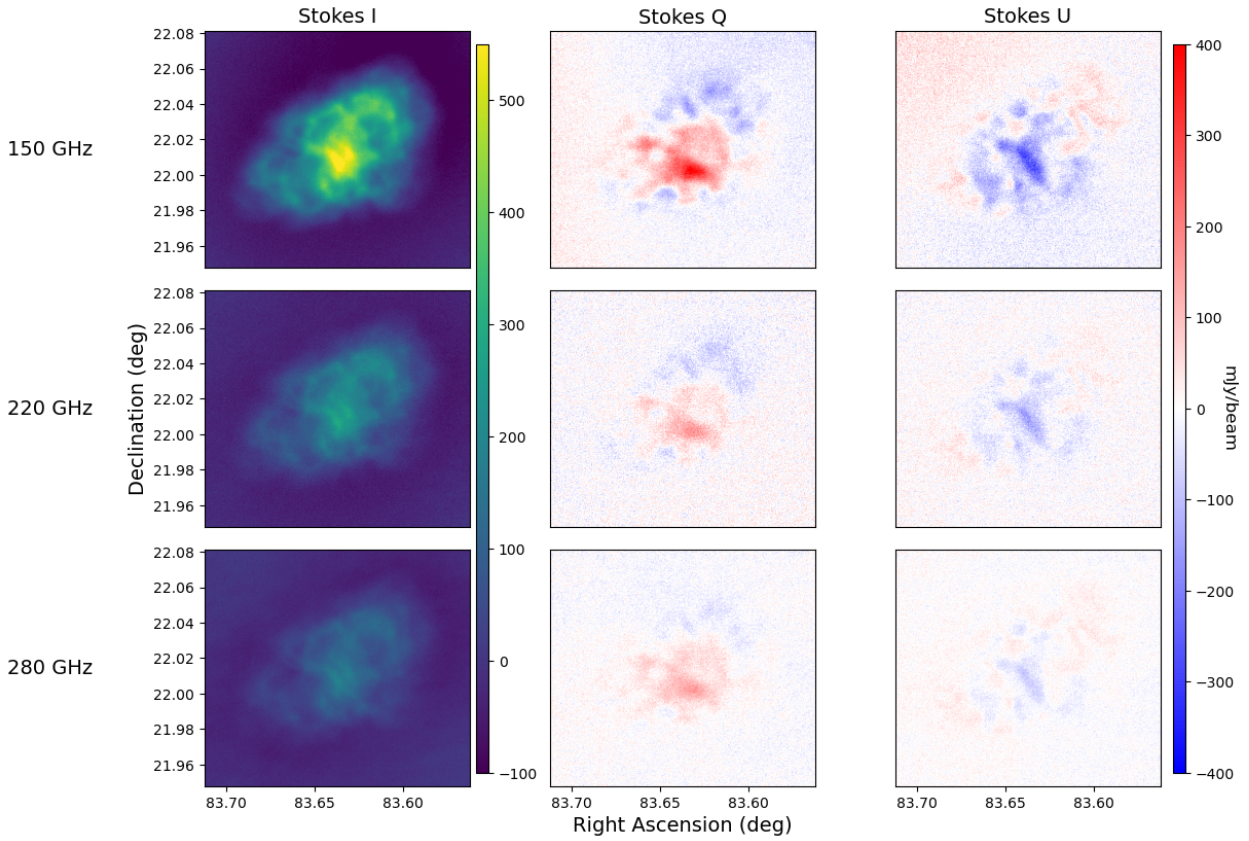

Figure 6.5: Preliminary maps of the Crab Nebula made with TolTEC. From the top row to bottom correspond to maps of 150, 220, and 280 GHz respectively. Left to right corresponds to flux from Stokes I, Q, and U respectively. The linear polarization intensities presented here may still be subject to a rotation calibration.

footing and provides a more accurate comparison between the bands which lends to a more interesting RGB image. Figure 6.6 shows the RGB combination of the Crab Nebula maps. The red, green, and blue layers correspond to the 150, 220, and 280 GHz bands respectively. The emission from the nebula is roughly in the same location for each frequency band which is why the image looks mostly white in color but the reddish-orange tinge is due to the fact that the observed emission is mostly synchrotron radiation which has a negative spectral index and therefore is somewhat brighter at the lower frequencies.

The maps presented in this section represent the highest resolution maps of the Crab Nebula in intensity and polarization at these frequencies that have been made with a single

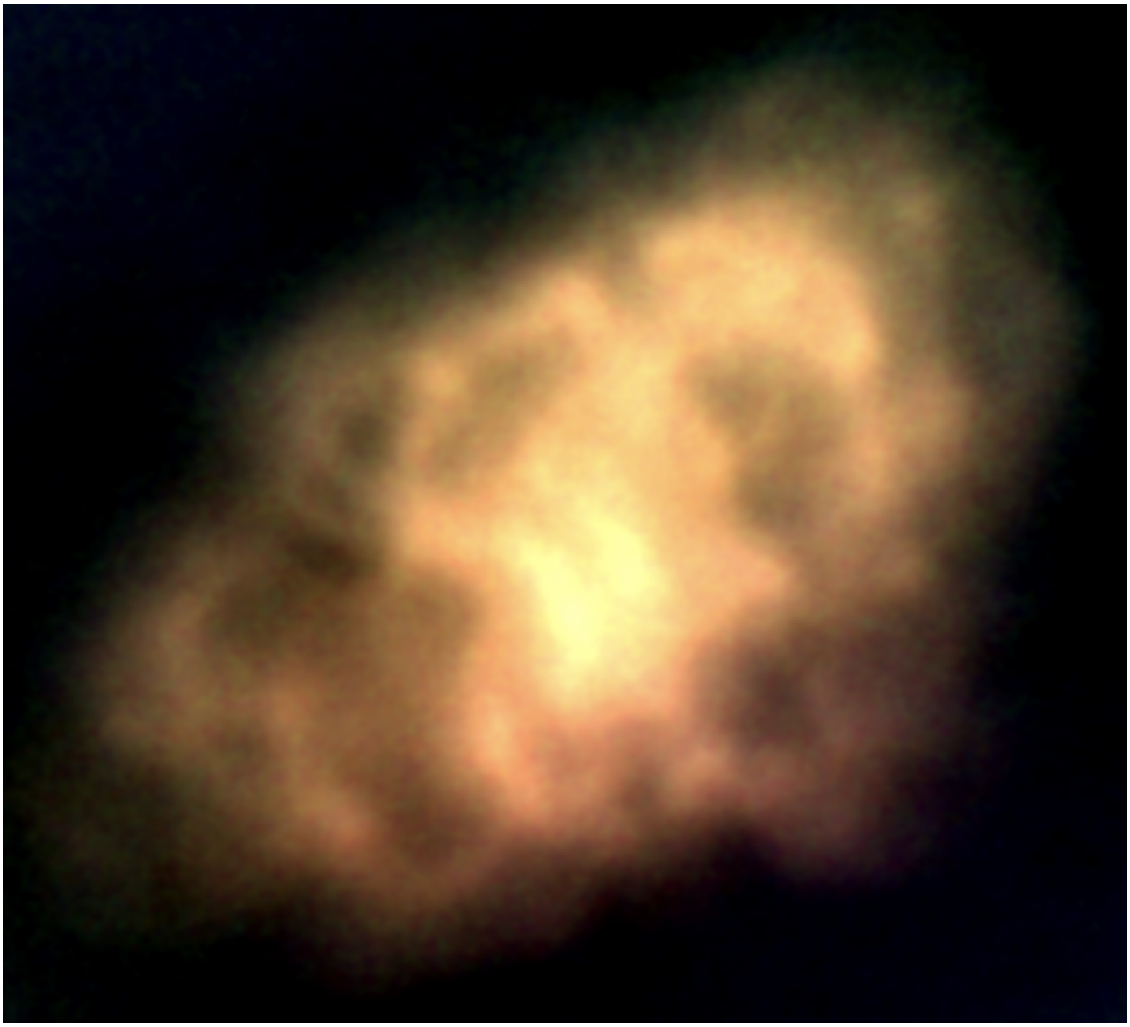

Figure 6.6: Preliminary map of the Crab Nebula made with TolTEC in RGB. The red, green, and blue correspond to the 150, 220, and 280 GHz maps respectively. This Stokes I map was smoothed with a 3 arcsecond FWHM Gaussian kernel to smooth out pixel-scale noise.

dish telescope. The only instrument that can achieve higher resolution at these frequencies is ALMA, but since that instrument is an interferometer its fine synthetic aperture comes at the expense of a small field of view meaning it cannot image the arcminute-scale features that TolTEC captures. Additionally, these images prove TolTEC's ability image polarized intensity simultaneously in three frequency bands. Something that no other instrument can do at this resolution.

6.2.1 Map Noise Properties

Ideally we would like maps with no noise present, but that is not the reality of astronomical observations with known noise sources present. Noise from readout electronics and the atmosphere will contaminate detector timestreams at longer timescales and manifest as $\frac{1}{f}$ noise or pink noise. Disentangling what is noise in the presence of signal can be done in a couple of ways. The simplest is to mask regions of the map that contain signal and analyze the unmasked regions. While simple, this estimation of noise lead to low signal-to-noise features persisting. An alternate and more robust way of estimating noise is to make a coaddition of many observations, difference the coadded map with the individual observations, and then study the differenced maps. This is a robust way to remove signal from maps and the method we choose for our analysis.

We follow the example of noise analysis from the publically available ACT data analysis iPython notebooks that were published with the DR4-DR5 data release [110]. We made maps of the six individual observations that TolTEC made of the Crab Nebula and a coaddition of those observations. Since the edges of the maps have uneven coverage and higher noise we apply a square mask so that only the center of the map where all the observations overlap is analyzed. To reduce any ringing when we perform Fourier transforms, we apply a half arcminute cosine taper to the edges of that mask so the edges smoothly go to zero. Additionally, we mask an elliptical region that is just large enough to cover the source. We made that choice because upon inspecting the difference maps we noticed some residual signal leaking into the difference map. This is most likely due to gain variations at the 10% level and is most likely only an issue because the Crab Nebula is so bright at millimeter wavelengths. As a result of this masking, the total unmasked area that is being analyzed is 62 square arcminutes.

With the mask in hand we then construct difference maps by subtracting individual splits from the coadded map. At the same time we convert from the native map units of mJy per

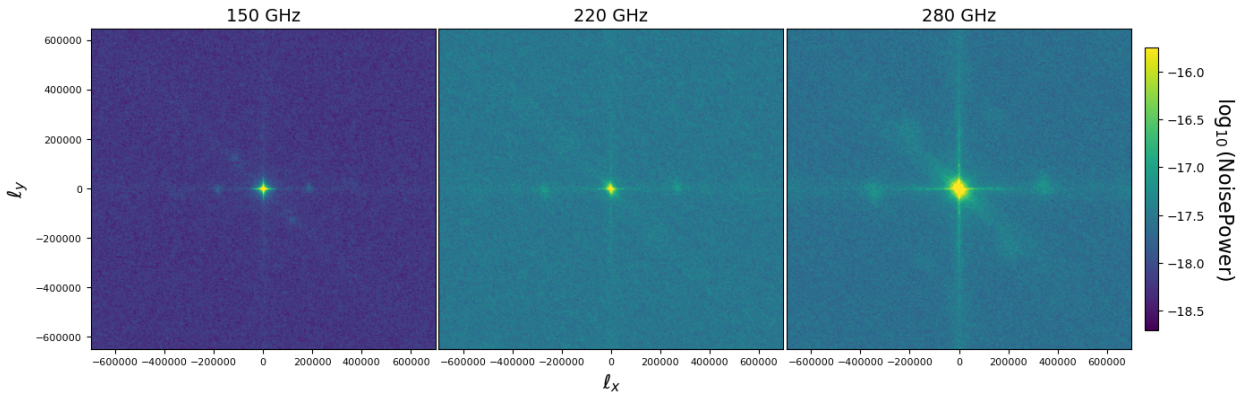

Figure 6.7: The two dimensional noise power spectrum for the TolTEC observations of the Crab Nebula. The noise power is calibrated so the units are arbitrary.

beam to an aperture independent unit of Jy per pixel so that a fair comparison can be made between the noise curves for the three TolTEC photometric bands. The difference maps are then Fourier transformed and multiplied by their complex conjugate in Fourier space to get the noise power spectrum. The noise power spectra of the six independent observations are then averaged in Fourier space. Figure 6.7 shows the two dimensional noise power spectra for each frequency of the TolTEC Crab Nebula observations.

The bright feature at the center of each of the plots can be attributed to $\frac{1}{f}$ noise. The bright lines along $\ell_x = 0$ and $\ell_y = 0$ are explained by noise along the scan directions since a raster scan pattern was employed for the observations. The other bright line that appears at an angle of -45 degrees between ℓ_x and ℓ_y is due to two of the six observations raster scan oriented 45 degrees with respect to lines of constant declination. The faint spots that appear radially outward occur at multipole values that can be associated with harmonics of the instrument beam, hence why the they occur at increasingly higher multipole as the frequency increases. Further investigation is needed to completely understand why these features occur in the power spectra.

To get a more compact picture of the noise from these 2D power spectra, we radially bin the power spectra in ℓ. We present the radially binned noise power spectra in figure 6.8. Again the noise power is not well calibrated so the units on the y-axis should be considered

arbitrary, the important information in this plot is the scales at which the noise arising in the maps. To quantify that, we fit a pink plus white noise spectra of the form

$$N(\ell) = N_{\text{pink}} \left(\frac{\ell}{\ell_{\text{knee}}} \right)^{-\alpha} + N_{\text{white}}$$

to these curves with the goal to measure the ℓ-knee of transition from pink to white noise. The fits of the data to the model are plotted with dotted lines. The discrepancy of the fit with the data at low multipole is most likely due to the size of the map, not many large modes exist in the map.

We summarize the fitted parameters in table 6.1. Notice that the ℓ_{knee} is increasing with frequency which would be expected as effects like the atmosphere get worse with frequency. Additionally note that the white noise floor is the best at 150 GHz but worse at the other frequencies which is expected from the designed noise equivalent temperature (NET) of the detectors [74]. The white noise of the 280 GHz detectors being comparable to the 220 GHz detectors, even though their NET is higher, is due to a failed readout network in the 220 GHz array which means it has around 600 fewer detectors available than design. The difference in the spectral index of the pink noise of the 220 GHz map from the 150 and 280 GHz map is surprising and not fully understood. It may be due to different noise properties of the readout between the frequency arrays.

Table 6.1: Fitted parameters of the radially binned noise power spectra for the TolTEC Crab Nebula observations.

	150 GHz	**220 GHz**	**280 GHz**
N_{pink}	9.7×10^{-19}	1.0×10^{-18}	2.7×10^{-18}
α	3.5	2.9	3.2
ℓ_{knee}	44040	56881	89820
N_{white}	6.7×10^{-19}	3.3×10^{-18}	2.9×10^{-19}

If we convert the ℓ_{knee} multipole values into angular scales, we find that they are only

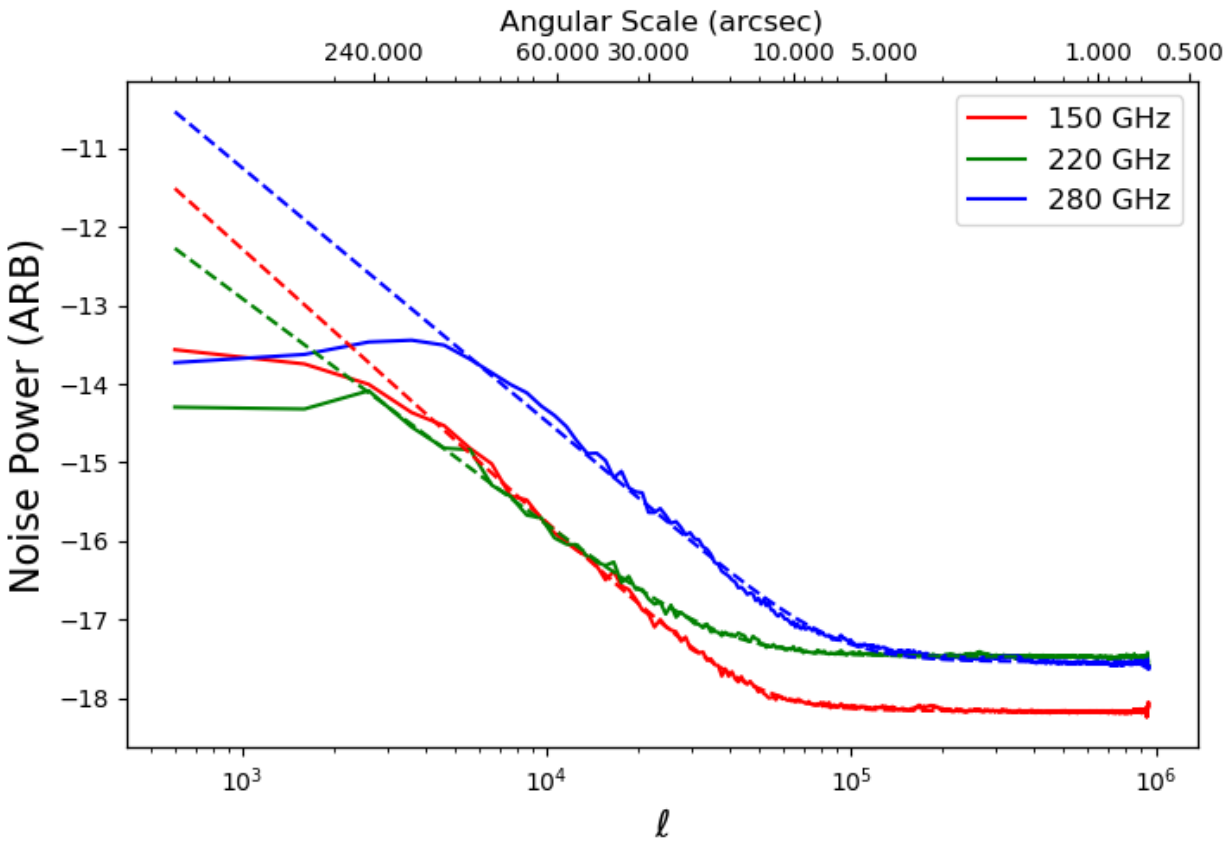

Figure 6.8: Radially binned noise power spectra from the TolTEC observations of the Crab Nebula. The solid lines are the binned power spectra from data and the dotted lines correspond to a best fit model of white plus pink noise.

marginally larger than the instrument beam at those frequencies. This is surprising as we would expect those values to be closer to the instrument FOV. This is most likely due to the readout noise being higher than expected. If the system was photon-noise dominated then you would expect FOV scales to be recovered, but as readout noise can cause correlations within network then one could expect the ℓ_{knee} to be smaller than the FOV. Whether this can explain why it is only slightly larger than the beam size still needs to be investigated.

6.2.2 Integrated Flux

We use aperture photometry to measure the flux, but first we correct for large scale negative modes in the three maps. If uncorrected these would bias our measurement of the fluxes lower than reality. To correct for the negatives we mask all positive values in the map to model the left over negative values. We then subtract that model from the map so that the mean signal of the area around the nebula is zero. Since the negative modes encompass the nebula we additionally subtract a top hat within the nebula that is equal to the mean of the modeled negative flux regions. This naive background subtraction comes at the cost of an additional systematic error which we add to the final error budget of our measurement.

With the large scale negatives corrected, we perform the aperture photometry. We sum the flux within increasing circular apertures around the nebula until the cumulative flux plateaus. The values of the plateau is then the integrated flux of the nebula. We plot our results for the integrated flux in figure 6.9. The error bars for the TolTEC measurements are the quadrature sum of a 10% flux calibration error and the standard deviation of the modeled negative subtraction. The statistical error is subdominant to those two systematic errors. We also plot the Crab Nebula flux as measured by WMAP, *Planck*, and NIKA [111–113]. The TolTEC values are consistent with the values measured by those experiments.

We hope to improve the systematic sources of error in this measurement in two ways. First, the overall gain calibration of TolTEC can be improved with more frequent beammap measurements of thermal emission of astronomical sources like planets and asteroids. Issues with the LMT ephemeris during the December 2022 commissioning lead to problems tracking Uranus during beammap observations which was supposed to be a primary calibrator so a radio galaxy was used instead. Radio galaxies are non-ideal calibration sources since their emission can flare on day timescales. We know via observations of other radio galaxies that the scatter in our calibration is at the 10-15% level and thus the source of a large systematic error. Future commissioning observations will feature more stringent calibration based on

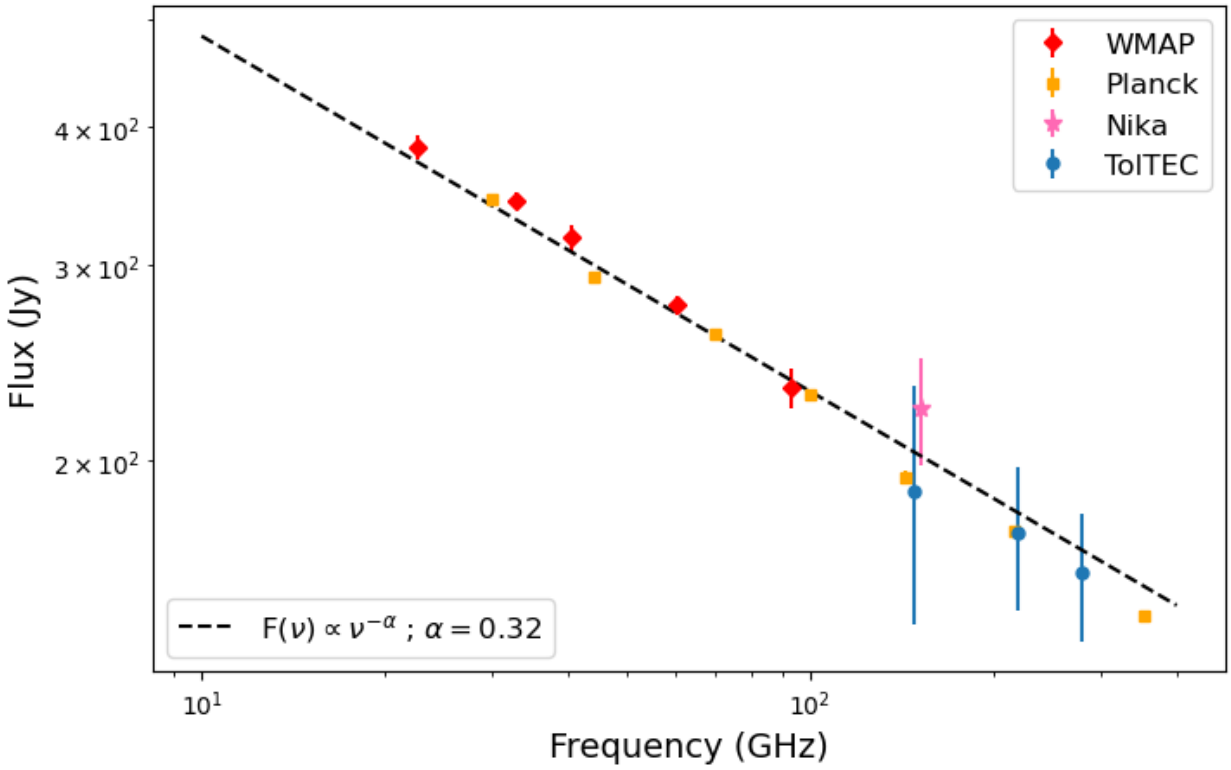

Figure 6.9: Spectral energy density of the Crab Nebula including the measured TolTEC values. Measurements from WMAP, *Planck*, and NIKA are also plotted for reference. The plotted dotted line is a simple power law fit to the WMAP and *Planck* data.

thermal sources.

The second way to improve our systematic error is to improve the maximum likelihood mapmaking pipeline. For bright sources, like the Crab Nebula, we have found that large scale negative modes appear in the maps around the source that cannot be astrophysical in nature. This is thought to be due to how the noise covariance is being estimated in the maximum-likelihood mapmaking pipeline. Since the signal-to-noise of the Crab Nebula is so large an iterative approach is used to estimate the noise covariance. Previous mapmaking iterations are subtracted from timestreams to get better estimation of the noise, but the noise on the largest scales are the last to converge. Investigating better ways to estimate the noise covariance will improve this and resolve the large-scale negative modes. Another avenue to potentially solve this issue is to combine the TolTEC maps with lower resolution

but more sensitive maps from ACT to improve the large scale noise. This is also currently being investigated.

6.2.3 Polarization Properties

We now turn to presenting results on the polarization of the Crab Nebula. Given the uncertainty of the instrumental polarization, we present these results with the caveat that, like the Stokes Q and U maps presented in section 6.2, these images may be subject to an overall rotation. With that being said, the spatial resolution of TolTEC makes these derived polarization quantities incredibly impressive.

First we construct the polarized intensity of the Crab Nebula. From the Stokes Q and U maps presented in section 6.2, we estimate the polarized intensity as the quadrature sum of Stokes Q and U

$$I_{\rm pol} = \sqrt{Q^2 + U^2}$$

This quantity should be independent of any systematic rotation, although if there is induced instrumental polarization that could introduce and error in this quantity. However, with the brightness of the Crab Nebula in polarization we would anticipate those errors to be small.

We present the three color polarized intensity of the Crab Nebula at 150, 220, and 280 GHz in figure 6.10. We find that the polarized intensity is the greatest near the location of the pulsar within the nebula. This is expected as the magnetic fields that generate the polarized synchrotron emission should be the most intense near the pulsar. The observed decrease in polarized intensity with frequency is consistent with the falling synchrotron spectrum. While the ratio of polarized intensity to total intensity, or the polarized fraction, should be consistent across the three frequencies since we are not dividing by the total intensity we expect a falling spectrum.

The linear polarization fraction is found by taking the polarized intensity maps presented

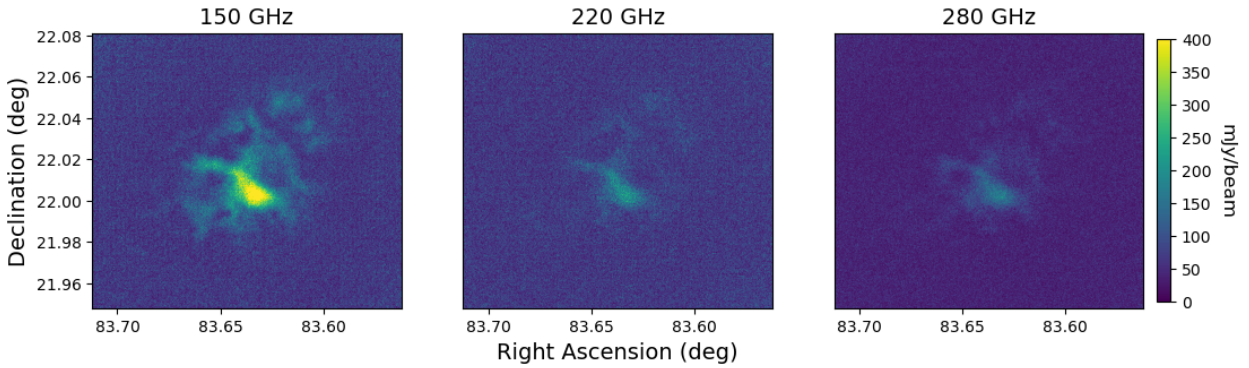

Figure 6.10: Map of the polarized intensity of the Crab Nebula made in three colors by TolTEC.

above and dividing them by the total intensity maps. Doing this with the total intensity maps presented in section 6.2 resulted in a values that disagrees with those measured by NIKA. This can be attributed to the difference in how the Stokes Q and U maps are constructed compared to the Stokes I maps. We instead construct different Stokes I maps made by summing all of the antenna orientations and dividing by two as shown in equation 6.1. These maps still have non-physical negative values in the maps, so we mask all values that are less then 10% of the max in the nebula and add the negative background subtraction found for the total intensity maps found earlier in this section. This gives us an estimate of the polarized intensity only for the highest flux areas of the nebula where there is the most certainty. Even then there is most likely high error in these maps and so they should be considered preliminary. We present the linear polarized fraction in figure 6.11. We note that the polarized fraction is roughly consistent across all three bands although the 150 GHz map has the highest signal to noise. The morphology of the 150 GHz polarization fraction map is more or less consistent with the result from NIKA, although at higher resolution [113]. The highest polarization fraction is around the pulsar but there is significant filamentary polarization fraction throughout the nebula.

The final polarization related quantity to consider is the polarization angle. By the construction of the Stokes Q and U maps, this quantity has the most uncertainty. First,

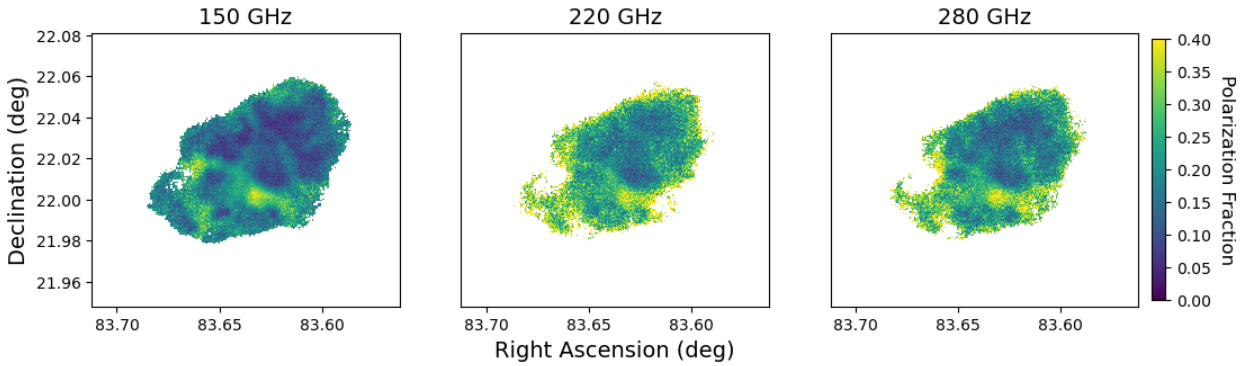

Figure 6.11: Map of the linear polarized fraction of the Crab Nebula made in three colors by TolTEC.

the instrumental polarization is unknown so if the optics cause any rotation this will bias the determination of the polarization angle. Second, by differencing the pair of antenna we are essentially finding the polarization angle in the frame of the detector arrays and there is a rotation needed to get the polarization angle in equitorial coordinates. This rotation is derived empirically through observations of bright polarized quasars that have known polarization angles that are stable. We estimate the uncertainty of this calibration is at the 10-20% level, but this will be greatly improved in the future. The maps of the polarization angle at the three TolTEC frequencies are shown in figure 6.12. The angle is consistent between all three bands as expected and agrees at 150 GHz with the angles reported by NIKA [113].

Future work with TolTEC will constrain this angle even better. The high-resolution measurement of the polarization angle of the Crab Nebula is of great importance to CMB experiments that can leverage these measurements as an astrophysical polarization calibrator for their experiments.

6.3 Conclusion

These early measurements of the Crab Nebula by TolTEC are remarkable. They serve as one of the first demonstrations of TolTEC's next-generation imaging capability.

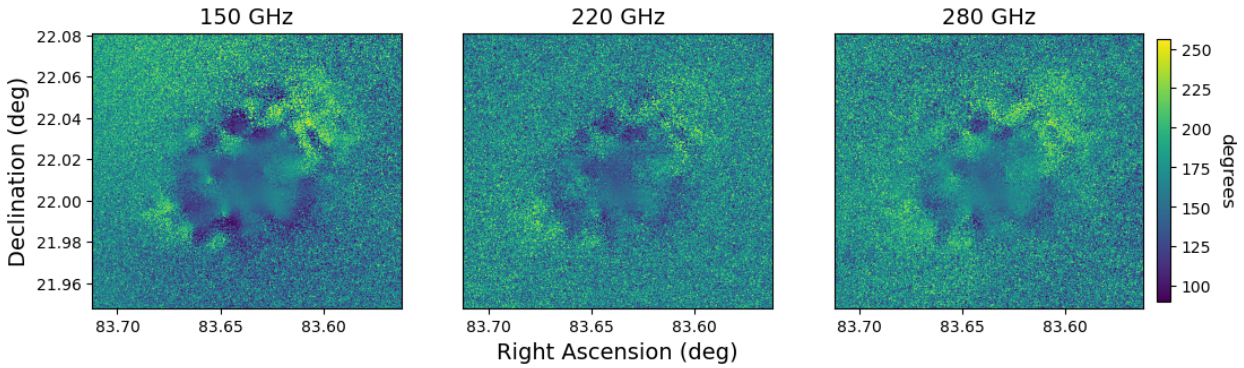

Figure 6.12: Map of the polarization angle of the Crab Nebula made in three colors by TolTEC.

The pointing observations show the angular resolution TolTEC achieves is as designed. They also show that there are aberrations in the instrument beam that remain but can be corrected by adjusting the primary mirror surface and the alignment between TolTEC and the secondary mirror. We presented a model for the instrument beam that accounts for these aberrations and reproduces the beam with percent-level accuracy.

The Crab Nebula images show TolTEC's ability to make simultaneous measurements in three frequency bands with high sensitivity and angular fidelity. The ability to constrain the polarization properties of the Crab Nebula with roughly 20 minutes of integration time is remarkable and will only be improved as instrument commissioning continues. Future improvements to maximum-likelihood mapmaking of bright sources will eliminate some of the systematic uncertainties that plague these measurements of total intensity and empirical measurements of the instrument polarization will improve the polarization measurements. There is no other instrument in the world that has TolTEC's imaging capabilities at these frequencies and resolution. This chapter demonstrates why that is so impressive.

CHAPTER 7

GALAXY CLUSTER FORECASTS WITH SO AND TOLTEC

So far, we have presented the science background motivating galaxy cluster observations, two instruments, the SO LAT and TolTEC camera, that are going to make the next-generation of galaxy cluster observations, state-of-the-art metamaterial AR coatings that were developed and fabricated for the refracting optical elements in those instruments, and preliminary results from the commissioning of TolTEC. Now we turn to forecasting what these instruments will be able to achieve in the coming years.

In this chapter we describe forecasts of constraints that the SO LAT will make on cosmological quantities over its lifetime, plans for immediate cluster observations during TolTEC's continuing commissioning phase, mock TolTEC observations of a simulated cluster and the recovery of SZ quantities from those mock observations, and finally we conclude with preliminary ideas of a 100-hour TolTEC Cluster Legacy Survey.

7.1 SO Cluster Cosmology Forecasts

The SO LAT will achieve first light in 2025 at the earliest and will begin its survey of nearly 40% of the sky. The current best estimate of instrument sensitivities, which have been measured in the lab, show that the SO LAT will reach its baseline sensitivity [104]. That means SO will image 40% of the sky to depths of 8.0, 10, 22, and 54 μK-arcmin in the SZ-relevant bands of 90, 150, 220, and 280 GHz [54]. These map depths are comparable to the depths achieved by SPT in the maps they used for their cluster cosmology analysis but will be over a larger portion of the sky [30].

The complete science forecasts for SO are covered in the SO science goals and forecasts paper from 2019 [54]. We wish to highlight several science points made in that paper which related to science cases we presented in chapter 2. Mainly the constraints on cosmology that

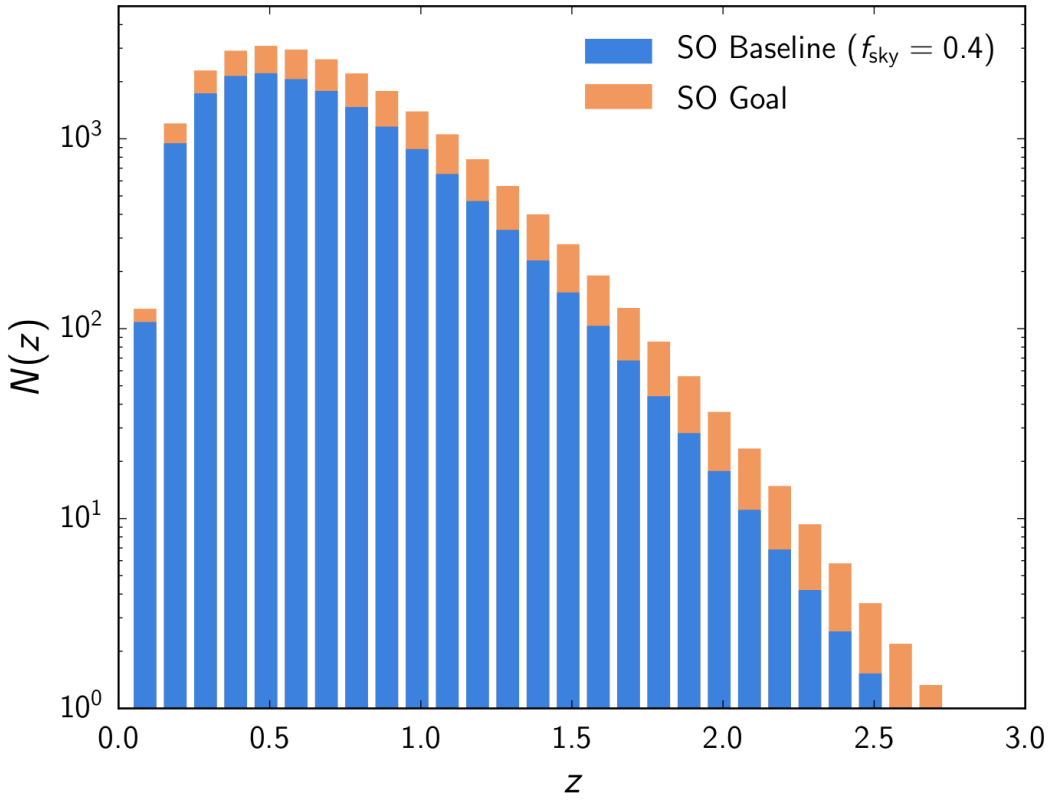

Figure 7.1: Galaxy cluster abundance forecast by SO [54]. The baseline bars are what is realistic for the instrument at this point in time.

can be made with SO cluster counts.

At baseline sensitivity, SO is forecast to observe 16000 clusters [54]. That is around a factor of four increase over the ACT DR4 cluster catalog [24] and a significant increase over the SPT catalogs [22, 23]. We reproduce the SO forecast for galaxy number count as a function of redshift in figure 7.1.

This increase in cluster number counts is not necessarily what will lead to better cosmological constraints as the dominant systematic to using clusters for cosmology remains the SZ to mass scaling relation. Fortunately, SO shares a survey area with next-generation optical surveys, like the Rubin Observatory [114]. For clusters up to roughly redshift 1.2, Rubin will be able to positively confirm what SO observed is in fact a cluster, measure the redshift to that cluster, and provide a weak lensing mass estimate. Above redshift of 1.2, SO

will rely on IR observatories to confirm the clusters and will use weak lensing of the CMB as a proxy to estimate the mass.

SO does not forecast constraints on Ω_M directly from cluster abunances, as the primary CMB constraints on that will be much tighter than what can be achieved with clusters. However for beyond ΛCDM parameters, SO forecasts that from cluster abundances it will constrain the sum of the neutrino masses to 27 meV, and if dark energy is not a cosmological constant SO will be able to constrain the equation of state parameters w_0 and w_a to an uncertainty of 0.06 and 0.2 respectively. The later constraint is especially interesting in light of recent measurements made by the Dark Energy Spectroscopic Instrument [115].

Beyond the cosmological constraints that SO will make with galaxy cluster number counts, the nearly 20000 clusters that it will identify will be ripe for follow up with other instruments. The SO cluster catalog will provide new and interesting targets for X-ray instruments and for high-resolution millimeter wavelength observatories like TolTEC.

7.2 Future Targeted Observations with TolTEC

While TolTEC achieved first light in 2022, it has yet to make significant cluster observations. This is due to bugs being worked out that have limited the instrument's sensitivity as well as lack of integration time on the sky due to issues with the LMT. In lieu of cluster images from TolTEC's ongoing commissioning campaign we present a list of clusters that TolTEC will observe as part of commissioning and the anticipated integration time for each cluster. We will then show some simulations made with realistic cluster inputs to show what TolTEC will observe when it is operating at designed sensitivity. Additionally we will show what tSZ signal can be recovered from those simulations using an internal linear combination (ILC) of the simulated data. Lastly, we will conclude with a discussion of a future 100-hour TolTEC Cluster Legacy Survey and what that can give to the science community.

7.2.1 Commissioning Cluster Observations

As part of TolTEC's commissioning program it plans to observe three different clusters: MACS J0717.5+3745, MACS J1206.2-0847, and MACS J1149+2223. MACS0717 will have two hours of integration time whereas the other two clusters will only have one hour each. The goal of these commissioning observations is to demonstrate that TolTEC can achieve a reasonable signal to noise in a brief integration time. Additional observations of these clusters can be made to increase the depth of the observations.

The benefit of observing these clusters as part of commissioning is that there is a large amount of ancillary data for them. They are all CLASH clusters so there is HST weak lensing data, and two of them, MACS0717 and MACS1149 are Frontier Fields clusters [116, 117]. These clusters were also imaged with the precursor instrument to TolTEC on the LMT, AzTEC.

The observations of these clusters should conclude by the end of 2024 or early 2025 at the latest. After which TolTEC science observations will begin.

7.2.2 TolTEC Observation of a Simulated Cluster

To anticipate what TolTEC will measure when it eventually spends time observing clusters, we use simulations of the SZ effect, input those simulations into a mock observing simulation pipeline that was developed for TolTEC to generate mock timestreams, and then make maps with those timestreams. From those maps we then use an ILC to separate the tSZ and kSZ components from the map and see how that compares to what we input.

For the input to the simulation pipeline we used a simulated galaxy cluster from the Omega 500 simulations[1] [118]. This is a large scale N-body plus gas-dynamics dynamics simulation that used the Adaptive Refinement Tree code [119]. The cosmological simulation used a box size of 500 Mpc comoving and re-simulated the regions around the halos with

1. https://gcmc.hub.yt/omega500/index.html

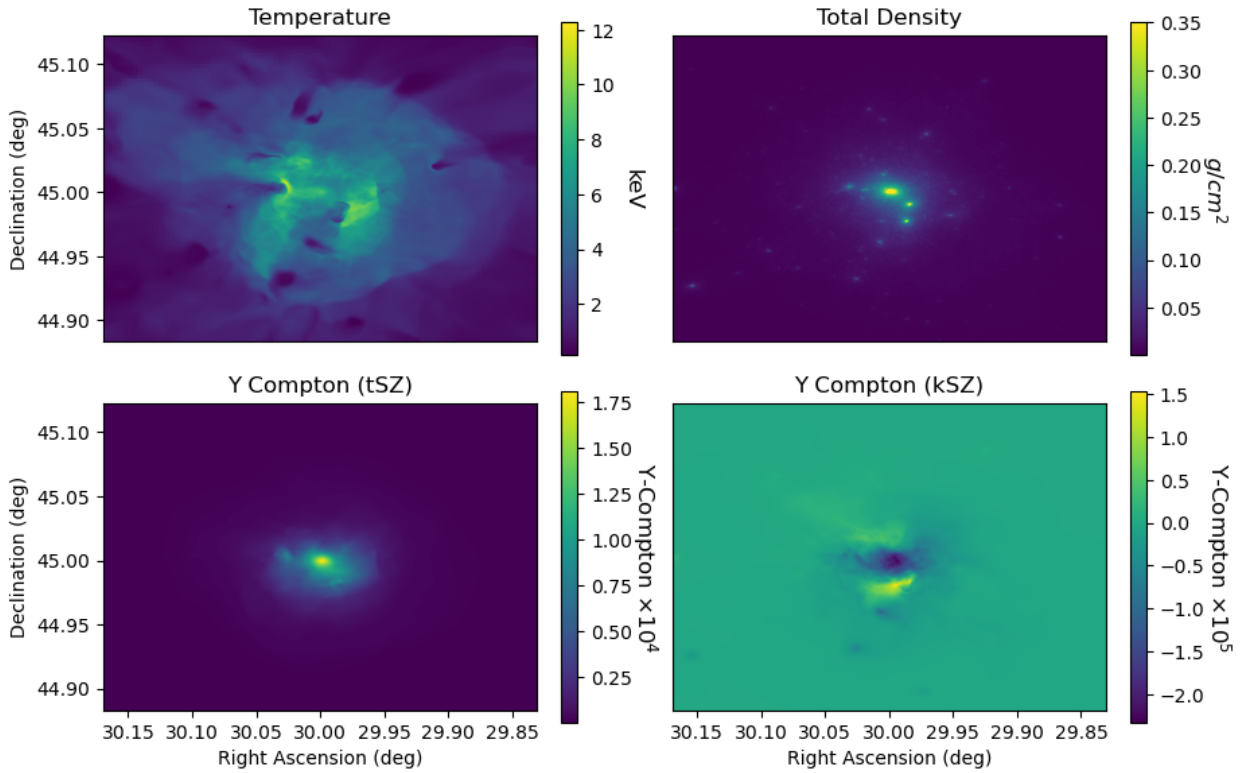

Figure 7.2: Simulated quantities of HaloID 13 from the Omega 500 simulations.

$M_{500} > 3 \times 10^{14} h^{-1} M_{\odot}$. From this catalog we selected HaloID 13 and used the x projection of that cluster.

The clusters presented in the catalog are at degree scales which is unfeasible to observe with TolTEC so we push the cluster back in time so it has an angular scale of a more representative cluster at a higher redshift. We show the scaled simulation images in figure 7.2. While the total density plot is useful to understand where subhalos are in the images and the temperature plot helps to identify where shocks occur, the two plots of the tSZ and kSZ Y-Compton are what we desire to make images in the millimeter-wave. We take those two tSZ and kSZ plots and use the spectral shifts in CMB brightness from section 2.3.1 to get the brightness in TolTEC's photometric bands. We add the signal from both the tSZ and kSZ together to make the final images to input into the TolTEC simulator.

A full observing simulator called TolTECA simu was developed by the TolTEC collabora-

tion [120]. This simulator takes input image files, actual telescope observing scripts that are used for real observations, generates realistic detector and atmospheric noise, and outputs timestreams in the format of actual TolTEC timestreams. Those timestreams are then run through the same mapmaking pipeline described in section 5.2.

We mock observed this cluster for a total of five hours across three nights. The scan strategy employed was a 6 arcmin by 6 arcmin double lissajous which covers an effective area of around 100 square arcmin. Each night contained four observations of half an hour each. The scan strategy was rotated 45 degrees for each observation to symmetrize any noise associated with the scan strategy. We used the designed TolTEC detector counts and noise properties for these observations.

We ran the timestreams through the TolTEC maximum-likelihood pipeline. This was the first real exercise of the maximum-likelihood mapmaking pipeline with several hours of timestreams as the input. As a result, we ran into some memory issues associated with loading in all of the timestreams so the decision was made to downsample the timestreams from 122 Hz down to 41 Hz which should not effect the output maps since the scan speed of the telescope would put all signals below roughly 16 Hz, so we are still Nyquist sampling the signal. Since the signal-to-noise of the cluster is much lower than the other test cases like the Crab Nebula, we found that the iterative mapmaking method needed to recover the extended flux in those maps were not needed and instead one mapmaking iteration of 100 steps in the PCG were sufficient to get quality maps.

We plot the maximum-likelihood maps in figure 7.3. One can clearly see the SZ decrement in the 150 GHz map and a hint of the increment at the cluster core in the 280 GHz map. There is even very low signal-to-noise features in the 220 GHz map which bodes well for the direct imaging of the kSZ effect. There does appear to be significant atmospheric contamination in the 220 and 280 GHz maps. The intended atmosphere model was supposed to the top 25th percentile of good observing however there is a known issue in the scaling of this model

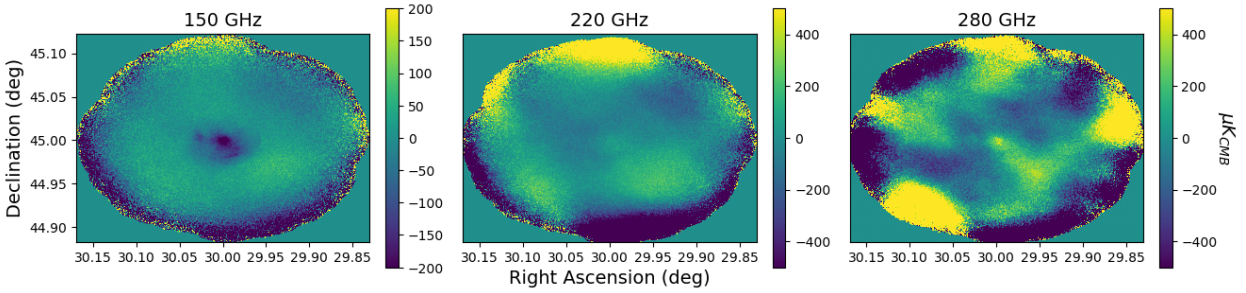

Figure 7.3: Maximum likelihood maps made with simulated TolTEC observations at 150, 220, and 280 GHz.

with a realistic atmosphere generated by TOAST. The result is atmospheric emission that is quite harsh, so this should be interpreted as data taken in medium to poor quality weather.

While we can see that the SZ signals are present in these maps, there is also clear atmospheric contamination. To extract the SZ signals in the presence of atmospheric foregrounds we employ an ILC to separate the SZ components for which we know the spectral dependence. ILCs leverage the multifrequency maps of the sky and the differing spectral dependence of the signals in those maps. Each map at the different frequencies that ToTEC observes at can be modeled as a sum of different signal components multiplied by a weight that corresponds to the spectral response of that component at that frequency plus noise.

$$M_i = \sum_j a_{i,j} S_j + N_i$$

Above M_i corresponds to the map at the i frequency (i.e. 150, 220, or 280 GHz), S_j corresponds to the jth signal component (i.e. the tSZ or kSZ signal), $a_{i,j}$ represents the spectral response of the jth signal component at frequency i, and N_i represents the noise in band i.

The aim of ILC component separation is to reconstruct a S_j map with only the set of M_i maps and known $a_{i,j}$ spectral response. If one is only interested in a single signal component,

$$M_i = a_i S_{\text{interest}} + \sum_j b_{i,j} S_j + N_i$$

then one finds that the reconstruction of S_{interest} that has minimum variance is given by

$$S_{\text{interest}} = \sum_i w_i M_i$$

with the weights w_i being given by

$$w_i = \frac{a_j (C^{-1})_{ji}}{a_j (C^{-1})_{jk} a_k}$$

with $(C^{-1})_{ij}$ being the inverse of the covariance matrix between map at frequency i and frequency j [121,122]. This is essentially an inverse covariance weighted average of the maps. For our case we are interested in recovering a minimum variance reconstruction of the tSZ signal from our simulated maps so the a_i are given by the tSZ spectrum defined in 2.3.1 and the covariance matrices are calculated from the maps themselves.

We calculate these quantities with the simulated maps and show the minimum variance reconstruction of the tSZ signal in figure 7.4. The tSZ signal that we recover is roughly 60% lower than the original tSZ map that was input into the simulator. We ran multifrequency maps with no noise through the single component ILC reconstruction and recovered maps that were identical to the input, so this 60% loss is occurring somewhere in the simulator and mapmaking pipeline.

Attempts to made a minimum variance reconstruction of the kSZ signal are more difficult since the kSZ has unit response across the three TolTEC frequency bands in CMB brightness temperature units. This means that if there are gain mismatches or other correlated signals between the maps, like the atmosphere, then those signals will leak into the kSZ map. Therefore a more sophisticated approach to component separation must be made.

We turn to the multicomponent ILC reconstruction to do attempt to reconstruct the

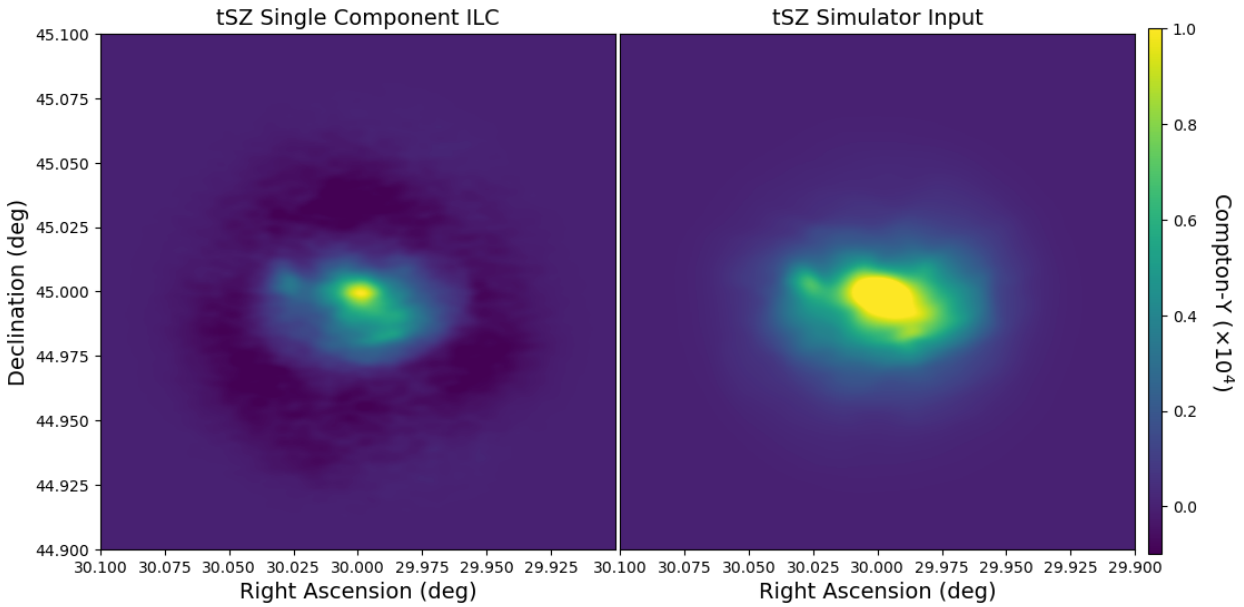

Figure 7.4: (Left) Minimum variance reconstruction of the tSZ signal from the simulated maps of the cluster. (Right) The original simulated tSZ signal that was input into the TolTECA simulator.

kSZ signal. This method takes the model of the sky from above and instead of considering one component that we wish to recover it considers two components, one we would like to recover and one we wish to null (i.e. the weights in the ILC construction with respect to that component sum to zero) [121]. In this case the model of the sky is represented as follows, and now we are explicit with the tSZ and kSZ signal maps,

$$M_i = a_i S_{\mathrm{tSZ}} + b_i S_{\mathrm{kSZ}} + N_i$$

So we have two options in this case, we can construct a tSZ map with the kSZ signal nulled or a kSZ map with the tSZ signal nulled. In the tSZ with the kSZ signal nulled case the weights in that the multifrequency maps are averaged with become

$$w_i = \frac{(b_k(C^{-1})_{kl}b_l)a_j(C^{-1})_{ji} - (a_k(C^{-1})_{kl}b_l)b_j(C^{-1})_{ji}}{(b_k(C^{-1})_{kl}b_l)(a_k(C^{-1})_{kl}a_l) - (a_k(C^{-1})_{kl}b_l)^2}$$

To get the weights for the kSZ signal with the tSZ nulled simply replace the a_i above

with b_i and vice versa.

We construct the two maps of each component with the other component nulled and they are shown in figure 7.5. We can see low signal-to-noise tSZ and kSZ features in each of these maps, but there are significant large scale artifacts in each of the reconstructed maps. We again confirm that the multicomponent ILC returns the tSZ and kSZ input when maps with no noise are used, so the large scale features are due to the noise in the maps. To test this, we increased the signal of the maps that are input into the TolTECA simulator by a factor of ten which dramatically increased the signal-to-noise in the simulated maps. We found that with those maps we were able to recover the tSZ and kSZ signals using the multicomponent ILC procedure.

Unfortunately increasing the signal that is input into the simulator by a factor of ten is equivalent to observing the cluster by a factor of 100 longer which is not realistic, so we are investigating other ILC techniques that can deal with signals that occur at different scales. From the maps in figure 7.3 we can see that the atmospheric noise occurs at a larger angular scale than the cluster signal we are trying to recover. Instead of making weights that are flat across all angular scales like we did above, it would be better to construct weights that not only incorporate the spectral information from the component signals but also the spatial information in Fourier-space [123]. This is currently ongoing work to improve the signal reconstruction with TolTEC maps.

Another avenue that can improve the noise in these maps at larger scales is to combine the TolTEC maps with an instrument that has lower noise at the larger angular scales. The SO LAT is a perfect instrument that has white noise at the arcminute scales where the atmospheric noise dominates the TolTEC maps. This can be seen by looking at the noise power spectrum of TolTEC and SO LAT together which is plotted in figure 7.6. Where the noise from the SO LAT starts to dramatically increase due to the finite beam size is where TolTEC begins to be the most sensitive. Likewise at the larger angular scales where the

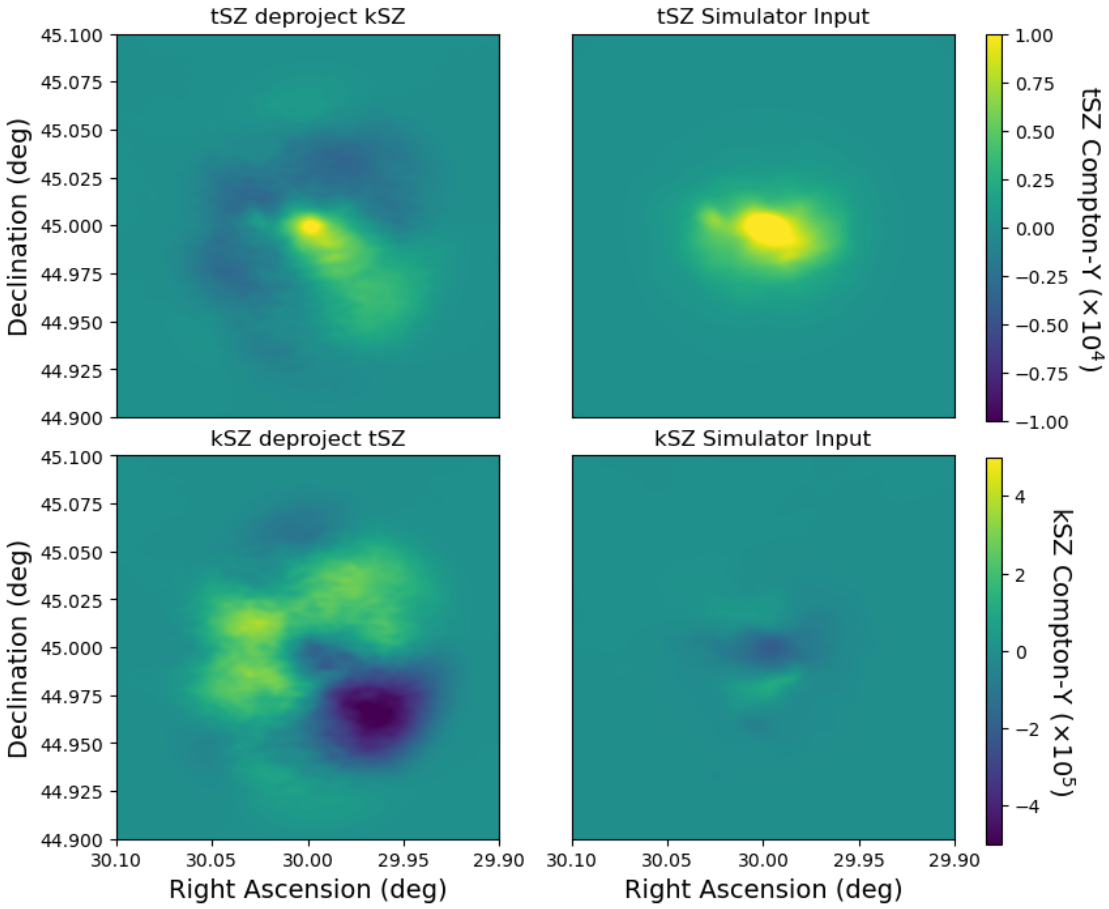

Figure 7.5: (Top Left) Reconstruction of the tSZ signal with the kSZ signal nulled made from the simulated maps of the cluster. (Top Right) The original simulated tSZ signal that was input into the TolTECA simulator. (Bottom Left) Reconstruction of the kSZ signal with the tSZ signal nulled made from the simulated maps of the cluster. (Bottom Right) The original simulated kSZ signal that was input into the TolTECA simulator.

TolTEC noise is increasing due to $\frac{1}{f}$, the SO noise is flat and several orders of magnitude lower.

We are currently working on combining the simulated TolTEC and SO maps following a prescription used by SPT to combine their maps of the LMC with *Planck* [124]. This work is currently underway and does not yet have results, but if one looks at the simulated TolTEC and SO maps side-by-side in figure 7.7 one can see the power of the large scale information SO maps will add.

In summary, we took the tSZ and kSZ information from a simulated cluster and put it

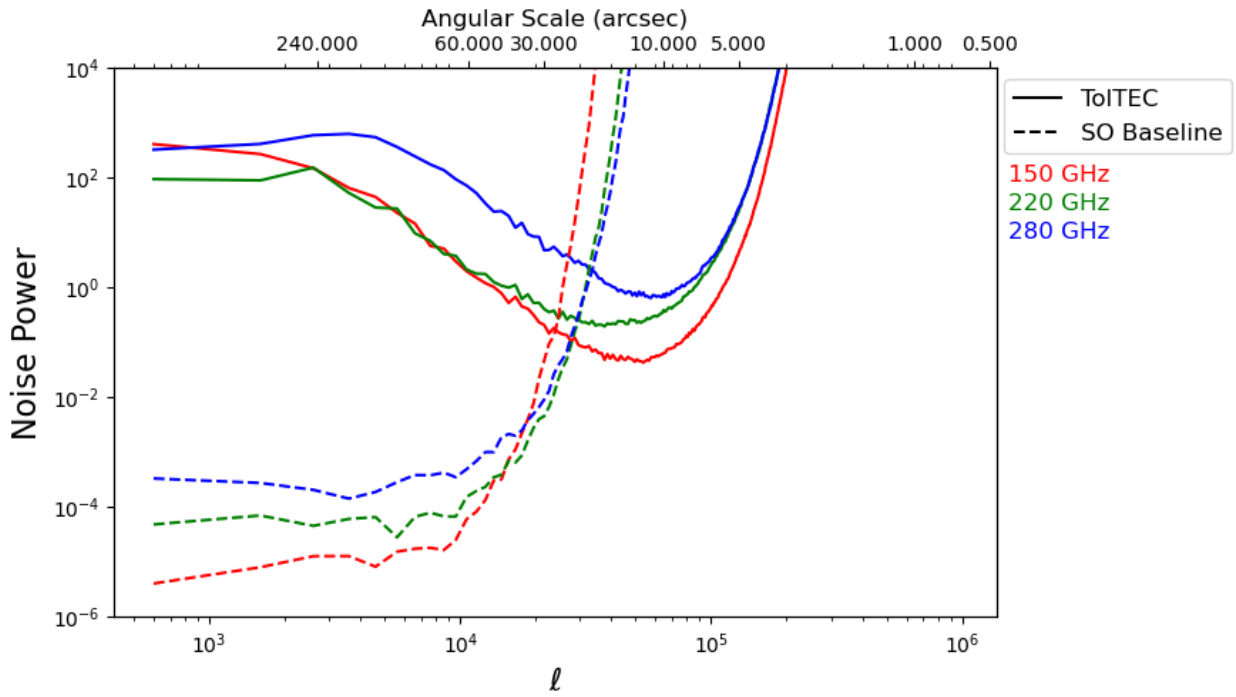

Figure 7.6: Noise power spectra for SO and TolTEC. The SO noise uses projects baseline map depths and the TolTEC curve uses the noise power spectrum found in section 6.2.2. Both curves deconvolve the instrument beams.

though a simulation pipeline that replicates actual observations with the TolTEC instrument. We then took the output of that simulator and made maximum-likelihood maps of those simulated observations. Those maps have decent signal-to-noise but suffer from large scale noise. We then attempted to make reconstructions of the tSZ and kSZ signals using ILC methods. We find good that the minimum variance reconstruction of the tSZ morphologically agrees with the input tSZ map however work remains to understand why the recovered signal is roughly 60% the magnitude of the input. The multicomponent ILC methods recover acpects of the tSZ and kSZ signals but at low signal-to-noise and with large scale noise present. We have identified two ways to improve our reconstructions, ILCs that leverage harmonic space information and combining the TolTEC maps with SO, and we are currently working towards implementing those methods. Overall, this exercise of forecasting images of clusters that will be made with TolTEC shows immense promise.

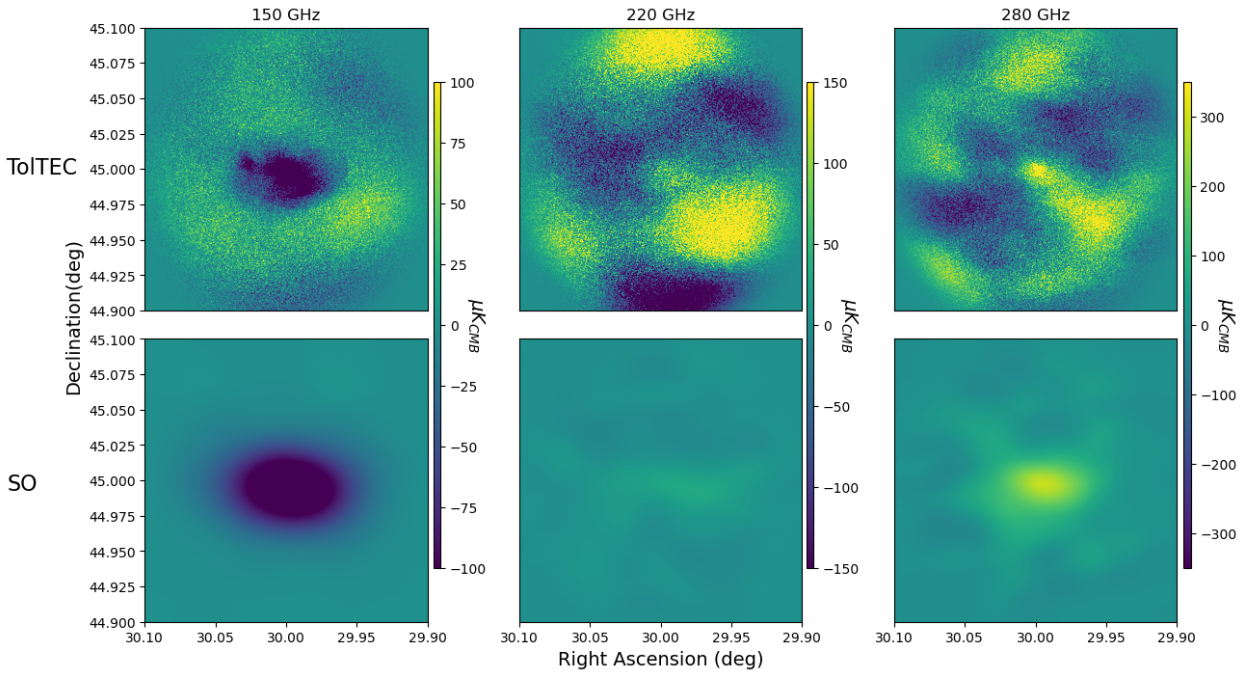

Figure 7.7: (Top Row) Simulated TolTEC maps of the cluster at 150, 220, and 280 GHz. (Bottom Row) Simulated SO maps of the cluster at 150, 220, and 280 GHz.

7.2.3 Future 100-hour Cluster Legacy Survey

We have outlined future immediate work that is underway with TolTEC clusters, mainly observing clusters and working with simulations to build a pipeline that recovers important cluster signals, but we would like to conclude this dissertation with a discussion of far-future work that can be done with TolTEC and that would be a great service to the broader cosmology and astronomy community. The current number of high-resolution cluster images that exist at millimeter wavelengths is limited to observations made by MUSTANG2, Bolocam, and a few other instruments like ALMA. These observations are either limited in resolution, field of view, or frequency coverage. A multifrequency high-resolution sample of 50-100 clusters across a range of redshifts would revolutionize our understanding of the physics that occur within the ICM. This is important for the calibration of hydrodynamics within the ICM for simulations and calibrating the Compton y to mass scaling relations.

The NIKA2 experiment has finished a 300 hour survey of roughly 50 galaxy clusters

and will soon release their results [125]. This catalog will be remarkable and a step in the next-generation of cluster observations. To go even further, a similar study needs to be done with TolTEC which has twice the resolution of NIKA2, roughly an order of magnitude greater sensitivity, and an additional photometric band. We estimate that with 100 hours of TolTEC observing time we could similarly image 100 clusters to a noise RMS of roughly 200 μK at 150 GHz. If the selection of cluster for TolTEC's program were to avoid clusters selected by NIKA2 then the combination of the TolTEC and NIKA2 catalogs would mean that there would be over 150 clusters imaged with sub-arcminute resolution. That is a statistically significant sample. To see how impressive this sample would look, we took 100 of the clusters from the Omega 500 simulations and added white noise consistent to one hour of observing time. We plot the resulting 100 cluster sample at 150 GHz in figure 7.8. A sample such as this would begin a new era of cluster astronomy and cosmology.

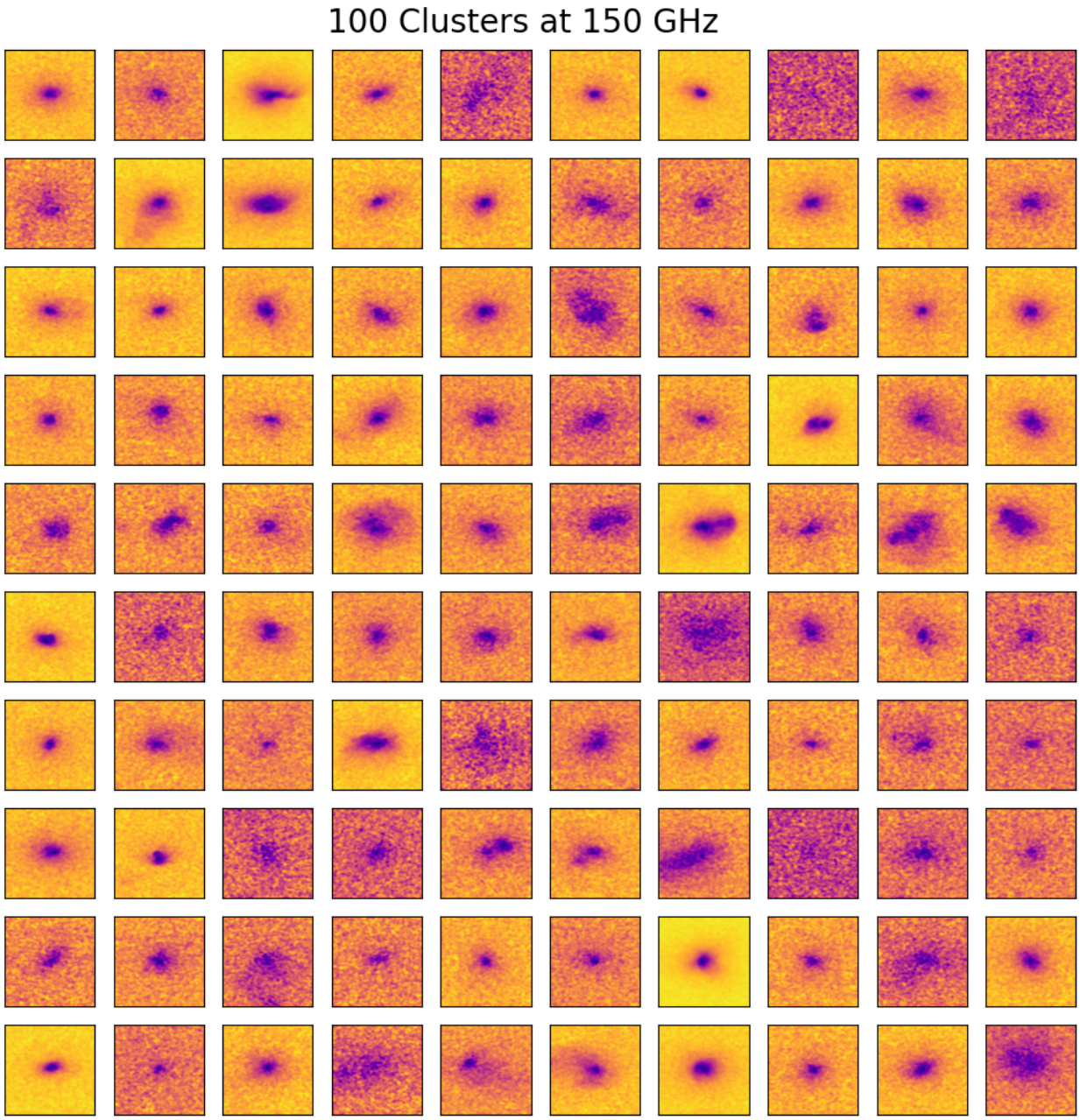

Figure 7.8: Simulations of 100 Clusters at 150 GHz with white noise levels consistent of one hour of TolTEC observations.

REFERENCES

[1] H. Mo, F. Van den Bosch, and S. White, *Galaxy formation and evolution*. Cambridge ; New York: Cambridge University Press, 2010. OCLC: ocn460059772.

[2] W. H. Press and P. Schechter, "Formation of Galaxies and Clusters of Galaxies by Self-Similar Gravitational Condensation," *ApJ*, vol. 187, p. 425, Feb. 1974.

[3] J. R. Bond, S. Cole, G. Efstathiou, and N. Kaiser, "Excursion set mass functions for hierarchical Gaussian fluctuations," *ApJ*, vol. 379, p. 440, Oct. 1991.

[4] R. K. Sheth and G. Tormen, "Large-scale bias and the peak background split," *Monthly Notices of the Royal Astronomical Society*, vol. 308, pp. 119–126, Sept. 1999.

[5] J. Tinker, A. V. Kravtsov, A. Klypin, K. Abazajian, M. Warren, G. Yepes, S. Gottlöber, and D. E. Holz, "Toward a Halo Mass Function for Precision Cosmology: The Limits of Universality," *ApJ*, vol. 688, p. 709, Dec. 2008. Publisher: IOP Publishing.

[6] V. Springel, R. Pakmor, O. Zier, and M. Reinecke, "Simulating cosmic structure formation with the gadget-4 code," *Monthly Notices of the Royal Astronomical Society*, vol. 506, pp. 2871–2949, Sept. 2021.

[7] J. Schaye, R. A. Crain, R. G. Bower, M. Furlong, M. Schaller, T. Theuns, C. Dalla Vecchia, C. S. Frenk, I. G. McCarthy, J. C. Helly, A. Jenkins, Y. M. Rosas-Guevara, S. D. M. White, M. Baes, C. M. Booth, P. Camps, J. F. Navarro, Y. Qu, A. Rahmati, T. Sawala, P. A. Thomas, and J. Trayford, "The EAGLE project: simulating the evolution and assembly of galaxies and their environments," *Monthly Notices of the Royal Astronomical Society*, vol. 446, pp. 521–554, Jan. 2015.

[8] R. A. Crain, J. Schaye, R. G. Bower, M. Furlong, M. Schaller, T. Theuns, C. Dalla Vecchia, C. S. Frenk, I. G. McCarthy, J. C. Helly, A. Jenkins, Y. M. Rosas-Guevara, S. D. M. White, and J. W. Trayford, "The EAGLE simulations of galaxy formation: calibration of subgrid physics and model variations," *Monthly Notices of the Royal Astronomical Society*, vol. 450, pp. 1937–1961, June 2015.

[9] D. Nelson, A. Pillepich, M. Ayromlou, W. Lee, K. Lehle, E. Rohr, and N. Truong, "Introducing the TNG-Cluster Simulation: overview and physical properties of the gaseous intracluster medium," Mar. 2024. arXiv:2311.06338 [astro-ph].

[10] M. Markevitch and A. Vikhlinin, "Shocks and cold fronts in galaxy clusters," *Physics Reports*, vol. 443, pp. 1–53, May 2007.

[11] M. Markevitch, A. H. Gonzalez, D. Clowe, A. Vikhlinin, W. Forman, C. Jones, S. Murray, and W. Tucker, "Direct Constraints on the Dark Matter Self-Interaction Cross Section from the Merging Galaxy Cluster 1E 0657–56," *ApJ*, vol. 606, p. 819, May 2004. Publisher: IOP Publishing.

[12] C. Zhang, E. Churazov, and I. Zhuravleva, "Pairs of giant shock waves (N-waves) in merging galaxy clusters," *Monthly Notices of the Royal Astronomical Society*, vol. 501, pp. 1038–1045, Feb. 2021.

[13] S. Kotecha, C. Welker, Z. Zhou, J. Wadsley, K. Kraljic, J. Sorce, E. Rasia, I. Roberts, M. Gray, G. Yepes, and W. Cui, "Cosmic filaments delay quenching inside clusters," *Monthly Notices of the Royal Astronomical Society*, vol. 512, pp. 926–944, May 2022.

[14] V. N. Zirakashvili and V. S. Ptuskin, "Cosmic ray acceleration in accretion flows of galaxy clusters," *J. Phys.: Conf. Ser.*, vol. 1181, p. 012033, Feb. 2019. Publisher: IOP Publishing.

[15] A. Celotti, P. Padovani, and G. Ghisellini, "Jets and accretion processes in active galactic nuclei: further clues," *Monthly Notices of the Royal Astronomical Society*, vol. 286, pp. 415–424, Apr. 1997.

[16] E. L. Blanton, T. E. Clarke, C. L. Sarazin, S. W. Randall, and B. R. McNamara, "Active galactic nucleus feedback in clusters of galaxies," *Proc. Natl. Acad. Sci. U.S.A.*, vol. 107, pp. 7174–7178, Apr. 2010.

[17] R. A. Sunyaev and Y. B. Zeldovich, "Small-Scale Fluctuations of Relic Radiation," *Astrophysics and Space Science*, vol. 7, pp. 3–19, Apr. 1970. Publisher: Springer ADS Bibcode: 1970Ap&SS...7....3S.

[18] T. Mroczkowski, D. Nagai, K. Basu, J. Chluba, J. Sayers, R. Adam, E. Churazov, A. Crites, L. Di Mascolo, D. Eckert, J. Macias-Perez, F. Mayet, L. Perotto, E. Pointecouteau, C. Romero, F. Ruppin, E. Scannapieco, and J. ZuHone, "Astrophysics with the Spatially and Spectrally Resolved Sunyaev-Zeldovich Effects," *Space Sci Rev*, vol. 215, p. 17, Feb. 2019.

[19] S. Nozawa, N. Itoh, and Y. Kohyama, "Relativistic corrections to the Sunyaev-Zeldovich effect for clusters of galaxies: effect of the motion of the observer," *A&A*, vol. 440, pp. 39–44, Sept. 2005.

[20] J. Ruhl, P. A. R. Ade, J. E. Carlstrom, H.-M. Cho, T. Crawford, M. Dobbs, C. H. Greer, N. W. Halverson, W. L. Holzapfel, T. M. Lanting, A. T. Lee, E. M. Leitch, J. Leong, W. Lu, M. Lueker, J. Mehl, S. S. Meyer, J. J. Mohr, S. Padin, T. Plagge, C. Pryke, M. C. Runyan, D. Schwan, M. K. Sharp, H. Spieler, Z. Staniszewski, and A. A. Stark, "The South Pole Telescope," (USA), p. 11, Oct. 2004.

[21] R. J. Thornton, P. A. R. Ade, S. Aiola, F. E. Angilè, M. Amiri, J. A. Beall, D. T. Becker, H.-M. Cho, S. K. Choi, P. Corlies, K. P. Coughlin, R. Datta, M. J. Devlin, S. R. Dicker, R. Dünner, J. W. Fowler, A. E. Fox, P. A. Gallardo, J. Gao, E. Grace, M. Halpern, M. Hasselfield, S. W. Henderson, G. C. Hilton, A. D. Hincks, S. P. Ho, J. Hubmayr, K. D. Irwin, J. Klein, B. Koopman, D. Li, T. Louis, M. Lungu, L. Maurin, J. McMahon, C. D. Munson, S. Naess, F. Nati, L. Newburgh, J. Nibarger, M. D.

Niemack, P. Niraula, M. R. Nolta, L. A. Page, C. G. Pappas, A. Schillaci, B. L. Schmitt, N. Sehgal, J. L. Sievers, S. M. Simon, S. T. Staggs, C. Tucker, M. Uehara, J. V. Lanen, J. T. Ward, and E. J. Wollack, "THE ATACAMA COSMOLOGY TELESCOPE: THE POLARIZATION-SENSITIVE ACTPol INSTRUMENT," *ApJS*, vol. 227, p. 21, Dec. 2016.

[22] L. E. Bleem, B. Stalder, T. d. Haan, K. A. Aird, S. W. Allen, D. E. Applegate, M. L. N. Ashby, M. Bautz, M. Bayliss, B. A. Benson, S. Bocquet, M. Brodwin, J. E. Carlstrom, C. L. Chang, I. Chiu, H. M. Cho, A. Clocchiatti, T. M. Crawford, A. T. Crites, S. Desai, J. P. Dietrich, M. A. Dobbs, R. J. Foley, W. R. Forman, E. M. George, M. D. Gladders, A. H. Gonzalez, N. W. Halverson, C. Hennig, H. Hoekstra, G. P. Holder, W. L. Holzapfel, J. D. Hrubes, C. Jones, R. Keisler, L. Knox, A. T. Lee, E. M. Leitch, J. Liu, M. Lueker, D. Luong-Van, A. Mantz, D. P. Marrone, M. McDonald, J. J. McMahon, S. S. Meyer, L. Mocanu, J. J. Mohr, S. S. Murray, S. Padin, C. Pryke, C. L. Reichardt, A. Rest, J. Ruel, J. E. Ruhl, B. R. Saliwanchik, A. Saro, J. T. Sayre, K. K. Schaffer, T. Schrabback, E. Shirokoff, J. Song, H. G. Spieler, S. A. Stanford, Z. Staniszewski, A. A. Stark, K. T. Story, C. W. Stubbs, K. Vanderlinde, J. D. Vieira, A. Vikhlinin, R. Williamson, O. Zahn, and A. Zenteno, "GALAXY CLUSTERS DISCOVERED VIA THE SUNYAEV–ZEL'DOVICH EFFECT IN THE 2500-SQUARE-DEGREE SPT-SZ SURVEY," *ApJS*, vol. 216, p. 27, Jan. 2015. Publisher: The American Astronomical Society.

[23] L. E. Bleem, M. Klein, T. M. C. Abbott, P. a. R. Ade, M. Aguena, O. Alves, A. J. Anderson, F. Andrade-Oliveira, B. Ansarinejad, M. Archipley, M. L. N. Ashby, J. E. Austermann, D. Bacon, J. A. Beall, A. N. Bender, B. A. Benson, F. Bianchini, S. Bocquet, D. Brooks, D. L. Burke, M. Calzadilla, J. E. Carlstrom, A. C. Rosell, J. Carretero, C. L. Chang, P. Chaubal, H. C. Chiang, T.-L. Chou, R. Citron, C. C. Moran, M. Costanzi, T. M. Crawford, A. T. Crites, L. N. d. Costa, T. d. Haan, J. D. Vicente, S. Desai, M. A. Dobbs, P. Doel, W. Everett, I. Ferrero, B. Flaugher, B. Floyd, D. Friedel, J. Frieman, J. Gallicchio, J. Garc'ia-Bellido, M. Gatti, E. M. George, G. Giannini, S. Grandis, D. Gruen, R. A. Gruendl, N. Gupta, G. Gutierrez, N. W. Halverson, S. R. Hinton, G. P. Holder, D. L. Hollowood, W. L. Holzapfel, K. Honscheid, J. D. Hrubes, N. Huang, J. Hubmayr, K. D. Irwin, J. Mena-Fernández, D. J. James, F. Kéruzoré, L. Knox, K. Kuehn, O. Lahav, A. T. Lee, S. Lee, D. Li, A. Lowitz, J. L. Marshal, M. McDonald, J. J. McMahon, F. Menanteau, S. S. Meyer, R. Miquel, J. J. Mohr, J. Montgomery, J. Myles, T. Natoli, J. P. Nibarger, G. I. Noble, V. Novosad, R. L. C. Ogando, S. Padin, S. Patil, M. E. S. Pereira, A. Pieres, A. A. P. Malag'on, C. Pryke, C. L. Reichardt, M. Rodr'iguez-Monroy, A. K. Romer, J. E. Ruhl, B. R. Saliwanchik, L. Salvati, E. Sanchez, A. Saro, K. K. Schaffer, T. Schrabback, I. Sevilla-Noarbe, C. Sievers, G. Smecher, M. Smith, T. Somboonpanyakul, B. Stalder, A. A. Stark, E. Suchyta, M. E. C. Swanson, G. Tarle, C. To, C. Tucker, T. Veach, J. D. Vieira, M. Vincenzi, G. Wang, J. Weller, N. Whitehorn, P. Wiseman, W. L. K. Wu, V. Yefremenko, J. A. Zebrowski, and Y. Zhang, "Galaxy Clusters Discovered via the Thermal

Sunyaev-Zel'dovich Effect in the 500-square-degree SPTpol Survey," *The Open Journal of Astrophysics*, vol. 7, Feb. 2024. Publisher: Maynooth Academic Publishing.

[24] M. Hilton, C. Sifón, S. Naess, M. Madhavacheril, M. Oguri, E. Rozo, E. Rykoff, T. M. C. Abbott, S. Adhikari, M. Aguena, S. Aiola, S. Allam, S. Amodeo, A. Amon, J. Annis, B. Ansarinejad, C. Aros-Bunster, J. E. Austermann, S. Avila, D. Bacon, N. Battaglia, J. A. Beall, D. T. Becker, G. M. Bernstein, E. Bertin, T. Bhandarkar, S. Bhargava, J. R. Bond, D. Brooks, D. L. Burke, E. Calabrese, M. C. Kind, J. Carretero, S. K. Choi, A. Choi, C. Conselice, L. N. d. Costa, M. Costanzi, D. Crichton, K. T. Crowley, R. Dünner, E. V. Denison, M. J. Devlin, S. R. Dicker, H. T. Diehl, J. P. Dietrich, P. Doel, S. M. Duff, A. J. Duivenvoorden, J. Dunkley, S. Everett, S. Ferraro, I. Ferrero, A. Ferté, B. Flaugher, J. Frieman, P. A. Gallardo, J. García-Bellido, E. Gaztanaga, D. W. Gerdes, P. Giles, J. E. Golec, M. B. Gralla, S. Grandis, D. Gruen, R. A. Gruendl, J. Gschwend, G. Gutierrez, D. Han, W. G. Hartley, M. Hasselfield, J. C. Hill, G. C. Hilton, A. D. Hincks, S. R. Hinton, S.-P. P. Ho, K. Honscheid, B. Hoyle, J. Hubmayr, K. M. Huffenberger, J. P. Hughes, A. T. Jaelani, B. Jain, D. J. James, T. Jeltema, S. Kent, K. Knowles, B. J. Koopman, K. Kuehn, O. Lahav, M. Lima, Y.-T. Lin, M. Lokken, S. I. Loubser, N. MacCrann, M. A. G. Maia, T. A. Marriage, J. Martin, J. McMahon, P. Melchior, F. Menanteau, R. Miquel, H. Miyatake, K. Moodley, R. Morgan, T. Mroczkowski, F. Nati, L. B. Newburgh, M. D. Niemack, A. J. Nishizawa, R. L. C. Ogando, J. Orlowski-Scherer, L. A. Page, A. Palmese, B. Partridge, F. Paz-Chinchón, P. Phakathi, A. A. Plazas, N. C. Robertson, A. K. Romer, A. C. Rosell, M. Salatino, E. Sanchez, E. Schaan, A. Schillaci, N. Sehgal, S. Serrano, T. Shin, S. M. Simon, M. Smith, M. Soares-Santos, D. N. Spergel, S. T. Staggs, E. R. Storer, E. Suchyta, M. E. C. Swanson, G. Tarle, D. Thomas, C. To, H. Trac, J. N. Ullom, L. R. Vale, J. V. Lanen, E. M. Vavagiakis, J. D. Vicente, R. D. Wilkinson, E. J. Wollack, Z. Xu, and Y. Zhang, "The Atacama Cosmology Telescope: A Catalog of >4000 Sunyaev–Zel'dovich Galaxy Clusters," *ApJS*, vol. 253, p. 3, Feb. 2021. Publisher: The American Astronomical Society.

[25] S. Aiola, E. Calabrese, L. Maurin, S. Naess, B. L. Schmitt, M. H. Abitbol, G. E. Addison, P. A. R. Ade, D. Alonso, M. Amiri, S. Amodeo, E. Angile, J. E. Austermann, T. Baildon, N. Battaglia, J. A. Beall, R. Bean, D. T. Becker, J. R. Bond, S. M. Bruno, V. Calafut, L. E. Campusano, F. Carrero, G. E. Chesmore, H.-m. Cho, S. K. Choi, S. E. Clark, N. F. Cothard, D. Crichton, K. T. Crowley, O. Darwish, R. Datta, E. V. Denison, M. J. Devlin, C. J. Duell, S. M. Duff, A. J. Duivenvoorden, J. Dunkley, R. Dünner, T. Essinger-Hileman, M. Fankhanel, S. Ferraro, A. E. Fox, B. Fuzia, P. A. Gallardo, V. Gluscevic, J. E. Golec, E. Grace, M. Gralla, Y. Guan, K. Hall, M. Halpern, D. Han, P. Hargrave, M. Hasselfield, J. M. Helton, S. Henderson, B. Hensley, J. C. Hill, G. C. Hilton, M. Hilton, A. D. Hincks, R. Hložek, S.-P. P. Ho, J. Hubmayr, K. M. Huffenberger, J. P. Hughes, L. Infante, K. Irwin, R. Jackson, J. Klein, K. Knowles, B. Koopman, A. Kosowsky, V. Lakey, D. Li, Y. Li, Z. Li, M. Lokken, T. Louis, M. Lungu, A. MacInnis, M. Madhavacheril, F. Maldonado, M. Mallaby-Kay, D. Marsden, J. McMahon, F. Menanteau, K. Moodley, T. Morton, T. Namikawa, F. Nati,

L. Newburgh, J. P. Nibarger, A. Nicola, M. D. Niemack, M. R. Nolta, J. Orlowski-Sherer, L. A. Page, C. G. Pappas, B. Partridge, P. Phakathi, G. Pisano, H. Prince, R. Puddu, F. J. Qu, J. Rivera, N. Robertson, F. Rojas, M. Salatino, E. Schaan, A. Schillaci, N. Sehgal, B. D. Sherwin, C. Sierra, J. Sievers, C. Sifon, P. Sikhosana, S. Simon, D. N. Spergel, S. T. Staggs, J. Stevens, E. Storer, D. D. Sunder, E. R. Switzer, B. Thorne, R. Thornton, H. Trac, J. Treu, C. Tucker, L. R. Vale, A. V. Engelen, J. V. Lanen, E. M. Vavagiakis, K. Wagoner, Y. Wang, J. T. Ward, E. J. Wollack, Z. Xu, F. Zago, and N. Zhu, "The Atacama Cosmology Telescope: DR4 maps and cosmological parameters," *J. Cosmol. Astropart. Phys.*, vol. 2020, p. 047, Dec. 2020.

[26] M. Arnaud, G. W. Pratt, R. Piffaretti, H. Böhringer, J. H. Croston, and E. Pointecouteau, "The universal galaxy cluster pressure profile from a representative sample of nearby systems (REXCESS) and the $Y_{\rm sz} - M_{500}$ relation," *A&A*, vol. 517, p. A92, July 2010.

[27] N. Aghanim, M. Arnaud, M. Ashdown, J. Aumont, C. Baccigalupi, A. Balbi, A. J. Banday, R. B. Barreiro, M. Bartelmann, J. G. Bartlett, E. Battaner, K. Benabed, A. Benoît, J.-P. Bernard, M. Bersanelli, R. Bhatia, J. J. Bock, A. Bonaldi, J. R. Bond, J. Borrill, F. R. Bouchet, M. L. Brown, M. Bucher, C. Burigana, P. Cabella, J.-F. Cardoso, A. Catalano, L. Cayón, A. Challinor, A. Chamballu, L.-Y. Chiang, C. Chiang, G. Chon, P. R. Christensen, E. Churazov, D. L. Clements, S. Colafrancesco, S. Colombi, F. Couchot, A. Coulais, B. P. Crill, F. Cuttaia, A. D. Silva, H. Dahle, L. Danese, R. J. Davis, P. d. Bernardis, G. d. Gasperis, A. d. Rosa, G. d. Zotti, J. Delabrouille, J.-M. Delouis, F.-X. Désert, J. M. Diego, K. Dolag, S. Donzelli, O. Doré, U. Dörl, M. Douspis, X. Dupac, G. Efstathiou, T. A. Enßlin, F. Finelli, I. Flores-Cacho, O. Forni, M. Frailis, E. Franceschi, S. Fromenteau, S. Galeotta, K. Ganga, R. T. Génova-Santos, M. Giard, G. Giardino, Y. Giraud-Héraud, J. González-Nuevo, K. M. Górski, S. Gratton, A. Gregorio, A. Gruppuso, D. Harrison, S. Henrot-Versillé, C. Hernández-Monteagudo, D. Herranz, S. R. Hildebrandt, E. Hivon, M. Hobson, W. A. Holmes, W. Hovest, R. J. Hoyland, K. M. Huffenberger, A. H. Jaffe, W. C. Jones, M. Juvela, E. Keihänen, R. Keskitalo, T. S. Kisner, R. Kneissl, L. Knox, H. Kurki-Suonio, G. Lagache, J.-M. Lamarre, A. Lasenby, R. J. Laureijs, C. R. Lawrence, S. Leach, R. Leonardi, M. Linden-Vørnle, M. López-Caniego, P. M. Lubin, J. F. Macías-Pérez, C. J. MacTavish, B. Maffei, D. Maino, N. Mandolesi, R. Mann, M. Maris, F. Marleau, E. Martínez-González, S. Masi, S. Matarrese, F. Matthai, P. Mazzotta, S. Mei, A. Melchiorri, J.-B. Melin, L. Mendes, A. Mennella, S. Mitra, M.-A. Miville-Deschênes, A. Moneti, L. Montier, G. Morgante, D. Mortlock, D. Munshi, A. Murphy, P. Naselsky, P. Natoli, C. B. Netterfield, H. U. Nørgaard-Nielsen, F. Noviello, D. Novikov, I. Novikov, I. J. O'Dwyer, S. Osborne, F. Pajot, F. Pasian, G. Patanchon, O. Perdereau, L. Perotto, F. Perrotta, F. Piacentini, M. Piat, E. Pierpaoli, R. Piffaretti, S. Plaszczynski, E. Pointecouteau, G. Polenta, N. Ponthieu, T. Poutanen, G. W. Pratt, G. Prézeau, S. Prunet, J.-L. Puget, R. Rebolo, M. Reinecke, C. Renault, S. Ricciardi, T. Riller, I. Ristorcelli, G. Rocha, C. Rosset, J. A. Rubiño-Martín, B. Rusholme, M. Sandri, G. Savini, B. M. Schaefer, D. Scott, M. D. Seiffert, P. Shellard, G. F. Smoot, J.-L. Starck, F. Stivoli, V. Stol-

yarov, R. Sudiwala, R. Sunyaev, J.-F. Sygnet, J. A. Tauber, L. Terenzi, L. Toffolatti, M. Tomasi, J.-P. Torre, M. Tristram, J. Tuovinen, L. Valenziano, L. Vibert, P. Vielva, F. Villa, N. Vittorio, B. D. Wandelt, S. D. M. White, M. White, D. Yvon, A. Zacchei, and A. Zonca, "Planck early results. XII. Cluster Sunyaev-Zeldovich optical scaling relations," *A&A*, vol. 536, p. A12, Dec. 2011. Publisher: EDP Sciences.

[28] J. P. Dietrich, S. Bocquet, T. Schrabback, D. Applegate, H. Hoekstra, S. Grandis, J. J. Mohr, S. W. Allen, M. B. Bayliss, B. A. Benson, L. E. Bleem, M. Brodwin, E. Bulbul, R. Capasso, I. Chiu, T. M. Crawford, A. H. Gonzalez, T. de Haan, M. Klein, A. von der Linden, A. B. Mantz, D. P. Marrone, M. McDonald, S. Raghunathan, D. Rapetti, C. L. Reichardt, A. Saro, B. Stalder, A. Stark, C. Stern, and C. Stubbs, "Sunyaev–Zel'dovich effect and X-ray scaling relations from weak lensing mass calibration of 32 South Pole Telescope selected galaxy clusters," *Monthly Notices of the Royal Astronomical Society*, vol. 483, pp. 2871–2906, Mar. 2019.

[29] S. Bocquet, A. Saro, K. Dolag, and J. J. Mohr, "Halo mass function: baryon impact, fitting formulae, and implications for cluster cosmology," *Mon. Not. R. Astron. Soc.*, vol. 456, pp. 2361–2373, Mar. 2016.

[30] S. Bocquet, S. Grandis, L. E. Bleem, M. Klein, J. J. Mohr, T. Schrabback, T. M. C. Abbott, P. A. R. Ade, M. Aguena, A. Alarcon, S. Allam, S. W. Allen, O. Alves, A. Amon, A. J. Anderson, J. Annis, B. Ansarinejad, J. E. Austermann, S. Avila, D. Bacon, M. Bayliss, J. A. Beall, K. Bechtol, M. R. Becker, A. N. Bender, B. A. Benson, G. M. Bernstein, S. Bhargava, F. Bianchini, M. Brodwin, D. Brooks, L. Bryant, A. Campos, R. E. A. Canning, J. E. Carlstrom, A. C. Rosell, M. C. Kind, J. Carretero, F. J. Castander, R. Cawthon, C. L. Chang, C. Chang, P. Chaubal, R. Chen, H. C. Chiang, A. Choi, T.-L. Chou, R. Citron, C. C. Moran, J. Cordero, M. Costanzi, T. M. Crawford, A. T. Crites, L. N. da Costa, M. E. S. Pereira, C. Davis, T. M. Davis, J. DeRose, S. Desai, T. de Haan, H. T. Diehl, M. A. Dobbs, S. Dodelson, C. Doux, A. Drlica-Wagner, K. Eckert, J. Elvin-Poole, S. Everett, W. Everett, I. Ferrero, A. Ferté, A. M. Flores, J. Frieman, J. Gallicchio, J. García-Bellido, M. Gatti, E. M. George, G. Giannini, M. D. Gladders, D. Gruen, R. A. Gruendl, N. Gupta, G. Gutierrez, N. W. Halverson, I. Harrison, W. G. Hartley, K. Herner, S. R. Hinton, G. P. Holder, D. L. Hollowood, W. L. Holzapfel, K. Honscheid, J. D. Hrubes, N. Huang, J. Hubmayr, E. M. Huff, D. Huterer, K. D. Irwin, D. J. James, M. Jarvis, G. Khullar, K. Kim, L. Knox, R. Kraft, E. Krause, K. Kuehn, N. Kuropatkin, F. Kéruzoré, O. Lahav, A. T. Lee, P. F. Leget, D. Li, H. Lin, A. Lowitz, N. MacCrann, G. Mahler, A. Mantz, J. L. Marshall, J. McCullough, M. McDonald, J. J. McMahon, J. Mena-Fernández, F. Menanteau, S. S. Meyer, R. Miquel, J. Montgomery, J. Myles, T. Natoli, A. Navarro-Alsina, J. P. Nibarger, G. I. Noble, V. Novosad, R. L. C. Ogando, Y. Omori, S. Padin, S. Pandey, P. Paschos, S. Patil, A. Pieres, A. A. P. Malagón, A. Porredon, J. Prat, C. Pryke, M. Raveri, C. L. Reichardt, J. Roberson, R. P. Rollins, C. Romero, A. Roodman, J. E. Ruhl, E. S. Rykoff, B. R. Saliwanchik, L. Salvati, C. Sánchez, E. Sanchez, D. S. Cid, A. Saro, K. K. Schaffer, L. F. Secco, I. Sevilla-Noarbe, K. Sharon, E. Sheldon, T. Shin, C. Sievers, G. Smecher, M. Smith, T. Somboonpanyakul, M. Sommer, B. Stalder, A. A.

Stark, J. Stephen, V. Strazzullo, E. Suchyta, G. Tarle, C. To, M. A. Troxel, C. Tucker, I. Tutusaus, T. N. Varga, T. Veach, J. D. Vieira, A. Vikhlinin, A. von der Linden, G. Wang, N. Weaverdyck, J. Weller, N. Whitehorn, W. L. K. Wu, B. Yanny, V. Yefremenko, B. Yin, M. Young, J. A. Zebrowski, Y. Zhang, H. Zohren, and J. Zuntz, "SPT Clusters with DES and HST Weak Lensing. II. Cosmological Constraints from the Abundance of Massive Halos," 2024. Publisher: [object Object] Version Number: 1.

[31] V. Poulin, J. L. Bernal, E. D. Kovetz, and M. Kamionkowski, "Sigma-8 tension is a drag," *Phys. Rev. D*, vol. 107, p. 123538, June 2023. Publisher: American Physical Society.

[32] S. R. Dicker, P. A. R. Ade, J. Aguirre, J. A. Brevik, H. M. Cho, R. Datta, M. J. Devlin, B. Dober, D. Egan, J. Ford, P. Ford, G. Hilton, K. D. Irwin, B. S. Mason, P. Marganian, M. Mello, J. J. McMahon, T. Mroczkowski, M. Rosenman, C. Tucker, L. Vale, S. White, M. Whitehead, and A. H. Young, "MUSTANG 2: A Large Focal Plane Array for the 100 m Green Bank Telescope," *J Low Temp Phys*, vol. 176, pp. 808–814, Sept. 2014.

[33] J. Glenn, P. A. R. Ade, M. Amarie, J. J. Bock, S. F. Edgington, A. Goldin, S. Golwala, D. Haig, A. E. Lange, G. Laurent, P. D. Mauskopf, M. Yun, and H. Nguyen, "Current status of Bolocam: a large-format millimeter-wave bolometer camera," (Waikoloa, Hawai'i, United States), p. 30, Feb. 2003.

[34] B. A. Benson, S. E. Church, P. a. R. Ade, J. J. Bock, K. M. Ganga, C. N. Henson, and K. L. Thompson, "Measurements of Sunyaev-Zel'dovich Effect Scaling Relations for Clusters of Galaxies," *ApJ*, vol. 617, p. 829, Dec. 2004. Publisher: IOP Publishing.

[35] P. D. Mauskopf, P. F. Horner, J. Aguirre, J. J. Bock, E. Egami, J. Glenn, S. R. Golwala, G. Laurent, H. T. Nguyen, and J. Sayers, "A high signal-to-noise ratio map of the Sunyaev–Zel'dovich increment at 1.1-mm wavelength in Abell 1835," *Monthly Notices of the Royal Astronomical Society*, vol. 421, pp. 224–234, Mar. 2012.

[36] C. E. Romero, B. S. Mason, J. Sayers, T. Mroczkowski, C. Sarazin, M. Donahue, A. Baldi, T. E. Clarke, A. H. Young, J. Sievers, S. R. Dicker, E. D. Reese, N. Czakon, M. Devlin, P. M. Korngut, and S. Golwala, "Galaxy Cluster Pressure Profiles as Determined by Sunyaev Zel'dovich Effect Observations with MUSTANG and Bolocam. II. Joint Analysis of 14 Clusters," *ApJ*, vol. 838, p. 86, Mar. 2017. Publisher: The American Astronomical Society.

[37] S. R. Dicker, E. S. Battistelli, T. Bhandarkar, M. J. Devlin, S. M. Duff, G. Hilton, M. Hilton, A. D. Hincks, J. Hubmayr, K. Huffenberger, J. P. Hughes, L. Di Mascolo, B. S. Mason, J. A. B. Mates, J. McMahon, T. Mroczkowski, S. Naess, J. Orlowski-Scherer, B. Partridge, F. Radiconi, C. Romero, C. L. Sarazin, N. Sehgal, J. Sievers, C. Sifón, J. Ullom, L. R. Vale, M. R. Vissers, and Z. Xu, "Observations of compact sources in galaxy clusters using MUSTANG2," *Monthly Notices of the Royal Astronomical Society*, vol. 508, pp. 2600–2612, Dec. 2021.

[38] J. Hlavacek-Larrondo, M. McDonald, B. A. Benson, W. R. Forman, S. W. Allen, L. E. Bleem, M. L. N. Ashby, S. Bocquet, M. Brodwin, J. P. Dietrich, C. Jones, J. Liu, C. L. Reichardt, B. R. Saliwanchik, A. Saro, T. Schrabback, J. Song, B. Stalder, A. Vikhlinin, and A. Zenteno, "X-RAY CAVITIES IN A SAMPLE OF 83 SPT-SELECTED CLUSTERS OF GALAXIES: TRACING THE EVOLUTION OF AGN FEEDBACK IN CLUSTERS OF GALAXIES OUT TO z = 1.2," *ApJ*, vol. 805, p. 35, May 2015. Publisher: The American Astronomical Society.

[39] H. Akamatsu, M. Takizawa, K. Nakazawa, Y. Fukazawa, Y. Ishisaki, and T. Ohashi, "X-Ray View of the Shock Front in the Merging Cluster Abell 3376 with Suzaku," *Publications of the Astronomical Society of Japan*, vol. 64, p. 67, Aug. 2012.

[40] D. Clowe, M. Bradač, A. H. Gonzalez, M. Markevitch, S. W. Randall, C. Jones, and D. Zaritsky, "A Direct Empirical Proof of the Existence of Dark Matter*," *ApJ*, vol. 648, p. L109, Aug. 2006. Publisher: IOP Publishing.

[41] S. M. Molnar, N. Hearn, Z. Haiman, G. Bryan, A. E. Evrard, and G. Lake, "ACCRETION SHOCKS IN CLUSTERS OF GALAXIES AND THEIR SZ SIGNATURE FROM COSMOLOGICAL SIMULATIONS," *ApJ*, vol. 696, p. 1640, Apr. 2009. Publisher: The American Astronomical Society.

[42] M. Calvo, A. Benoît, A. Catalano, J. Goupy, A. Monfardini, N. Ponthieu, E. Barria, G. Bres, M. Grollier, G. Garde, J.-P. Leggeri, G. Pont, S. Triqueneaux, R. Adam, O. Bourrion, J.-F. Macías-Pérez, M. Rebolo, A. Ritacco, J.-P. Scordilis, D. Tourres, A. Adane, G. Coiffard, S. Leclercq, F.-X. Désert, S. Doyle, P. Mauskopf, C. Tucker, P. Ade, P. André, A. Beelen, B. Belier, A. Bideaud, N. Billot, B. Comis, A. D'Addabbo, C. Kramer, J. Martino, F. Mayet, F. Pajot, E. Pascale, L. Perotto, V. Revéret, A. Ritacco, L. Rodriguez, G. Savini, K. Schuster, A. Sievers, and R. Zylka, "The NIKA2 Instrument, A Dual-Band Kilopixel KID Array for Millimetric Astronomy," *J Low Temp Phys*, vol. 184, pp. 816–823, Aug. 2016.

[43] R. Adam, I. Bartalucci, G. W. Pratt, P. Ade, P. André, M. Arnaud, A. Beelen, A. Benoît, A. Bideaud, N. Billot, H. Bourdin, O. Bourrion, M. Calvo, A. Catalano, G. Coiffard, B. Comis, A. D'Addabbo, M. D. Petris, J. Démoclès, F.-X. Désert, S. Doyle, E. Egami, C. Ferrari, J. Goupy, C. Kramer, G. Lagache, S. Leclercq, J.-F. Macías-Pérez, S. Maurogordato, P. Mauskopf, F. Mayet, A. Monfardini, T. Mroczkowski, F. Pajot, E. Pascale, L. Perotto, G. Pisano, E. Pointecouteau, N. Ponthieu, V. Revéret, A. Ritacco, L. Rodriguez, C. Romero, F. Ruppin, K. Schuster, A. Sievers, S. Triqueneaux, C. Tucker, M. Zemcov, and R. Zylka, "Mapping the kinetic Sunyaev-Zel'dovich effect toward MACS J0717.5+3745 with NIKA," *A&A*, vol. 598, p. A115, Feb. 2017. Publisher: EDP Sciences.

[44] J. Orlowski-Scherer, S. K. Haridas, L. D. Mascolo, K. P. Sarmiento, C. E. Romero, S. Dicker, T. Mroczkowski, T. Bhandarkar, E. Churazov, T. E. Clarke, M. Devlin, M. Gaspari, I. Lowe, B. Mason, C. L. Sarazin, J. Sievers, and R. Sunyaev,

"GBT/MUSTANG-2 9 resolution imaging of the SZ effect in MS0735.6+7421 - Confirmation of the SZ cavities through direct imaging," *A&A*, vol. 667, p. L6, Nov. 2022. Publisher: EDP Sciences.

[45] B. R. McNamara, P. E. J. Nulsen, M. W. Wise, D. A. Rafferty, C. Carilli, C. L. Sarazin, and E. L. Blanton, "The heating of gas in a galaxy cluster by X-ray cavities and large-scale shock fronts," *Nature*, vol. 433, pp. 45–47, Jan. 2005. Publisher: Nature Publishing Group.

[46] J. R. Peterson and A. C. Fabian, "X-ray spectroscopy of cooling clusters," *Physics Reports*, vol. 427, pp. 1–39, Apr. 2006.

[47] E. Churazov, A. Vikhlinin, I. Zhuravleva, A. Schekochihin, I. Parrish, R. Sunyaev, W. Forman, H. Böhringer, and S. Randall, "X-ray surface brightness and gas density fluctuations in the Coma cluster," *Monthly Notices of the Royal Astronomical Society*, vol. 421, pp. 1123–1135, Apr. 2012.

[48] R. Khatri and M. Gaspari, "Thermal SZ fluctuations in the ICM: probing turbulence and thermodynamics in Coma cluster with Planck," *Monthly Notices of the Royal Astronomical Society*, vol. 463, pp. 655–669, Nov. 2016.

[49] C. E. Romero, J. Sievers, V. Ghirardini, S. Dicker, S. Giacintucci, T. Mroczkowski, B. S. Mason, C. Sarazin, M. Devlin, M. Gaspari, N. Battaglia, M. Hilton, E. Bulbul, I. Lowe, and S. Stanchfield, "Pressure Profiles and Mass Estimates Using High-resolution Sunyaev–Zel'dovich Effect Observations of Zwicky 3146 with MUSTANG-2," *ApJ*, vol. 891, p. 90, Mar. 2020. Publisher: The American Astronomical Society.

[50] C. E. Romero, M. Gaspari, G. Schellenberger, T. Bhandarkar, M. Devlin, S. R. Dicker, W. Forman, R. Khatri, R. Kraft, L. D. Mascolo, B. S. Mason, E. Moravec, T. Mroczkowski, P. Nulsen, J. Orlowski-Scherer, K. P. Sarmiento, C. Sarazin, J. Sievers, and Y. Su, "Inferences from Surface Brightness Fluctuations of Zwicky 3146 via the Sunyaev–Zel'dovich Effect and X-Ray Observations," *ApJ*, vol. 951, p. 41, July 2023. Publisher: The American Astronomical Society.

[51] N. Galitzki, T. Baildon, D. Barron, J. Lashner, A. T. Lee, Y. Li, M. Limon, M. Lungu, F. Matsuda, P. D. Mauskopf, A. J. May, N. McCallum, J. McMahon, F. Nati, M. D. Niemack, J. L. Orlowski-Scherer, S. C. Parshley, L. Piccirillo, M. S. Rao, M. Salatino, J. S. Seibert, C. Sierra, M. Silva-Feaver, S. M. Simon, S. T. Staggs, J. R. Stevens, A. Suzuki, G. Teply, R. Thornton, C. Tsai, J. N. Ullom, E. M. Vavagiakis, M. R. Vissers, B. Westbrook, E. J. Wollack, Z. Xu, N. Zhu, C. Raum, S. Beckman, O. Jeong, A. Ali, K. S. Arnold, P. C. Ashton, J. E. Austermann, C. Baccigalupi, J. A. Beall, S. M. M. Bruno, S. Bryan, P. G. Calisse, G. E. Chesmore, Y. Chinone, S. K. Choi, G. Coppi, K. D. Crowley, K. T. Crowley, A. Cukierman, M. J. Devlin, S. Dicker, B. Dober, S. M. Duff, J. Dunkley, G. Fabbian, P. A. Gallardo, M. Gerbino, N. Goeckner-Wald, J. E. Golec, J. Gudmundsson, E. E. Healy, S. Henderson, C. A. Hill, G. C. Hilton, S.-P. P. Ho, L. A. Howe, J. Hubmayr, B. Keating, B. J. Koopman, K. Kuichi, and A. Kusaka,

"The Simons Observatory: instrument overview," in *Millimeter, Submillimeter, and Far-Infrared Detectors and Instrumentation for Astronomy IX* (J. Zmuidzinas and J.-R. Gao, eds.), (Austin, United States), p. 3, SPIE, July 2018.

[52] G. W. Wilson, S. Abi-saad, P. Ade, I. Aretxaga, J. E. Austermann, Y. Ban, J. Bardin, J. A. Beall, M. Berthoud, S. A. Bryan, J. Bussan, E. Castillo-Domínguez, M. Chavez, R. Contente, N. W. DeNigris, B. Dober, M. Eiben, D. Ferrusca, L. Fissel, J. Gao, J. Golec, R. Golina, A. Gomez, S. Gordon, R. Gutermuth, G. Hilton, M. Hosseini, J. Hubmayr, D. Hughes, S. W. Kuczarski, D. Lee, E. Lunde, Z. Ma, H. Mani, P. Mauskopf, M. McCrackan, C. McKenney, J. McMahon, G. Novak, G. Pisano, A. Pope, A. Ralston, I. Rodriguez, D. Sánchez-Argüelles, F. P. Schloerb, S. M. Simon, A. Sinclair, K. Souccar, A. Torres Campos, C. Tucker, J. Ullom, E. Van Camp, J. Van Lanen, M. Velazquez, M. Vissers, E. Weeks, and M. S. Yun, "The TolTEC camera: an overview of the instrument and in-lab testing results," in *Millimeter, Submillimeter, and Far-Infrared Detectors and Instrumentation for Astronomy X* (J. Zmuidzinas and J.-R. Gao, eds.), (Online Only, United States), p. 1, SPIE, Dec. 2020.

[53] S. R. Dicker, P. A. Gallardo, J. E. Gudmundsson, P. D. Mauskopf, A. Ali, P. C. Ashton, G. Coppi, M. J. Devlin, N. Galitzki, S. P. Ho, C. A. Hill, J. Hubmayr, B. Keating, A. T. Lee, M. Limon, F. Matsuda, J. McMahon, M. D. Niemack, J. L. Orlowski-Scherer, L. Piccirillo, M. Salatino, S. M. Simon, S. T. Staggs, R. Thornton, J. N. Ullom, E. M. Vavagiakis, E. J. Wollack, Z. Xu, and N. Zhu, "Cold optical design for the Large Aperture Simons Observatory telescope," 2018. Publisher: [object Object] Version Number: 2.

[54] P. Ade, J. Aguirre, Z. Ahmed, S. Aiola, A. Ali, D. Alonso, M. A. Alvarez, K. Arnold, P. Ashton, J. Austermann, H. Awan, C. Baccigalupi, T. Baildon, D. Barron, N. Battaglia, R. Battye, E. Baxter, A. Bazarko, J. A. Beall, R. Bean, D. Beck, S. Beckman, B. Beringue, F. Bianchini, S. Boada, D. Boettger, J. R. Bond, J. Borrill, M. L. Brown, S. M. Bruno, S. Bryan, E. Calabrese, V. Calafut, P. Calisse, J. Carron, A. Challinor, G. Chesmore, Y. Chinone, J. Chluba, H.-M. S. Cho, S. Choi, G. Coppi, N. F. Cothard, K. Coughlin, D. Crichton, K. D. Crowley, K. T. Crowley, A. Cukierman, J. M. D'Ewart, R. Dünner, T. d. Haan, M. Devlin, S. Dicker, J. Didier, M. Dobbs, B. Dober, C. J. Duell, S. Duff, A. Duivenvoorden, J. Dunkley, J. Dusatko, J. Errard, G. Fabbian, S. Feeney, S. Ferraro, P. Fluxà, K. Freese, J. C. Frisch, A. Frolov, G. Fuller, B. Fuzia, N. Galitzki, P. A. Gallardo, J. T. G. Ghersi, J. Gao, E. Gawiser, M. Gerbino, V. Gluscevic, N. Goeckner-Wald, J. Golec, S. Gordon, M. Gralla, D. Green, A. Grigorian, J. Groh, C. Groppi, Y. Guan, J. E. Gudmundsson, D. Han, P. Hargrave, M. Hasegawa, M. Hasselfield, M. Hattori, V. Haynes, M. Hazumi, Y. He, E. Healy, S. W. Henderson, C. Hervias-Caimapo, C. A. Hill, J. C. Hill, G. Hilton, M. Hilton, A. D. Hincks, G. Hinshaw, R. Hložek, S. Ho, S.-P. P. Ho, L. Howe, Z. Huang, J. Hubmayr, K. Huffenberger, J. P. Hughes, A. Ijjas, M. Ikape, K. Irwin, A. H. Jaffe, B. Jain, O. Jeong, D. Kaneko, E. D. Karpel, N. Katayama, B. Keating, S. S. Kernasovskiy, R. Keskitalo, T. Kisner, K. Kiuchi, J. Klein, K. Knowles, B. Koopman, A. Kosowsky, N. Krachmalnicoff, S. E. Kuenstner, C.-L. Kuo, A. Kusaka, J. Lashner,

A. Lee, E. Lee, D. Leon, J. S.-Y. Leung, A. Lewis, Y. Li, Z. Li, M. Limon, E. Linder, C. Lopez-Caraballo, T. Louis, L. Lowry, M. Lungu, M. Madhavacheril, D. Mak, F. Maldonado, H. Mani, B. Mates, F. Matsuda, L. Maurin, P. Mauskopf, A. May, N. McCallum, C. McKenney, J. McMahon, P. D. Meerburg, J. Meyers, A. Miller, M. Mirmelstein, K. Moodley, M. Munchmeyer, C. Munson, S. Naess, F. Nati, M. Navaroli, L. Newburgh, H. N. Nguyen, M. Niemack, H. Nishino, J. Orlowski-Scherer, L. Page, B. Partridge, J. Peloton, F. Perrotta, L. Piccirillo, G. Pisano, D. Poletti, R. Puddu, G. Puglisi, C. Raum, C. L. Reichardt, M. Remazeilles, Y. Rephaeli, D. Riechers, F. Rojas, A. Roy, S. Sadeh, Y. Sakurai, M. Salatino, M. S. Rao, E. Schaan, M. Schmittfull, N. Sehgal, J. Seibert, U. Seljak, B. Sherwin, M. Shimon, C. Sierra, J. Sievers, P. Sikhosana, M. Silva-Feaver, S. M. Simon, A. Sinclair, P. Siritanasak, K. Smith, S. R. Smith, D. Spergel, S. T. Staggs, G. Stein, J. R. Stevens, R. Stompor, A. Suzuki, O. Tajima, S. Takakura, G. Teply, D. B. Thomas, B. Thorne, R. Thornton, H. Trac, C. Tsai, C. Tucker, J. Ullom, S. Vagnozzi, A. v. Engelen, J. V. Lanen, D. D. V. Winkle, E. M. Vavagiakis, C. Vergès, M. Vissers, K. Wagoner, S. Walker, J. Ward, B. Westbrook, N. Whitehorn, J. Williams, J. Williams, E. J. Wollack, Z. Xu, B. Yu, C. Yu, F. Zago, H. Zhang, N. Zhu, and T. S. O. collaboration, "The Simons Observatory: science goals and forecasts," *J. Cosmol. Astropart. Phys.*, vol. 2019, p. 056, Feb. 2019.

[55] S. Paine, "The am atmospheric model," Sept. 2023. Publisher: [object Object] Version Number: 13.0.

[56] M. D. Niemack, "Designs for a large-aperture telescope to map the CMB 10× faster," *Appl. Opt., AO*, vol. 55, pp. 1688–1696, Mar. 2016. Publisher: Optica Publishing Group.

[57] S. C. Parshley, M. D. Niemack, R. Hills, S. R. Dicker, R. Dunner, J. Erler, P. A. Gallardo, J. E. Gudmundsson, T. Herter, B. J. Koopman, M. Limon, F. T. Matsuda, P. Mauskopf, D. A. Riechers, G. J. Stacey, and E. M. Vavagiakis, "The optical design of the six-meter CCAT-prime and Simons Observatory telescopes," in *Ground-based and Airborne Telescopes VII* (R. Gilmozzi, H. K. Marshall, and J. Spyromilio, eds.), (Austin, United States), p. 145, SPIE, July 2018.

[58] J. E. Gudmundsson, P. A. Gallardo, R. Puddu, S. R. Dicker, A. E. Adler, A. M. Ali, A. Bazarko, G. E. Chesmore, G. Coppi, N. F. Cothard, N. Dachlythra, M. Devlin, R. Dünner, G. Fabbian, N. Galitzki, J. E. Golec, S.-P. P. Ho, P. C. Hargrave, A. M. Kofman, A. T. Lee, M. Limon, F. T. Matsuda, P. D. Mauskopf, K. Moodley, F. Nati, M. D. Niemack, J. Orlowski-Scherer, L. A. Page, B. Partridge, G. Puglisi, C. L. Reichardt, C. E. Sierra, S. M. Simon, G. P. Teply, C. Tucker, E. J. Wollack, Z. Xu, and N. Zhu, "The Simons Observatory: modeling optical systematics in the Large Aperture Telescope," *Appl. Opt., AO*, vol. 60, pp. 823–837, Feb. 2021. Publisher: Optica Publishing Group.

[59] N. Zhu, T. Bhandarkar, G. Coppi, A. M. Kofman, J. L. Orlowski-Scherer, Z. Xu, S. Adachi, P. Ade, S. Aiola, J. Austermann, A. O. Bazarko, J. A. Beall, S. Bhimani,

J. R. Bond, G. E. Chesmore, S. K. Choi, J. Connors, N. F. Cothard, M. Devlin, S. Dicker, B. Dober, C. J. Duell, S. M. Duff, R. Dünner, G. Fabbian, N. Galitzki, P. A. Gallardo, J. E. Golec, S. K. Haridas, K. Harrington, E. Healy, S.-P. P. Ho, Z. B. Huber, J. Hubmayr, J. Iuliano, B. R. Johnson, B. Keating, K. Kiuchi, B. J. Koopman, J. Lashner, A. T. Lee, Y. Li, M. Limon, M. Link, T. J. Lucas, H. McCarrick, J. Moore, F. Nati, L. B. Newburgh, M. D. Niemack, E. Pierpaoli, M. J. Randall, K. P. Sarmiento, L. J. Saunders, J. Seibert, C. Sierra, R. Sonka, J. Spisak, S. Sutariya, O. Tajima, G. P. Teply, R. J. Thornton, T. Tsan, C. Tucker, J. Ullom, E. M. Vavagiakis, M. R. Vissers, S. Walker, B. Westbrook, E. J. Wollack, and M. Zannoni, "The Simons Observatory Large Aperture Telescope Receiver," *ApJS*, vol. 256, p. 23, Sept. 2021. Publisher: The American Astronomical Society.

[60] P. A. R. Ade, G. Pisano, C. Tucker, and S. Weaver, "A review of metal mesh filters," (Orlando, Florida , USA), p. 62750U, June 2006.

[61] Y. Inoue, *The thermal design of the POLARBEAR-2 experiment*. PhD thesis, Graduate University for Advanced Studies, Shonankokusaimura, Hayama, Miura District, Kanagawa 240-0193, Japan, 2013.

[62] J. E. Golec, S. Sutariya, R. Jackson, J. Zimmerman, S. R. Dicker, J. Iuliano, J. McMahon, G. Puglisi, C. Tucker, and E. J. Wollack, "Simons Observatory: broadband metamaterial antireflection cuttings for large-aperture alumina optics," *Appl. Opt., AO*, vol. 61, pp. 8904–8911, Oct. 2022. Publisher: Optica Publishing Group.

[63] Z. Xu, G. E. Chesmore, S. Adachi, A. M. Ali, A. Bazarko, G. Coppi, M. Devlin, T. Devlin, S. R. Dicker, P. A. Gallardo, J. E. Golec, J. E. Gudmundsson, K. Harrington, M. Hattori, A. Kofman, K. Kiuchi, A. Kusaka, M. Limon, F. Matsuda, J. McMahon, F. Nati, M. D. Niemack, A. Suzuki, G. P. Teply, R. J. Thornton, E. J. Wollack, M. Zannoni, and N. Zhu, "The Simons Observatory: metamaterial microwave absorber and its cryogenic applications," *Appl. Opt., AO*, vol. 60, pp. 864–874, Feb. 2021. Publisher: Optica Publishing Group.

[64] R. Datta, C. D. Munson, M. D. Niemack, J. J. McMahon, J. Britton, E. J. Wollack, J. Beall, M. J. Devlin, J. Fowler, P. Gallardo, J. Hubmayr, K. Irwin, L. Newburgh, J. P. Nibarger, L. Page, M. A. Quijada, B. L. Schmitt, S. T. Staggs, R. Thornton, and L. Zhang, "Large-aperture wide-bandwidth antireflection-coated silicon lenses for millimeter wavelengths," *Appl. Opt., AO*, vol. 52, pp. 8747–8758, Dec. 2013. Publisher: Optica Publishing Group.

[65] J. E. Golec, J. J. McMahon, A. Ali, G. Chesmore, L. Cooperrider, S. Dicker, N. Galitzki, K. Harrington, R. Jackson, B. Westbrook, E. J. Wollack, Z. Xu, and N. Zhu, "Design and fabrication of metamaterial anti-reflection coatings for the Simons Observatory," in *Advances in Optical and Mechanical Technologies for Telescopes and Instrumentation IV* (R. Geyl and R. Navarro, eds.), (Online Only, United States), p. 199, SPIE, Dec. 2020.

[66] H. McCarrick, K. Arnold, Z. Atkins, J. Austermann, T. Bhandarkar, S. K. Choi, C. J. Duell, S. M. Duff, D. Dutcher, N. Galitzk, E. Healy, Z. B. Huber, J. Hubmayr, B. R. Johnson, M. D. Niemack, J. Seibert, M. Silva-Feaver, R. F. Sonka, S. T. Staggs, E. M. Vavagiakis, Y. Wang, Z. Xu, K. Zheng, and N. Zhu, "The 90 and 150 GHz universal focal-plane modules for the Simons Observatory," 2021. Publisher: [object Object] Version Number: 1.

[67] E. Healy, D. Dutcher, Z. Atkins, J. Austermann, S. K. Choi, C. J. Duell, S. Duff, N. Galitzki, Z. B. Huber, J. Hubmayr, B. R. Johnson, H. McCarrick, M. D. Niemack, R. Sonka, S. T. Staggs, E. Vavagiakis, Y. Wang, Z. Xu, and K. Zheng, "The Simons Observatory 220 and 280 GHz Focal-Plane Module: Design and Initial Characterization," *J Low Temp Phys*, vol. 209, pp. 815–823, Dec. 2022.

[68] K. W. Yoon, J. W. Appel, J. E. Austermann, J. A. Beall, D. Becker, B. A. Benson, L. E. Bleem, J. Britton, C. L. Chang, J. E. Carlstrom, H. Cho, A. T. Crites, T. Essinger-Hileman, W. Everett, N. W. Halverson, J. W. Henning, G. C. Hilton, K. D. Irwin, J. McMahon, J. Mehl, S. S. Meyer, S. Moseley, M. D. Niemack, L. P. Parker, S. M. Simon, S. T. Staggs, K. U-yen, C. Visnjic, E. Wollack, and Y. Zhao, "Feedhorn-Coupled TES Polarimeters for Next-Generation CMB Instruments," *AIP Conference Proceedings*, vol. 1185, pp. 515–518, Dec. 2009.

[69] S. M. Simon, J. E. Golec, A. Ali, J. Austermann, J. A. Beall, S. M. M. Bruno, S. K. Choi, K. T. Crowley, S. Dicker, B. Dober, S. M. Duff, E. Healy, C. A. Hill, S.-P. P. Ho, J. Hubmayr, Y. Li, M. Lungu, J. McMahon, J. Orlowski-Scherer, M. Salatino, S. Staggs, E. J. Wollack, Z. Xu, and N. Zhu, "Feedhorn development and scalability for Simons Observatory and beyond," in *Millimeter, Submillimeter, and Far-Infrared Detectors and Instrumentation for Astronomy IX* (J. Zmuidzinas and J.-R. Gao, eds.), (Austin, United States), p. 147, SPIE, July 2018.

[70] R. Datta, J. Hubmayr, C. Munson, J. Austermann, J. Beall, D. Becker, H. M. Cho, N. Halverson, G. Hilton, K. Irwin, D. Li, J. McMahon, L. Newburgh, J. Nibarger, M. Niemack, B. Schmitt, H. Smith, S. Staggs, J. Van Lanen, and E. Wollack, "Horn Coupled Multichroic Polarimeters for the Atacama Cosmology Telescope Polarization Experiment," *J Low Temp Phys*, vol. 176, pp. 670–676, Sept. 2014.

[71] K. Irwin and G. Hilton, "Transition-Edge Sensors," in *Cryogenic Particle Detection* (C. E. Ascheron, H. J. Kölsch, W. Skolaut, and C. Enss, eds.), vol. 99, pp. 63–150, Berlin, Heidelberg: Springer Berlin Heidelberg, July 2005. Series Title: Topics in Applied Physics.

[72] A. T. Lee, S. Cho, J. M. Gildemeister, N. Halverson, W. L. Holzapfel, J. Mehl, M. J. Myers, T. Lanting, P. L. Richards, E. Rittweger, D. Schwan, H. Spieler, and H. Tran, "Voltage-biased TES bolometers for the far-infrared to millimeter wavelength range," (Waikoloa, Hawai'i, United States), p. 129, Feb. 2003.

[73] C. Yu, Z. Ahmed, J. A. Connors, J. M. D'Ewart, B. Dober, J. C. Frisch, S. W. Henderson, G. C. Hilton, J. Hubmayr, S. E. Kuenstner, J. A. B. Mates, M. Silva-Feaver, J. N. Ullom, L. R. Vale, D. V. Winkle, and E. Young, "Bandwidth and Aliasing in the Microwave SQUID Multiplexer," *J Low Temp Phys*, vol. 209, pp. 589–597, Nov. 2022.

[74] S. A. Bryan, J. E. Austermann, P. Mauskopf, G. Novak, S. M. Simon, G. W. Wilson, J. McMahon, D. Ferrusca, A. Montana, and D. Sanchez-Arguelles, "Optical design of the TolTEC millimeter-wave camera," in *Millimeter, Submillimeter, and Far-Infrared Detectors and Instrumentation for Astronomy IX* (J. Zmuidzinas and J.-R. Gao, eds.), (Austin, United States), p. 17, SPIE, July 2018.

[75] D. H. Hughes, F. P. Schloerb, I. Aretxaga, E. Castillo-Dominguez, M. Chávez Dagostino, E. Colín, N. Erickson, D. Ferrusca Rodriguez, D. M. Gale, A. Gómez-Ruiz, J. L. Hernández Rebollar, M. Heyer, J. D. Lowenthal, A. Montaña, M. E. Moreno Nolasco, G. Narayanan, A. Pope, I. Rodríguez-Montoya, D. Sánchez-Argüelles, D. R. Smith, K. Souccar, M. V. De La Rosa Becerra, G. W. Wilson, and M. S. Yun, "The Large Millimeter Telescope (LMT) Alfonso Serrano: current status and telescope performance," in *Ground-based and Airborne Telescopes VIII* (H. K. Marshall, J. Spyromilio, and T. Usuda, eds.), (Online Only, United States), p. 277, SPIE, Dec. 2020.

[76] E. L. Lunde, M. Berthoud, N. S. DeNigris, S. M. Doyle, D. Ferrusca, J. E. Golec, S. W. Kuczarski, D. Lee, Z. Ma, P. D. Mauskopf, M. McCrackan, J. J. McMahon, G. A. Novak, G. Pisano, S. M. Simon, K. Souccar, C. E. Tucker, M. Underhill, E. Van Camp, and G. W. Wilson, "The TolTEC camera: optical alignment and characterization," in *Millimeter, Submillimeter, and Far-Infrared Detectors and Instrumentation for Astronomy XI* (J. Zmuidzinas and J.-R. Gao, eds.), (Montréal, Canada), p. 83, SPIE, Aug. 2022.

[77] D. Lee, G. A. Novak, M. Berthoud, J. Bussan, R. Golenia, E. Van Camp, G. W. Wilson, N. S. DeNigris, Z. Ma, M. McCrackan, K. Souccar, L. M. Fissel, A. Bij, F. Thiel, I. Aretxaga, D. Ferrusca, P. D. Mauskopf, E. L. Lunde, P. A. R. Ade, C. E. Tucker, G. Pisano, E. G. Cox, L. Sabin, C. Carrasco-Gonzalez, A. Pasetto, A. Gómez-Ruiz, C. Hull, J. E. Austermann, J. A. Beall, J. Gao, and M. R. Vissers, "The TolTEC camera: polarimetric commissioning and performance of the continuously rotating half-wave plate," in *Millimeter, Submillimeter, and Far-Infrared Detectors and Instrumentation for Astronomy XI* (J. Zmuidzinas and J.-R. Gao, eds.), (Montréal, Canada), p. 113, SPIE, Aug. 2022.

[78] P. D. Mauskopf, "Transition Edge Sensors and Kinetic Inductance Detectors in Astronomical Instruments," *PASP*, vol. 130, p. 082001, June 2018. Publisher: The Astronomical Society of the Pacific.

[79] J. E. Austermann, J. A. Beall, S. A. Bryan, B. Dober, J. Gao, G. Hilton, J. Hubmayr, P. Mauskopf, C. M. McKenney, S. M. Simon, J. N. Ullom, M. R. Vissers, and

G. W. Wilson, "Millimeter-Wave Polarimeters Using Kinetic Inductance Detectors for TolTEC and Beyond," *J Low Temp Phys*, vol. 193, pp. 120–127, Nov. 2018.

[80] J. W. Lamb, "Miscellaneous data on materials for millimetre and submillimetre optics," *Int J Infrared Milli Waves*, vol. 17, pp. 1997–2034, Dec. 1996.

[81] H. K. Raut, V. A. Ganesh, A. S. Nair, and S. Ramakrishna, "Anti-reflective coatings: A critical, in-depth review," *Energy Environ. Sci.*, vol. 4, no. 10, p. 3779, 2011.

[82] K. P. Coughlin, J. J. McMahon, K. T. Crowley, B. J. Koopman, K. H. Miller, S. M. Simon, and E. J. Wollack, "Pushing the Limits of Broadband and High-Frequency Metamaterial Silicon Antireflection Coatings," *J Low Temp Phys*, vol. 193, pp. 876–885, Dec. 2018.

[83] A. M. Ali, S. Adachi, K. Arnold, P. Ashton, A. Bazarko, Y. Chinone, G. Coppi, L. Corbett, K. D. Crowley, K. T. Crowley, M. Devlin, S. Dicker, S. Duff, C. Ellis, N. Galitzki, N. Goeckner-Wald, K. Harrington, E. Healy, C. A. Hill, S.-P. P. Ho, J. Hubmayr, B. Keating, K. Kiuchi, A. Kusaka, A. T. Lee, M. Ludlam, A. Mangu, F. Matsuda, H. McCarrick, F. Nati, M. D. Niemack, H. Nishino, J. Orlowski-Scherer, M. Sathyanarayana Rao, C. Raum, Y. Sakurai, M. Salatino, T. Sasse, J. Seibert, C. Sierra, M. Silva-Feaver, J. Spisak, S. M. Simon, S. Staggs, O. Tajima, G. Teply, T. Tsan, E. Wollack, B. Westbrook, Z. Xu, M. Zannoni, and N. Zhu, "Small Aperture Telescopes for the Simons Observatory," *J Low Temp Phys*, vol. 200, pp. 461–471, Sept. 2020.

[84] G. E. Chesmore, T. Mroczkowski, J. McMahon, S. Sutariya, A. Josaitis, and L. Jensen, "Reflectometry Measurements of the Loss Tangent in Silicon at Millimeter Wavelengths," 2018. Publisher: [object Object] Version Number: 1.

[85] N. M. Alford and S. J. Penn, "Sintered alumina with low dielectric loss," *Journal of Applied Physics*, vol. 80, pp. 5895–5898, Nov. 1996.

[86] J. D. Breeze, X. Aupi, and N. M. Alford, "Ultralow loss polycrystalline alumina," *Applied Physics Letters*, vol. 81, pp. 5021–5023, Dec. 2002.

[87] M. N. Afsar, "Precision millimeter-wave dielectric measurements of birefringent crystalline sapphire and ceramic alumina," *IEEE Trans. Instrum. Meas.*, vol. IM-36, pp. 554–559, June 1987.

[88] Y. Inoue, T. Matsumura, M. Hazumi, A. T. Lee, T. Okamura, A. Suzuki, T. Tomaru, and H. Yamaguchi, "Cryogenic infrared filter made of alumina for use at millimeter wavelength," *Appl. Opt., AO*, vol. 53, pp. 1727–1733, Mar. 2014. Publisher: Optica Publishing Group.

[89] Y. Inoue, N. Stebor, P. A. R. Ade, Y. Akiba, K. Arnold, A. E. Anthony, M. Atlas, D. Barron, A. Bender, D. Boettger, J. Borrilll, S. Chapman, Y. Chinone, A. Cukierman, M. Dobbs, T. Elleflot, J. Errard, G. Fabbian, C. Feng, A. Gilbert, N. W. Halverson,

M. Hasegawa, K. Hattori, M. Hazumi, W. L. Holzapfel, Y. Hori, G. C. Jaehnig, A. H. Jaffe, N. Katayama, B. Keating, Z. Kermish, R. Keskitalo, T. Kisner, M. Le Jeune, A. T. Lee, E. M. Leitch, E. Linder, F. Matsuda, T. Matsumura, X. Meng, H. Morii, M. J. Myers, M. Navaroli, H. Nishino, T. Okamura, H. Paar, J. Peloton, D. Poletti, G. Rebeiz, C. L. Reichardt, P. L. Richards, C. Ross, D. E. Schenck, B. D. Sherwin, P. Siritanasak, G. Smecher, M. Sholl, B. Steinbach, R. Stompor, A. Suzuki, J. Suzuki, S. Takada, S. Takakura, T. Tomaru, B. Wilson, A. Yadav, H. Yamaguchi, and O. Zahn, "Thermal and optical characterization for POLARBEAR-2 optical system," (Montréal, Quebec, Canada), p. 91533A, Aug. 2014.

[90] A. Nadolski and others, "Broadband, millimeter-wave antireflection coatings for large-format, cryogenic aluminum oxide optics," *Appl. Opt.*, vol. 59, no. 10, pp. 3285–3295, 2020. _eprint: 1912.04272.

[91] M. Dierickx, P. A. R. Ade, Z. Ahmed, M. Amiri, D. Barkats, R. Basu Thakur, C. A. Bischoff, D. Beck, J. J. Bock, V. Buza, J. Cheshire, J. Connors, J. Cornelison, M. Crumrine, A. Cukierman, E. Denison, L. Duband, M. Eiben, S. Fatigoni, J. P. Filippini, N. Goeckner-Wald, D. C. Goldfinger, J. A. Grayson, P. Grimes, G. Hall, G. Halal, M. Halpern, E. Hand, S. Harrison, S. Henderson, S. R. Hildebrandt, G. C. Hilton, J. Hubmayr, H. Hui, K. D. Irwin, J. Kang, K. S. Karkare, S. Kefeli, J. M. Kovac, C. L. Kuo, K. Lau, E. M. Leitch, A. Lennox, K. G. Megerian, L. Minutolo, L. Moncelsi, Y. Nakato, T. Namikawa, H. T. Nguyen, R. O'Brient, S. Palladino, M. Petroff, N. Precup, T. Prouve, C. Pryke, B. Racine, C. D. Reintsema, D. Santalucia, A. Schillaci, B. L. Schmitt, B. Singari, A. Soliman, T. S. Germaine, B. Steinbach, R. V. Sudiwala, K. L. Thompson, C. Tucker, A. D. Turner, C. Umiltà, C. Verges, A. G. Vieregg, A. Wandui, A. C. Weber, D. V. Wiebe, J. Willmert, W. L. K. Wu, E. Yang, K. W. Yoon, E. Young, C. Yu, L. Zeng, C. Zhang, and S. Zhang, "Plastic Laminate Antireflective Coatings for Millimeter-Wave Optics in BICEP Array," *J Low Temp Phys*, vol. 211, pp. 366–374, June 2023.

[92] T. Nitta, S. Sekiguchi, Y. Sekimoto, K. Mitsui, N. Okada, K. Karatsu, M. Naruse, M. Sekine, H. Matsuo, T. Noguchi, M. Seta, and N. Nakai, "Anti-reflection Coating for Cryogenic Silicon and Alumina Lenses in Millimeter-Wave Bands," *J Low Temp Phys*, vol. 176, pp. 677–683, Sept. 2014.

[93] D. Rosen, A. Suzuki, B. Keating, W. Krantz, A. T. Lee, E. Quealy, P. L. Richards, P. Siritanasak, and W. Walker, "Epoxy-based broadband antireflection coating for millimeter-wave optics," *Appl. Opt.*, vol. 52, p. 8102, Nov. 2013.

[94] Y. Inoue, T. Hamada, M. Hasegawa, M. Hazumi, Y. Hori, A. Suzuki, T. Tomaru, T. Matsumura, T. Sakata, T. Minamoto, and T. Hirai, "Two-layer anti-reflection coating with mullite and polyimide foam for large-diameter cryogenic infrared filters," *Appl. Opt., AO*, vol. 55, pp. D22–D28, Dec. 2016. Publisher: Optica Publishing Group.

[95] R. Takaku, Q. Wen, S. Cray, M. Devlin, S. Dicker, S. Hanany, T. Hasebe, T. Iida, N. Katayama, K. Konishi, M. Kuwata-Gonokami, T. Matsumura, N. Mio, H. Sakurai,

Y. Sakurai, R. Yamada, and J. Yumoto, "Large diameter millimeter-wave low-pass filter made of alumina with laser ablated anti-reflection coating," *Opt. Express, OE*, vol. 29, pp. 41745–41765, Dec. 2021. Publisher: Optica Publishing Group.

[96] T. Matsumura, K. Young, Q. Wen, S. Hanany, H. Ishino, Y. Inoue, M. Hazumi, J. Koch, O. Suttman, and V. Schütz, "Millimeter-wave broadband antireflection coatings using laser ablation of subwavelength structures," *Appl. Opt.*, vol. 55, p. 3502, May 2016.

[97] K. Harrington, T. Marriage, A. Ali, J. W. Appel, C. L. Bennett, F. Boone, M. Brewer, M. Chan, D. T. Chuss, F. Colazo, S. Dahal, K. Denis, R. Dünner, J. Eimer, T. Essinger-Hileman, P. Fluxa, M. Halpern, G. Hilton, G. F. Hinshaw, J. Hubmayr, J. Iuliano, J. Karakla, J. McMahon, N. T. Miller, S. H. Moseley, G. Palma, L. Parker, M. Petroff, B. Pradenas, K. Rostem, M. Sagliocca, D. Valle, D. Watts, E. Wollack, Z. Xu, and L. Zeng, "The Cosmology Large Angular Scale Surveyor," (Edinburgh, United Kingdom), p. 99141K, July 2016.

[98] G. Rhoades, K. Helson, J. Iuliano, A. Ali, J. W. Appel, C. Bennett, M. Brewer, R. Bustos, D. T. Chuss, J. Cleary, J. Denes Couto, S. Dahal, K. L. Denis, R. Dünner, J. R. Eimer, T. M. Essinger-Hileman, P. Fluxa, M. Halpern, K. Harrington, G. C. Hilton, G. F. Hinshaw, J. Hubmayr, J. Karakla, T. Marriage, N. Miller, J. J. McMahon, C. Nuñez, I. Padilla, G. Palma, L. Parker, M. Petroff, B. Pradenas Márquez, R. Reeves, C. D. Reintsema, K. Rostem, D. Augusto Nunes Valle, T. Van Engelhoven, B. Wang, Q. Wang, D. J. Watts, J. Weiland, E. J. Wollack, Z. L. Xu, Z. Yan, and L. Zeng, "The Cosmology Large Angular Scale Surveyor receiver design," in *Millimeter, Submillimeter, and Far-Infrared Detectors and Instrumentation for Astronomy IX* (J. Zmuidzinas and J.-R. Gao, eds.), (Austin, United States), p. 78, SPIE, July 2018.

[99] P. Lalanne and D. Lemercier-lalanne, "On the effective medium theory of subwavelength periodic structures," *Journal of Modern Optics*, vol. 43, pp. 2063–2085, Oct. 1996.

[100] E. B. Grann, M. G. Moharam, and D. A. Pommet, "Artificial uniaxial and biaxial dielectrics with use of two-dimensional subwavelength binary gratings," *J. Opt. Soc. Am. A*, vol. 11, p. 2695, Oct. 1994.

[101] H. Kikuta, Y. Ohira, H. Kubo, and K. Iwata, "Effective medium theory of two-dimensional subwavelength gratings in the non-quasi-static limit," *J. Opt. Soc. Am. A*, vol. 15, p. 1577, June 1998.

[102] D. H. Raguin and G. M. Morris, "Analysis of antireflection-structured surfaces with continuous one-dimensional surface profiles," *Appl. Opt.*, vol. 32, p. 2582, May 1993.

[103] G. E. Chesmore, K. Harrington, C. E. Sierra, P. A. Gallardo, S. Sutariya, T. Alford, A. E. Adler, T. Bhandarkar, G. Coppi, N. Dachlythra, J. Golec, J. Gudmundsson, S. K. Haridas, B. R. Johnson, A. M. Kofman, J. Iuliano, J. McMahon, M. D. Niemack, J. Orlowski-Scherer, K. P. Sarmiento, R. Puddu, M. Silva-Feaver, S. M. Simon, J. Robe,

E. J. Wollack, and Z. Xu, "Simons Observatory: characterizing the Large Aperture Telescope Receiver with radio holography," *Appl. Opt., AO*, vol. 61, pp. 10309–10319, Dec. 2022. Publisher: Optica Publishing Group.

[104] C. E. Sierra, K. Harrington, S. Sutariya, T. Alford, A. M. Kofman, G. E. Chesmore, J. E. Austermann, A. Bazarko, J. A. Beall, T. Bhandarkar, M. J. Devlin, S. R. Dicker, P. N. Dow, S. M. Duff, D. Dutcher, N. Galitzki, J. E. Golec, J. C. Groh, J. E. Gudmundsson, S. K. Haridas, E. Healy, J. Hubmayr, J. Iuliano, B. R. Johnson, C. S. Lessler, R. A. Lew, M. J. Link, T. J. Lucas, J. J. McMahon, J. E. Moore, F. Nati, M. D. Niemack, B. L. Schmitt, M. Silva-Feaver, R. Singh, R. F. Sonka, A. Thomas, R. J. Thornton, T. Tsan, J. N. Ullom, J. L. Van Lanen, E. M. Vavagiakis, M. R. Vissers, Y. Wang, and K. Zheng, "Simons Observatory: Pre-deployment Performance of a Large Aperture Telescope Optics Tube in the 90 and 150 GHz Spectral Bands," May 2024. arXiv:2405.06868 [astro-ph].

[105] W. P. Blair, K. Davidson, R. A. Fesen, A. Uomoto, G. M. MacAlpine, and R. B. C. Henry, "Hubble Space Telescope Wide Field Planetary Camera 2 Imaging of the Crab Nebula. I. Observational Overview*," *ApJS*, vol. 109, p. 473, Apr. 1997.

[106] G. Dubner, G. Castelletti, O. Kargaltsev, G. G. Pavlov, M. Bietenholz, and A. Talavera, "Morphological Properties of the Crab Nebula: A Detailed Multiwavelength Study Based on New VLA, HST, Chandra, and XMM-Newton Images," *ApJ*, vol. 840, p. 82, May 2017. Publisher: The American Astronomical Society.

[107] K. Mori, J. J. Hester, D. N. Burrows, G. G. Pavlov, and H. Tsunemi, "Chandra reveals the Dynamic Structure of the Inner Crab Nebula," 2001. Publisher: [object Object] Version Number: 1.

[108] J. Aumont, J. F. Macías-Pérez, A. Ritacco, N. Ponthieu, and A. Mangilli, "Absolute calibration of the polarisation angle for future CMB B-mode experiments from current and future measurements of the Crab nebula," *A&A*, vol. 634, p. A100, Feb. 2020. Publisher: EDP Sciences.

[109] M. Bonato, E. Liuzzo, D. Herranz, J. Gonzalez-Nuevo, L. Bonavera, M. Tucci, M. Massardi, G. de Zotti, M. Negrello, and M. A. Zwaan, "VizieR Online Data Catalog: The ALMA Calibrator Catalogue (Bonato+, 2019)," *VizieR Online Data Catalog*, vol. 748, p. J/MNRAS/485/1188, Sept. 2019. ADS Bibcode: 2019yCat..74851188B.

[110] M. Mallaby-Kay, Z. Atkins, S. Aiola, S. Amodeo, J. E. Austermann, J. A. Beall, D. T. Becker, J. R. Bond, E. Calabrese, G. E. Chesmore, S. K. Choi, K. T. Crowley, O. Darwish, E. V. Denison, M. J. Devlin, S. M. Duff, A. J. Duivenvoorden, J. Dunkley, S. Ferraro, K. Fichman, P. A. Gallardo, J. E. Golec, Y. Guan, D. Han, M. Hasselfield, J. C. Hill, G. C. Hilton, M. Hilton, R. Hložek, J. Hubmayr, K. M. Huffenberger, J. P. Hughes, B. J. Koopman, T. Louis, A. MacInnis, M. S. Madhavacheril, J. McMahon, K. Moodley, S. Naess, T. Namikawa, F. Nati, L. B. Newburgh, J. P. Nibarger, M. D. Niemack, L. A. Page, M. Salatino, E. Schaan, A. Schillaci, N. Sehgal, B. D. Sherwin,

C. Sifón, S. Simon, S. T. Staggs, E. R. Storer, J. N. Ullom, A. V. Engelen, J. V. Lanen, L. R. Vale, E. J. Wollack, and Z. Xu, "The Atacama Cosmology Telescope: Summary of DR4 and DR5 Data Products and Data Access," *ApJS*, vol. 255, p. 11, July 2021. Publisher: The American Astronomical Society.

[111] J. L. Weiland, N. Odegard, R. S. Hill, E. Wollack, G. Hinshaw, M. R. Greason, N. Jarosik, L. Page, C. L. Bennett, J. Dunkley, B. Gold, M. Halpern, A. Kogut, E. Komatsu, D. Larson, M. Limon, S. S. Meyer, M. R. Nolta, K. M. Smith, D. N. Spergel, G. S. Tucker, and E. L. Wright, "SEVEN-YEAR *WILKINSON MICROWAVE ANISOTROPY PROBE* (*WMAP*) OBSERVATIONS: PLANETS AND CELESTIAL CALIBRATION SOURCES," *ApJS*, vol. 192, p. 19, Feb. 2011.

[112] Planck Collaboration, P. A. R. Ade, N. Aghanim, F. Argüeso, M. Arnaud, M. Ashdown, J. Aumont, C. Baccigalupi, A. J. Banday, R. B. Barreiro, N. Bartolo, E. Battaner, C. Beichman, K. Benabed, A. Benoît, A. Benoit-Lévy, J.-P. Bernard, M. Bersanelli, P. Bielewicz, J. J. Bock, H. Böhringer, A. Bonaldi, L. Bonavera, J. R. Bond, J. Borrill, F. R. Bouchet, F. Boulanger, M. Bucher, C. Burigana, R. C. Butler, E. Calabrese, J.-F. Cardoso, P. Carvalho, A. Catalano, A. Challinor, A. Chamballu, R.-R. Chary, H. C. Chiang, P. R. Christensen, M. Clemens, D. L. Clements, S. Colombi, L. P. L. Colombo, C. Combet, F. Couchot, A. Coulais, B. P. Crill, A. Curto, F. Cuttaia, L. Danese, R. D. Davies, R. J. Davis, P. De Bernardis, A. De Rosa, G. De Zotti, J. Delabrouille, F.-X. Désert, C. Dickinson, J. M. Diego, H. Dole, S. Donzelli, O. Doré, M. Douspis, A. Ducout, X. Dupac, G. Efstathiou, F. Elsner, T. A. Enßlin, H. K. Eriksen, E. Falgarone, J. Fergusson, F. Finelli, O. Forni, M. Frailis, A. A. Fraisse, E. Franceschi, A. Frejsel, S. Galeotta, S. Galli, K. Ganga, M. Giard, Y. Giraud-Héraud, E. Gjerløw, J. González-Nuevo, K. M. Górski, S. Gratton, A. Gregorio, A. Gruppuso, J. E. Gudmundsson, F. K. Hansen, D. Hanson, D. L. Harrison, G. Helou, S. Henrot-Versillé, C. Hernández-Monteagudo, D. Herranz, S. R. Hildebrandt, E. Hivon, M. Hobson, W. A. Holmes, A. Hornstrup, W. Hovest, K. M. Huffenberger, G. Hurier, A. H. Jaffe, T. R. Jaffe, W. C. Jones, M. Juvela, E. Keihänen, R. Keskitalo, T. S. Kisner, R. Kneissl, J. Knoche, M. Kunz, H. Kurki-Suonio, G. Lagache, A. Lähteenmäki, J.-M. Lamarre, A. Lasenby, M. Lattanzi, C. R. Lawrence, J. P. Leahy, R. Leonardi, J. León-Tavares, J. Lesgourgues, F. Levrier, M. Liguori, P. B. Lilje, M. Linden-Vørnle, M. López-Caniego, P. M. Lubin, J. F. Macías-Pérez, G. Maggio, D. Maino, N. Mandolesi, A. Mangilli, M. Maris, D. J. Marshall, P. G. Martin, E. Martínez-González, S. Masi, S. Matarrese, P. McGehee, P. R. Meinhold, A. Melchiorri, L. Mendes, A. Mennella, M. Migliaccio, S. Mitra, M.-A. Miville-Deschênes, A. Moneti, L. Montier, G. Morgante, D. Mortlock, A. Moss, D. Munshi, J. A. Murphy, P. Naselsky, F. Nati, P. Natoli, M. Negrello, C. B. Netterfield, H. U. Nørgaard-Nielsen, F. Noviello, D. Novikov, I. Novikov, C. A. Oxborrow, F. Paci, L. Pagano, F. Pajot, R. Paladini, D. Paoletti, B. Partridge, F. Pasian, G. Patanchon, T. J. Pearson, O. Perdereau, L. Perotto, F. Perrotta, V. Pettorino, F. Piacentini, M. Piat, E. Pierpaoli, D. Pietrobon, S. Plaszczynski, E. Pointecouteau, G. Polenta, G. W. Pratt, G. Prézeau, S. Prunet, J.-L. Puget, J. P. Rachen, W. T. Reach, R. Rebolo, M. Reinecke, M. Remazeilles, C. Renault,

A. Renzi, I. Ristorcelli, G. Rocha, C. Rosset, M. Rossetti, G. Roudier, M. Rowan-Robinson, J. A. Rubiño-Martín, B. Rusholme, M. Sandri, H. S. Sanghera, D. Santos, M. Savelainen, G. Savini, D. Scott, M. D. Seiffert, E. P. S. Shellard, L. D. Spencer, V. Stolyarov, R. Sudiwala, R. Sunyaev, D. Sutton, A.-S. Suur-Uski, J.-F. Sygnet, J. A. Tauber, L. Terenzi, L. Toffolatti, M. Tomasi, M. Tornikoski, M. Tristram, M. Tucci, J. Tuovinen, M. Türler, G. Umana, L. Valenziano, J. Valiviita, B. Van Tent, P. Vielva, F. Villa, L. A. Wade, B. Walter, B. D. Wandelt, I. K. Wehus, D. Yvon, A. Zacchei, and A. Zonca, "*Planck* 2015 results: XXVI. The Second *Planck* Catalogue of Compact Sources," *A&A*, vol. 594, p. A26, Oct. 2016.

[113] A. Ritacco, J. F. Macías-Pérez, N. Ponthieu, R. Adam, P. Ade, P. André, J. Aumont, A. Beelen, A. Benoît, A. Bideaud, N. Billot, O. Bourrion, A. Bracco, M. Calvo, A. Catalano, G. Coiffard, B. Comis, A. D'Addabbo, M. D. Petris, F.-X. Désert, S. Doyle, J. Goupy, C. Kramer, G. Lagache, S. Leclercq, J.-F. Lestrade, P. Mauskopf, F. Mayet, A. Maury, A. Monfardini, F. Pajot, E. Pascale, L. Perotto, G. Pisano, M. Rebolo-Iglesias, V. Revéret, L. Rodriguez, C. Romero, H. Roussel, F. Ruppin, K. Schuster, A. Sievers, G. Siringo, C. Thum, S. Triqueneaux, C. Tucker, H. Wiesemeyer, and R. Zylka, "NIKA 150 GHz polarization observations of the Crab nebula and its spectral energy distribution," *A&A*, vol. 616, p. A35, Aug. 2018. Publisher: EDP Sciences.

[114] Ivezić, S. M. Kahn, J. A. Tyson, B. Abel, E. Acosta, R. Allsman, D. Alonso, Y. AlSayyad, S. F. Anderson, J. Andrew, J. R. P. Angel, G. Z. Angeli, R. Ansari, P. Antilogus, C. Araujo, R. Armstrong, K. T. Arndt, P. Astier, Aubourg, N. Auza, T. S. Axelrod, D. J. Bard, J. D. Barr, A. Barrau, J. G. Bartlett, A. E. Bauer, B. J. Bauman, S. Baumont, E. Bechtol, K. Bechtol, A. C. Becker, J. Becla, C. Beldica, S. Bellavia, F. B. Bianco, R. Biswas, G. Blanc, J. Blazek, R. D. Blandford, J. S. Bloom, J. Bogart, T. W. Bond, M. T. Booth, A. W. Borgland, K. Borne, J. F. Bosch, D. Boutigny, C. A. Brackett, A. Bradshaw, W. N. Brandt, M. E. Brown, J. S. Bullock, P. Burchat, D. L. Burke, G. Cagnoli, D. Calabrese, S. Callahan, A. L. Callen, J. L. Carlin, E. L. Carlson, S. Chandrasekharan, G. Charles-Emerson, S. Chesley, E. C. Cheu, H.-F. Chiang, J. Chiang, C. Chirino, D. Chow, D. R. Ciardi, C. F. Claver, J. Cohen-Tanugi, J. J. Cockrum, R. Coles, A. J. Connolly, K. H. Cook, A. Cooray, K. R. Covey, C. Cribbs, W. Cui, R. Cutri, P. N. Daly, S. F. Daniel, F. Daruich, G. Daubard, G. Daues, W. Dawson, F. Delgado, A. Dellapenna, R. d. Peyster, M. d. Val-Borro, S. W. Digel, P. Doherty, R. Dubois, G. P. Dubois-Felsmann, J. Durech, F. Economou, T. Eifler, M. Eracleous, B. L. Emmons, A. F. Neto, H. Ferguson, E. Figueroa, M. Fisher-Levine, W. Focke, M. D. Foss, J. Frank, M. D. Freemon, E. Gangler, E. Gawiser, J. C. Geary, P. Gee, M. Geha, C. J. B. Gessner, R. R. Gibson, D. K. Gilmore, T. Glanzman, W. Glick, T. Goldina, D. A. Goldstein, I. Goodenow, M. L. Graham, W. J. Gressler, P. Gris, L. P. Guy, A. Guyonnet, G. Haller, R. Harris, P. A. Hascall, J. Haupt, F. Hernandez, S. Herrmann, E. Hileman, J. Hoblitt, J. A. Hodgson, C. Hogan, J. D. Howard, D. Huang, M. E. Huffer, P. Ingraham, W. R. Innes, S. H. Jacoby, B. Jain, F. Jammes, M. J. Jee, T. Jenness, G. Jernigan, D. Jevremović, K. Johns, A. S. Johnson, M. W. G. Johnson, R. L. Jones, C. Juramy-Gilles, M. Jurić, J. S. Kalirai, N. J. Kallivayalil, B. Kalmbach,

J. P. Kantor, P. Karst, M. M. Kasliwal, H. Kelly, R. Kessler, V. Kinnison, D. Kirkby, L. Knox, I. V. Kotov, V. L. Krabbendam, K. S. Krughoff, P. Kubánek, J. Kuczewski, S. Kulkarni, J. Ku, N. R. Kurita, C. S. Lage, R. Lambert, T. Lange, J. B. Langton, L. L. Guillou, D. Levine, M. Liang, K.-T. Lim, C. J. Lintott, K. E. Long, M. Lopez, P. J. Lotz, R. H. Lupton, N. B. Lust, L. A. MacArthur, A. Mahabal, R. Mandelbaum, T. W. Markiewicz, D. S. Marsh, P. J. Marshall, S. Marshall, M. May, R. McKercher, M. McQueen, J. Meyers, M. Migliore, M. Miller, D. J. Mills, C. Miraval, J. Moeyens, F. E. Moolekamp, D. G. Monet, M. Moniez, S. Monkewitz, C. Montgomery, C. B. Morrison, F. Mueller, G. P. Muller, F. M. Arancibia, D. R. Neill, S. P. Newbry, J.-Y. Nief, A. Nomerotski, M. Nordby, P. O'Connor, J. Oliver, S. S. Olivier, K. Olsen, W. O'Mullane, S. Ortiz, S. Osier, R. E. Owen, R. Pain, P. E. Palecek, J. K. Parejko, J. B. Parsons, N. M. Pease, J. M. Peterson, J. R. Peterson, D. L. Petravick, M. E. L. Petrick, C. E. Petry, F. Pierfederici, S. Pietrowicz, R. Pike, P. A. Pinto, R. Plante, S. Plate, J. P. Plutchak, P. A. Price, M. Prouza, V. Radeka, J. Rajagopal, A. P. Rasmussen, N. Regnault, K. A. Reil, D. J. Reiss, M. A. Reuter, S. T. Ridgway, V. J. Riot, S. Ritz, S. Robinson, W. Roby, A. Roodman, W. Rosing, C. Roucelle, M. R. Rumore, S. Russo, A. Saha, B. Sassolas, T. L. Schalk, P. Schellart, R. H. Schindler, S. Schmidt, D. P. Schneider, M. D. Schneider, W. Schoening, G. Schumacher, M. E. Schwamb, J. Sebag, B. Selvy, G. H. Sembroski, L. G. Seppala, A. Serio, E. Serrano, R. A. Shaw, I. Shipsey, J. Sick, N. Silvestri, C. T. Slater, J. A. Smith, R. C. Smith, S. Sobhani, C. Soldahl, L. Storrie-Lombardi, E. Stover, M. A. Strauss, R. A. Street, C. W. Stubbs, I. S. Sullivan, D. Sweeney, J. D. Swinbank, A. Szalay, P. Takacs, S. A. Tether, J. J. Thaler, J. G. Thayer, S. Thomas, A. J. Thornton, V. Thukral, J. Tice, D. E. Trilling, M. Turri, R. V. Berg, D. V. Berk, K. Vetter, F. Virieux, T. Vucina, W. Wahl, L. Walkowicz, B. Walsh, C. W. Walter, D. L. Wang, S.-Y. Wang, M. Warner, O. Wiecha, B. Willman, S. E. Winters, D. Wittman, S. C. Wolff, W. M. Wood-Vasey, X. Wu, B. Xin, P. Yoachim, and H. Zhan, "LSST: From Science Drivers to Reference Design and Anticipated Data Products," *ApJ*, vol. 873, p. 111, Mar. 2019. Publisher: The American Astronomical Society.

[115] D. Collaboration, A. G. Adame, J. Aguilar, S. Ahlen, S. Alam, D. M. Alexander, M. Alvarez, O. Alves, A. Anand, U. Andrade, E. Armengaud, S. Avila, A. Aviles, H. Awan, B. Bahr-Kalus, S. Bailey, C. Baltay, A. Bault, J. Behera, S. BenZvi, A. Bera, F. Beutler, D. Bianchi, C. Blake, R. Blum, S. Brieden, A. Brodzeller, D. Brooks, E. Buckley-Geer, E. Burtin, R. Calderon, R. Canning, A. C. Rosell, R. Cereskaite, J. L. Cervantes-Cota, S. Chabanier, E. Chaussidon, J. Chaves-Montero, S. Chen, X. Chen, T. Claybaugh, S. Cole, A. Cuceu, T. M. Davis, K. Dawson, A. de la Macorra, A. de Mattia, N. Deiosso, A. Dey, B. Dey, Z. Ding, P. Doel, J. Edelstein, S. Eftekharzadeh, D. J. Eisenstein, A. Elliott, P. Fagrelius, K. Fanning, S. Ferraro, J. Ereza, N. Findlay, B. Flaugher, A. Font-Ribera, D. Forero-Sánchez, J. E. Forero-Romero, C. S. Frenk, C. Garcia-Quintero, E. Gaztañaga, H. Gil-Marín, S. G. A. Gontcho, A. X. Gonzalez-Morales, V. Gonzalez-Perez, C. Gordon, D. Green, D. Gruen, R. Gsponer, G. Gutierrez, J. Guy, B. Hadzhiyska, C. Hahn, M. M. S. Hanif, H. K. Herrera-Alcantar, K. Honscheid, C. Howlett, D. Huterer, V. Iršič, M. Ishak, S. Juneau,

N. G. Karaçaylı, R. Kehoe, S. Kent, D. Kirkby, A. Kremin, A. Krolewski, Y. Lai, T.-W. Lan, M. Landriau, D. Lang, J. Lasker, J. M. L. Goff, L. L. Guillou, A. Leauthaud, M. E. Levi, T. S. Li, E. Linder, K. Lodha, C. Magneville, M. Manera, D. Margala, P. Martini, M. Maus, P. McDonald, L. Medina-Varela, A. Meisner, J. Mena-Fernández, R. Miquel, J. Moon, S. Moore, J. Moustakas, N. Mudur, E. Mueller, A. Muñoz-Gutiérrez, A. D. Myers, S. Nadathur, L. Napolitano, R. Neveux, J. A. Newman, N. M. Nguyen, J. Nie, G. Niz, H. E. Noriega, N. Padmanabhan, E. Paillas, N. Palanque-Delabrouille, J. Pan, S. Penmetsa, W. J. Percival, M. M. Pieri, M. Pinon, C. Poppett, A. Porredon, F. Prada, A. Pérez-Fernández, I. Pérez-Ràfols, D. Rabinowitz, A. Raichoor, C. Ramírez-Pérez, S. Ramirez-Solano, C. Ravoux, M. Rashkovetskyi, M. Rezaie, J. Rich, A. Rocher, C. Rockosi, N. A. Roe, A. Rosado-Marin, A. J. Ross, G. Rossi, R. Ruggeri, V. Ruhlmann-Kleider, L. Samushia, E. Sanchez, C. Saulder, E. F. Schlafly, D. Schlegel, M. Schubnell, H. Seo, A. Shafieloo, R. Sharples, J. Silber, A. Slosar, A. Smith, D. Sprayberry, T. Tan, G. Tarlé, P. Taylor, S. Trusov, L. A. Ureña-López, R. Vaisakh, D. Valcin, F. Valdes, M. Vargas-Magaña, L. Verde, M. Walther, B. Wang, M. S. Wang, B. A. Weaver, N. Weaverdyck, R. H. Wechsler, D. H. Weinberg, M. White, J. Yu, Y. Yu, S. Yuan, C. Yèche, E. A. Zaborowski, P. Zarrouk, H. Zhang, C. Zhao, R. Zhao, R. Zhou, T. Zhuang, and H. Zou, "DESI 2024 VI: Cosmological Constraints from the Measurements of Baryon Acoustic Oscillations," Apr. 2024. arXiv:2404.03002 [astro-ph].

[116] M. Postman, D. Coe, N. Benítez, L. Bradley, T. Broadhurst, M. Donahue, H. Ford, O. Graur, G. Graves, S. Jouvel, A. Koekemoer, D. Lemze, E. Medezinski, A. Molino, L. Moustakas, S. Ogaz, A. Riess, S. Rodney, P. Rosati, K. Umetsu, W. Zheng, A. Zitrin, M. Bartelmann, R. Bouwens, N. Czakon, S. Golwala, O. Host, L. Infante, S. Jha, Y. Jimenez-Teja, D. Kelson, O. Lahav, R. Lazkoz, D. Maoz, C. McCully, P. Melchior, M. Meneghetti, J. Merten, J. Moustakas, M. Nonino, B. Patel, E. Regös, J. Sayers, S. Seitz, and A. V. d. Wel, "THE CLUSTER LENSING AND SUPERNOVA SURVEY WITH HUBBLE: AN OVERVIEW," *ApJS*, vol. 199, p. 25, Mar. 2012. Publisher: The American Astronomical Society.

[117] J. M. Lotz, A. Koekemoer, D. Coe, N. Grogin, P. Capak, J. Mack, J. Anderson, R. Avila, E. A. Barker, D. Borncamp, G. Brammer, M. Durbin, H. Gunning, B. Hilbert, H. Jenkner, H. Khandrika, Z. Levay, R. A. Lucas, J. MacKenty, S. Ogaz, B. Porterfield, N. Reid, M. Robberto, P. Royle, L. J. Smith, L. J. Storrie-Lombardi, B. Sunnquist, J. Surace, D. C. Taylor, R. Williams, J. Bullock, M. Dickinson, S. Finkelstein, P. Natarajan, J. Richard, B. Robertson, J. Tumlinson, A. Zitrin, K. Flanagan, K. Sembach, B. T. Soifer, and M. Mountain, "The Frontier Fields: Survey Design and Initial Results," *ApJ*, vol. 837, p. 97, Mar. 2017. Publisher: The American Astronomical Society.

[118] K. Nelson, E. T. Lau, D. Nagai, D. H. Rudd, and L. Yu, "WEIGHING GALAXY CLUSTERS WITH GAS. II. ON THE ORIGIN OF HYDROSTATIC MASS BIAS IN CDM GALAXY CLUSTERS," *ApJ*, vol. 782, p. 107, Feb. 2014. Publisher: The American Astronomical Society.

[119] A. V. Kravtsov, A. A. Klypin, and A. M. Khokhlov, "Adaptive Refinement Tree: A New High-Resolution N-Body Code for Cosmological Simulations," *ApJS*, vol. 111, p. 73, July 1997. Publisher: IOP Publishing.

[120] Z. Ma, M. McCrackan, N. DeNigris, K. Souccar, G. Wilson, J. E. Golec, P. Horton, D. Lee, P. Mauskopf, G. Novak, I. Rodríguez-Montoya, and J. Zaragoza-Cardiel, "The TolTEC Data Analysis Pipeline and Software Stack," *Bulletin of the AAS*, vol. 55, Feb. 2023.

[121] M. Remazeilles, J. Delabrouille, and J.-F. Cardoso, "Foreground component separation with generalized Internal Linear Combination," *Monthly Notices of the Royal Astronomical Society*, vol. 418, pp. 467–476, Nov. 2011.

[122] M. Tegmark, "Removing Real-World Foregrounds from Cosmic Microwave Background Maps," *ApJ*, vol. 502, p. 1, July 1998. Publisher: IOP Publishing.

[123] M. Tegmark, A. de Oliveira-Costa, and A. J. S. Hamilton, "High resolution foreground cleaned CMB map from WMAP," *Phys. Rev. D*, vol. 68, p. 123523, Dec. 2003. Publisher: American Physical Society.

[124] T. M. Crawford, R. Chown, G. P. Holder, K. A. Aird, B. A. Benson, L. E. Bleem, J. E. Carlstrom, C. L. Chang, H.-M. Cho, A. T. Crites, T. d. Haan, M. A. Dobbs, E. M. George, N. W. Halverson, N. L. Harrington, W. L. Holzapfel, Z. Hou, J. D. Hrubes, R. Keisler, L. Knox, A. T. Lee, E. M. Leitch, D. Luong-Van, D. P. Marrone, J. J. McMahon, S. S. Meyer, L. M. Mocanu, J. J. Mohr, T. Natoli, S. Padin, C. Pryke, C. L. Reichardt, J. E. Ruhl, J. T. Sayre, K. K. Schaffer, E. Shirokoff, Z. Staniszewski, A. A. Stark, K. T. Story, K. Vanderlinde, J. D. Vieira, and R. Williamson, "MAPS OF THE MAGELLANIC CLOUDS FROM COMBINED SOUTH POLE ESCOPE AND PLANCK DATA," *ApJS*, vol. 227, p. 23, Dec. 2016. Publisher: The American Astronomical Society.

[125] L. Perotto, R. Adam, P. Ade, H. Ajeddig, P. André, E. Artis, H. Aussel, R. Barrena, I. Bartalucci, A. Beelen, A. Benoît, S. Berta, L. Bing, O. Bourrion, M. Calvo, A. Catalano, M. D. Petris, F.-X. Désert, S. Doyle, E. F. C. Driessen, G. Ejlali, A. Ferragamo, A. Gomez, J. Goupy, C. Hanser, S. Katsioli, F. Kéruzoré, C. Kramer, B. Ladjelate, G. Lagache, S. Leclercq, J.-F. Lestrade, J. F. Macías-Pérez, S. C. Madden, A. Maury, P. Mauskopf, F. Mayet, A. Monfardini, A. Moyer-Anin, M. Muñoz-Echeverría, A. Paliwal, G. Pisano, E. Pointecouteau, N. Ponthieu, G. W. Pratt, V. Revéret, A. J. Rigby, A. Ritacco, C. Romero, H. Roussel, F. Ruppin, K. Schuster, A. Sievers, C. Tucker, and G. Yepes, "The NIKA2 Sunyaev-Zeldovich Large Program - Sample and upcoming product public release," *EPJ Web Conf.*, vol. 293, p. 00040, 2024. Publisher: EDP Sciences.